System Analysis and Design of a Low-Cost Micromechanical Seeker System

by

Brian J. Nagle

B.S. Mechanical Engineering
United States Air Force Academy, 2006

SUBMITTED TO THE DEPARTMENT OF MECHANICAL ENGINEERING IN
PARTIAL FULFILLMENT OF THE REQUIREMENTS FOR THE DEGREE OF

MASTER OF SCIENCE IN MECHANICAL ENGINEERING
AT THE
MASSACHUSETTS INSTITUTE OF TECHNOLOGY

JUNE 2008

Signature of Author:_____
Department of Mechanical Engineering
May 10, 2008

Certified by: _____
Dr. Domhnull Granquist-Fraser
Senior Technical Staff
The Charles Stark Draper Laboratory, Inc.
Thesis Supervisor

Certified by: _____
Professor Daniel E. Whitney
Engineering Systems Division
Senior Lecturer, Department of Mechanical Engineering
Thesis Advisor

Accepted by: _____
Professor Lallit Anand
Professor of Mechanical Engineering
Chairman, Committee for Graduate Students
Department of Mechanical Engineering

Report Documentation Page	Form Approved OMB No. 0704-0188

1. REPORT DATE **01 JUN 2008**	2. REPORT TYPE **N/A**	3. DATES COVERED **-**

4. TITLE AND SUBTITLE	5a. CONTRACT NUMBER
System Analysis and Design of a Low-Cost Micromechanical Seeker System	5b. GRANT NUMBER
	5c. PROGRAM ELEMENT NUMBER

6. AUTHOR(S)	5d. PROJECT NUMBER
	5e. TASK NUMBER
	5f. WORK UNIT NUMBER

7. PERFORMING ORGANIZATION NAME(S) AND ADDRESS(ES) **Massachusetts Institute Of Technology**	8. PERFORMING ORGANIZATION REPORT NUMBER **CI08-0019**

9. SPONSORING/MONITORING AGENCY NAME(S) AND ADDRESS(ES) **The Department of the Air Force AFIT/ENEL, Bldg 16 2275 D Street WPAFB, OH 45433**	10. SPONSOR/MONITOR'S ACRONYM(S)
	11. SPONSOR/MONITOR'S REPORT NUMBER(S)

12. DISTRIBUTION/AVAILABILITY STATEMENT

Approved for public release, distribution unlimited

13. SUPPLEMENTARY NOTES

The original document contains color images.

14. ABSTRACT

15. SUBJECT TERMS

16. SECURITY CLASSIFICATION OF:			17. LIMITATION OF ABSTRACT	18. NUMBER OF PAGES	19a. NAME OF RESPONSIBLE PERSON
a. REPORT **unclassified**	b. ABSTRACT **unclassified**	c. THIS PAGE **unclassified**	**UU**	**140**	

[This Page Intentionally Left Blank]

System Analysis and Design of a Low-Cost Micromechanical Seeker System

by

Brian James Nagle

Abstract

Precision guided targeting systems have been in use by the U.S. military for the last half-century. The desire for high targeting accuracies while maintaining minimal collateral damage has driven the implementation of guidance systems on a myriad of different platforms. Current seeker systems using global positioning system (GPS)-aided technology offer good accuracy, but are limited by an adversary's signal jamming capabilities and the dynamic nature of the military target environment. Furthermore, ultra-accurate inertial measurement units (IMU) that serve as stand-alone guidance systems are very expensive and offer no terminal guidance enhancement. As a result, it is cost prohibitive to equip some platforms with precision guidance capability.

The demand for high accuracy at low cost has prompted substantial recent development of micro-electromechanical systems (MEMS) IMU's and optical focal plane arrays (FPA). The resulting decreasing device size and production costs coupled with higher unit performance have created opportunities for implementing seeker-enabled systems on platforms previously deemed impractical. As a result, the author proposes a design methodology to develop a low-cost system while satisfying stringent performance requirements. The methodology is developed within the context of a strap-down seeker system for tactical applications.

The design tenets of the optical sensor, the inertial sensor, and projectile flight dynamics were analyzed in-depth for the specific scenario. The results of each analysis were combined to formulate a proposed system. The system was then modeled to produce system miss distance estimates for differing engagement situations. The system demonstrated 3σ miss distance estimates that were less than the maximum allowable error in each case.

The system cost was tabulated and a production price was approximated. Using current technology and pricing information for the main components, the analysis shows that a system with a 3σ miss distance of 0.801 m could be built for a unit price in the range of $11,730 - $19,550, depending on production costs. Design limitations are discussed, as well as strategies to improve the analysis for future consideration.

[This Page Intentionally Left Blank]

Acknowledgements

_____
Brian J. Nagle, 2nd Lt., USAF   May 10, 2008

[This Page Intentionally Left Blank]

Table of Contents

List of Figures

11

List of Tables

1 Introduction

1.1 Project Background

"Smart" munitions have become a staple in the vast majority of today's worldwide military arsenals. In general, the term "smart" refers to the ability to be guided autonomously to a target or delivery point. This autonomous guidance is usually achieved by some combination of an inertial measurement unit (IMU), a Global Positioning System (GPS) receiver, and a terminal guidance seeker to achieve high targeting accuracies with minimal collateral damage.

The United States military, in particular, has depended heavily on precision guided weapons to execute nearly every one of its operations since the conflict in Vietnam, and continues to rely greatly on precision guidance system for current operations. The increasingly high demand for these accurate munitions has driven substantial technology development in low cost precision guidance systems over the last half-century. Yet, despite the considerable advancements already realized, the development of better and cheaper smart munitions remains a high priority. As a result, all branches of the U.S. military continue to research new navigation and guidance technologies for their emerging and existing smart weapon systems.

Achieving precise targeting accuracy at low cost is a great challenge of the design process of smart weapons. Ultra-accurate munitions are typically quite expensive because of the excessive costs associated with their meticulous manufacturing, compact packaging, and detailed testing prior to use. Naturally, this accuracy vs. cost trade-off is at the forefront of the design process in nearly every laboratory developing the technology.

At first glance, simply adding an inexpensive GPS-enabled receiver to a moderately accurate IMU offers a solution to satisfy the two competing interests. State-of-the-art GPS technology offers position coordinate accuracies on the order of a few meters or less at a

reasonably low cost [1], and aiding with an IMU would only increase the system capability. However, an IMU aided solely with GPS presents shortcomings for military use. For example, in a hostile environment, GPS-aided guidance cannot be relied upon in close proximity to the target because of susceptibility to an adversary's GPS signal jamming capabilities. Without an extremely accurate IMU, the munition will likely not impact the target within an acceptable distance. In such situations, the ordnance must have the capacity to be guided autonomously to the target by some alternative means.

Moreover, for GPS aiding to be fully effective, an accurate *a priori* knowledge of the target location is required, which limits such precise targeting to objects that are immobile or are very slowly moving. Mobile or improvised targets demand real time updates from forward observers (troops, UAV's, etc.). Where the target is dynamic or its coordinate location is poorly defined, even the most accurate GPS + IMU combination is unable to contact the target and can lead to unnecessary collateral damage. Consequently, further autonomous on-board guidance capability is required to achieve the desired delivery accuracy against a target that is located in a hostile area, a mobile target, or a target whose position is poorly defined.

A sufficiently capable on-board terminal guidance seeker system provides a complete solution for this complexity. Seeker-enabled systems direct packages to the targets/delivery points during their terminal stages of flight, relieving the pressure on the IMU/GPS units to precisely guide the ordnances to their intended targets. Thus, due to the limitations of GPS aided IMU technology and the fleeting nature of many military targets, terminal guidance seekers are employed on a large number of military delivery systems.

1.1.1 Necessity of a New Design

The fabrication and packaging of seeker enhanced inertial guidance systems presents a highly sophisticated and complex process. Current literature on missile seekers reveals that in most powered and ballistic missile guidance systems, the seeker subsystem cost makes up an extremely large fraction of the total guidance system cost. As an example, the seeker system in the U.S. Air Force's AIM-9 Sidewinder missile demands approximately $70000 - $75000 of the total price of $84000, which includes the additional costs of the payload, rocket motor, and the control subsystem [2, 3]. Hence, for low value targets, the cost vs. benefit analysis of using

smart weapons dictates that either an unguided ordnance be employed, or the mission be abandoned. As a result, many military agencies have expressed the need for a low cost seeker system to create highly accurate and precise delivery packages.

Technological advancements in the areas of Micro-electromechanical Systems (MEMS) accelerometers and gyroscopes (components of an IMU) have paved the way for achieving higher IMU accuracies while driving down production costs.   Similarly, certain developments in areas of the consumer electronics market, such as those for charge-coupled devices (CCD's) used in digital cameras, have reduced the cost of producing the photodiode arrays used as focal planes in seeker heads for target imaging. Nevertheless, while the MEMS and photodiode technology advancements have created opportunities for implementing seeker-enabled systems on platforms that were previously deemed to be impractical, several remain to be explored in depth.

Of particular interest are applications involving munitions smaller than the AIM-9, or other similar large air-to-air missiles that are aimed at fast moving targets demanding expensive, ultra-accurate, high dynamic bandwidth seeker systems. For these small munitions, typically aimed at stationary or much slower targets, compact, robust, low-cost seeker systems are highly desirable. Several tactical examples include mortar and artillery systems, as well as rocket-propelled-grenades (RPG) [4-6]. The availability of small, low-cost seeker systems opens the door to employing them – not only on these and similar tactical munitions, but also on various supply packages, and a myriad of other civil and military applications.

1.1.2 Scenario/Mission Overview

A low cost (< $12,000) seeker system is required for tactical strike packages employed in urban warfare environments subject to radar and GPS jamming. The thesis will consider three separate tactical package velocities (Mach 0.2, Mach 0.4, and Mach 0.6) with three separate target ranges (5 km, 7.5 km, and 10 km) in order to ensure that the system is capable for multiple platforms in various situations. The ordnance will originate from one of several launch/release platforms (aerial, artillery unit, RPG). The package will be released or fired from a distance of 5-10 km to the desired target so as to impact its target within 60 seconds from the call-for-fire. The munition will initially be guided towards the target by an IMU directing the ordnance along a designated flight path in accordance with the target's pre-set, estimated coordinates. The IMU

will place the projectile within an "acquisition basket", a location and orientation that will place the target signature within the seeker's field of view (FOV). Once the seeker optical sensor detects a laser designation signal illuminating the target and reflected off it, roughly 10 sec before impact, the projectile's flight path control will be transferred to the terminal seeker system. The seeker will guide the projectile to impact by homing in on the laser illuminated target. The weapon will impact the target precisely, causing little to no collateral damage. Figure 1.1.1 is a pictorial representation of the mission for which the seeker system is required. The drawing is not to scale [7].
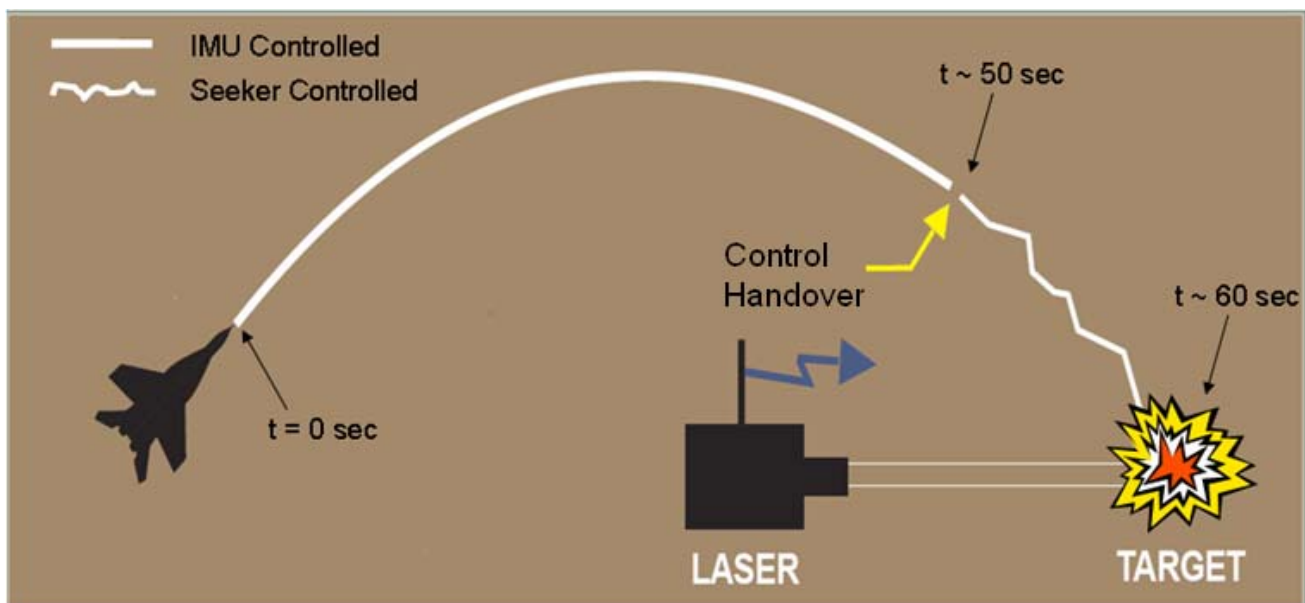
Figure 1.1.1 Generic Tactical Scenario

1.1.3 Requirements, Constraints, & Assumptions

With humanitarian concerns at the forefront of today's military doctrine, weapon precision and accuracy are paramount requirements for all armed operations. This constrains the seeker to meet an ordnance impact accuracy requirement of no more than 1.5 m circular error probable (CEP). At the same time, the seeker system cost needs to be low to justify its use (on the basis of cost-benefit analysis) and for the seeker to be competitive in the marketplace. A

$15,000 cost ceiling for the total seeker system appears to be a reasonable cost goal to achieve the required 1.5 m CEP performance for the above mission.

Furthermore, since the seeker is being designed for use on tactical munitions, the total system assembly must fit within an ordnance package 4" in maximum circular diameter, weighing 50 lbs or less. Lastly, while the mission of this seeker system is somewhat broad, its most likely use will be in providing support for troops on the ground. Therefore, promptness in ordnance delivery is extremely important for the safety of the ground personnel; consequently, a maximum of 60 seconds of total flight time from ordnance release to impact has been established as a requirement. Also for the safety of the individual operating the laser designation system, of these 60 seconds of flight, the seeker head will only control the projectile for a mere 10-12 seconds during which time the target will need to be illuminated with the laser.

For this study, the target is assumed to be stationary. Also, the seeker system design is strap-down, and not gimbaled. It is assumed that GPS jamming is present in the vicinity of operations, so on-board GPS aided guidance is denied within 3 km of the target. GPS, however, is available at the launch platform at the time of deployment, which provides an accurate fix on true launch position. The laser designation wavelength is 1.064 μm, which is wholly out of the visible range [8], so its detection by an adversary is unlikely. Also with respect to the designation system, it is assumed that the laser spot size is smaller than the target it is designating, preventing any confusion in the target designation from an over-spilled signal. Finally, it is assumed that the optical seeker head has an unobstructed view along its line-of-sight to the target, allowing the seeker to lock on to the laser designated spot/emitted target signature.

Lastly, from a strategic perspective, the analysis does not include any command and control issues associated with the type of engagements in which precision guidance systems are involved. The distribution and assignment of targets to those utilizing guided systems is a multifaceted endeavor that is updating and changing constantly during any operation. The thesis analysis assumes that all pertinent communication among the personnel involved is complete and that a target has been agreed upon.

1.2 Thesis Scope

This thesis establishes a design methodology for a new, compact strap-down seeker assembly for guiding tactical munitions employed in short-range, rapid-response situations demanding precision and accuracy in delivering the ordnance packages to their intended targets.

The principal design elements include the following: (a) MEMS sensor/focal plane analysis and selection, (b) MEMS IMU analysis and selection, (c) Projectile dynamic modeling, (d) System design and integration.

The thesis also evaluates the cost vs. performance of the seeker design elements to achieve the most cost-efficient design. This is accomplished by performing the design space trade-offs necessary to achieve the mission requirements while optimizing selection criteria of accuracy, cost, and size/weight. Based on this design study, a final design is formulated and modeled.

2   Literature Review

2.1   Infrared (IR) Focal Plane Array Technology

A majority of seeker systems rely on some sort of imaging focal plane to provide the terminal guidance for an object. Infrared (IR) focal planes are a popular choice among the focal plane technologies because of their ease of use, difficulty of IR wavelength detection by an adversary, and low material cost. The following sections outline the properties and operating characteristics that allow these devices to be relied upon by guided projectiles.

2.1.1 Semi-Conductor Chemistry

As atoms merge to form a crystalline solid entity their outer energy levels overlap to create electron bands. The outermost band, and that with the highest energy, is called the valence band. Beyond this band is an "energy gap", followed by a conduction band, filled only with high-energy, thermally excited electrons [9]. In metals, the valence band and the conduction band overlap, creating the opportunity for the free movement of electrons, or conduction. With insulators, on the other hand, the gap is wide, making it extremely difficult for electrons to gain enough energy to traverse into the conduction band [9]. Semi-conductors, such as Silicon (Si), Germanium (Ge), Tin (Sn), and Lead (Pb), retain a band gap that is nominally between those of metals and insulators. With enough thermal energy input into the semi-conductor crystal, some (or all) electrons in the valence band will reach the required excitation level to cross into the conduction band. Each electron that is able to make the leap from the valence band to the conduction band leaves behind a positively charged "hole", which, along

with the electrons in the conduction band, helps contribute to the electrical conductivity of the material.

One is able to improve the electrical conductivity of a semi-conductor by a process called "doping". Doping involves the introduction of certain chemical impurities into the crystalline structure of the material [9]. Depending on the charge makeup of the valence band of the impurity, doping generally adds either an electron or a hole to the material, dubbed donors or acceptors, respectively. Adding an impurity with more electrons in the valence band than the original atom will donate more electrons to the conduction band and leave behind positively charged holes, creating an "n-type" semi-conductor. Adding an impurity with fewer valence electrons will do just the opposite, creating a "p-type" semi-conductor. This process effectively shrinks the band gap and allows for easier flow of electrons into the conduction band.

Nearly all imaging arrays available today are comprised of semiconductors in which an n-type material and a p-type material are combined in very close contact. This mating procedure creates what is called a P-N junction. This junction is shown in Figure 2.1.1. In a P-N junction, the opposite charge carriers (holes and electrons) diffuse through the interface, eliminating each other in a process called recombination. Near the interface, however, the diffusion is stopped by an electric field created by the recombination process, leaving the remaining ions congregated tightly on both sides an area referred to as the depletion region [9].
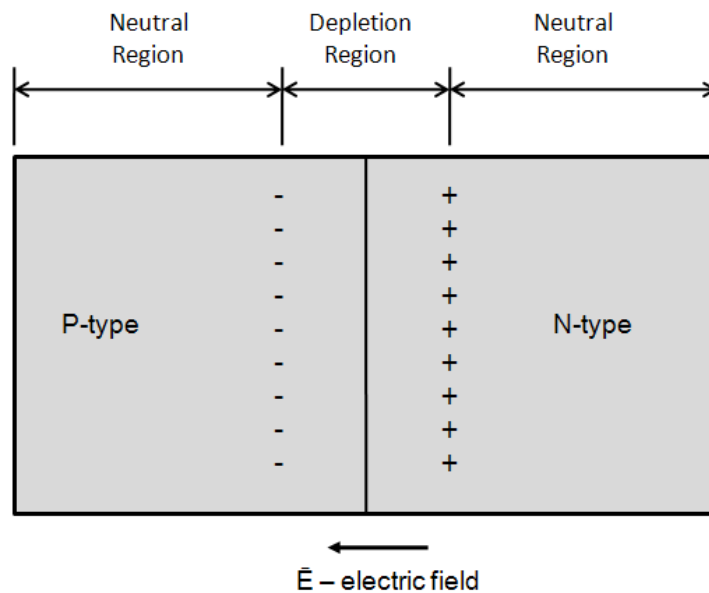
Figure 2.1.1 P-N Junction Illustration

2.1.2 Guided Munition Imaging Arrays

Photodiode arrays, which comprise CCD imaging arrays and other types of photodetectors and position sensing devices, are simply a combination of many P-N junctions arranged in a 2-D matrix. When a sufficient energy source, such as a photon or group of photons, strikes the surface of the photodiode array, it is able to excite an electron within the depletion region to create a mobile electron and a positively charged hole. These charge carriers are subsequently forced to exit the depletion region by the inherent electric field, producing a photocurrent through an external circuit that is proportional to the amount of energy incident on the surface of the photodiode array [10]. This phenomenon is called the photovoltaic effect and is the operating principle of many photodetection applications, to include the detection of a laser designation signal in guided munitions. In this manner, one is able to place a photodiode array at the focal point of a lens in the head of a guided munition to sense the amount of energy at a specific wavelength within the lens' field of view.

The material choice for the focal plane itself will vary with the application for which it is employed, the operating environment, as well as the desired wavelength. The differing band gap energies of the semi-conductor materials determine the separate wavelengths to which they are sensitive. Materials comprising the most widely used photodetectors for guided munition applications are Silicon, Indium Gallium Arsenide (InGaAs), Germanium, and Lead Sulfide (PbS). These specific materials are so widely used because they respond well to the laser wavelengths currently used to paint a desired target, which is usually between 1-1.5 μm [7]. Table 2.1.1 outlines several characteristics of these common photodiode device materials [10].

Material	Operating Temp (K)	Min λ (μm)	Max λ (μm)
Si	300	0.19	1.10
InGaAs	300	0.80	2.60
Ge	193	0.40	1.70
PbS	253	1.00	3.50

Table 2.1.1 Operating Characteristics of Photodiode Materials

Generally, it will not suffice to merely sense the target signature amongst its surroundings. Focal planes on guided muntions must provide some position sensing/correcting capabilities in order to direct the projectile's flight control system toward the target. For this reason, many infrared focal planes are divided into four separate regions, called quadrants,

separated by a IR insensitive material approximately a few μm thick. Commercial quadrant detectors, shown in Figure 2.1.2(a) [11], sense the signal intensity on each of the four elements to determine the true position of the incoming radiation signature. The *(x,y)* position of the IR signature described by Figure 2.1.2(b) is calculated by a weighted average of the output photocurrent values according to equations 2.1.1 and 2.1.2 [12],

$$x = \frac{(I_{X2} + I_{Y1}) - (I_{X1} + I_{Y2})}{I_{X1} + I_{X2} + I_{Y1} + I_{Y2}} \frac{L_X}{2} \tag{2.1.1}$$

$$y = \frac{(I_{X2} + I_{Y2}) - (I_{X1} + I_{Y1})}{I_{X1} + I_{X2} + I_{Y1} + I_{Y2}} \frac{L_Y}{2} \tag{2.1.2}$$
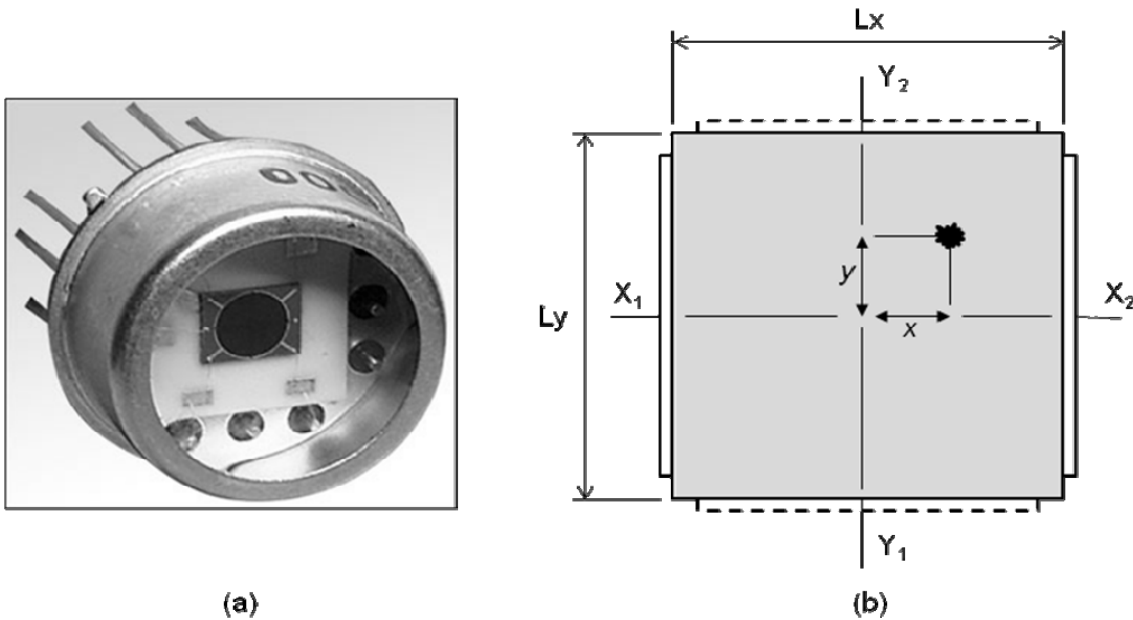
Figure 2.1.2 (a) Quadrant Detector Assembly, (b) Division of Active Area

where I_i is the output photocurrent at node i, and L_x and L_y are as shown in Figure 2.1.2. The coordinate outputs from the quadrant detector are proportional to the missile's heading error to the target and are supplied to the guided munition's flight computer to prompt control surface actuator deflections. These control surface corrections will center the beam (effectively zeroing the heading error) on the focal plane to ensure that it is on a collision course with the target. Figure 2.1.3 depicts how the heading error relates to the coordinate position of the laser designation signal.
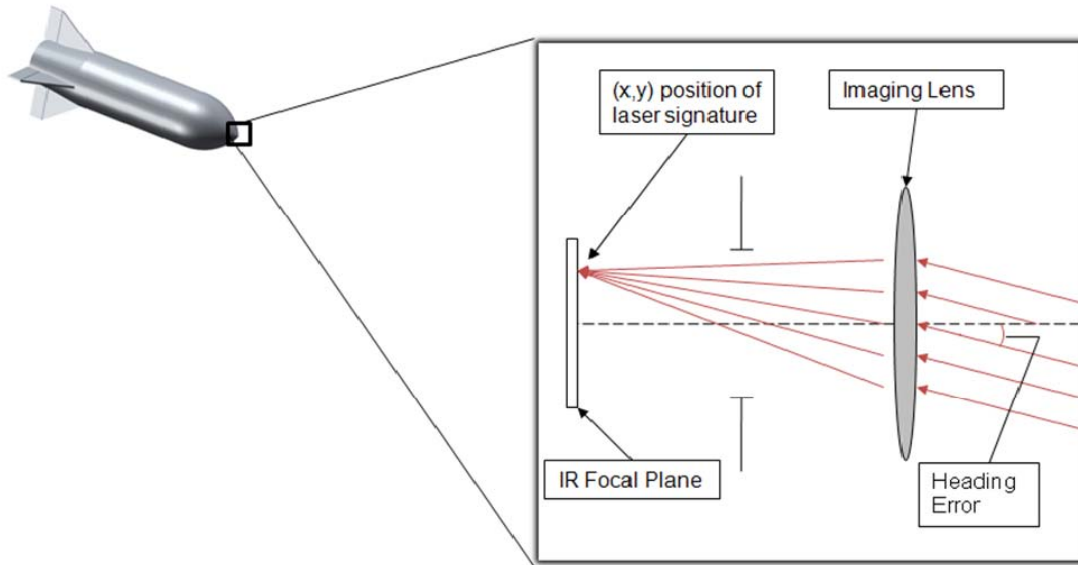
Figure 2.1.3 Expanded View of Seeker Optics

2.1.3 Photodiode Array Performance Parameters

Within the spectrum of the guided munition applications there are several performance parameters that are critical to the success of a quadrant photodiode array. These are responsivity, dark current, and noise-equivalent power (NEP).

Responsivity, or photosensitivity, is a detector proportionality constant that relates the output photocurrent to the incoming signal power. The units of responsivity are *Amps/Watt (A/W)* and typical photodiode responsivities vary along the sensitive wavelength band of the detector. Silicon photodiodes exhibit responses from the UV portion of the EM spectrum, through the visible wavelength range in into the near-infrared wavelengths. A typical responsivity plot is shown in Figure 2.1.4 [12]. For low light applications, or low EM power, responsivities may be too low to output an appreciable photocurrent. In this situation, the photodiode must include a gain to the incoming photons to achieve a photocurrent that is above the NEP. Avalanche Photodiodes (APD's) provide this gain as their makeup allows for internal multiplication, or "avalanching", of individual photons striking the focal plane. When considering use in precision guided munitions, the photosensitivity must be at a sufficient level to allow the focal plane to adequately recognize the target signature amidst both background and internal noise.
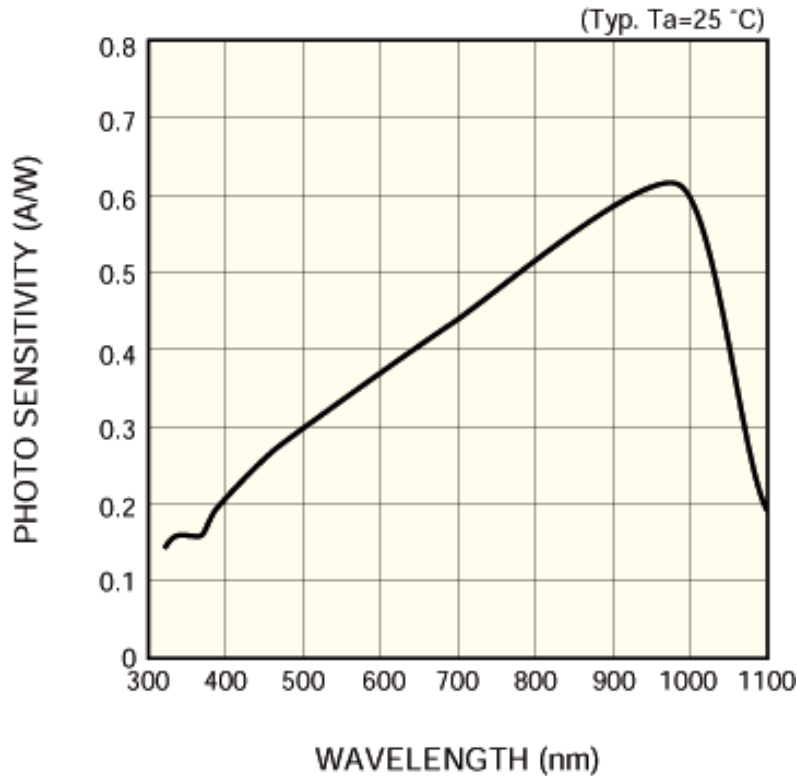
Figure 2.1.4 Photosensitivity Curve for a Hamamatsu Photodiode Array

Dark current refers to the photocurrent produced within the detector when no EM radiation is incident on the detector face and a reverse voltage is applied across the photodiode circuit junction. It is analogous to placing the detector within a "dark box" and measuring the output. Dark current arises due to natural imperfections in the processes and materials of a device's manufacturing, and contributes to the inherent noise of the detector. For the majority of detectors utilized in precision guided munitions, dark current is the dominating factor in the NEP calculation.

Assuming that the signal power eclipses the background power of a target's surroundings, the NEP generally refers to a weighted average of detector shot (photon) noise, dependent upon the dark current, and Johnson noise, dependent upon the temperature of the detector's operating environment. Both of these quantities will be developed in more detail in a later section.

2.2 Inertial Sensing Technology

Inertial sensors (IMU's) also retain an important role for precision guided munitions. Whereas the seeker focal plane provides the terminal guidance capability for the ordnance, the IMU must provide the initial and midcourse guidance when the target signature is too weak for the focal plane to recognize or is not transmitting due to safety considerations for personnel on the ground or in the air. An IMU measures the rate of rotation and the acceleration of the munition to provide accurate position estimation when GPS or seeker capabilities are not available. These mechanisms have been utilized on a myriad of platforms for quite some time [13].

In recent history there has been a trend towards developing MEMS gyroscopes and accelerometers to replace the traditional inertial sensing tools. MEMS components do not employ different measurement techniques from their macro-scale counterparts, they simply operate on a much smaller scale while offering vast cost reduction and improved performance functionality over the previously conventional devices. With respect to munition guidance applications, in particular, MEMS IMU's are becoming increasingly relied upon to provide inertial guidance because of their small size and attractive cost and performance features. The following subsections discuss MEMS inertial sensing principles of operation, and also detail how these micromachined systems are classified and used with respect to precision guidance applications.

2.2.1 Theory of Operation

At the simplest level, an IMU is designed to provide two distinct quantity measurements, linear acceleration and rotational rate. For most applications, it achieves these inertial measurements about the three body axes of roll, pitch, and yaw (figure 2.2.1), by placing a combination of accelerometers and gyroscopes, aligned in the proper orientation, within its housing and attaching it to the body of interest. As the nomenclature suggests, the accelerometers measure linear body acceleration along a particular axis while gyroscopes measure the rotational accelerations about the airframe's body axes. Missile body and angular accelerations are measured and fed from the IMU to a flight computer in order attain accurate position information. As this information is crucial to the success of any guided system, the

guidance system designer must have an adequate understanding of the process by which the individual measurements are transformed into useful position information.
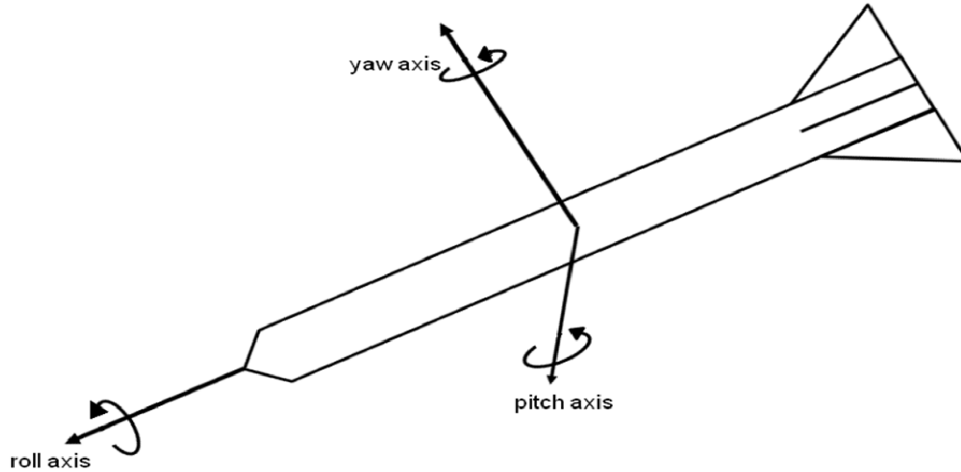
Figure 2.2.1 Body Fixed Axes for Missile Applications
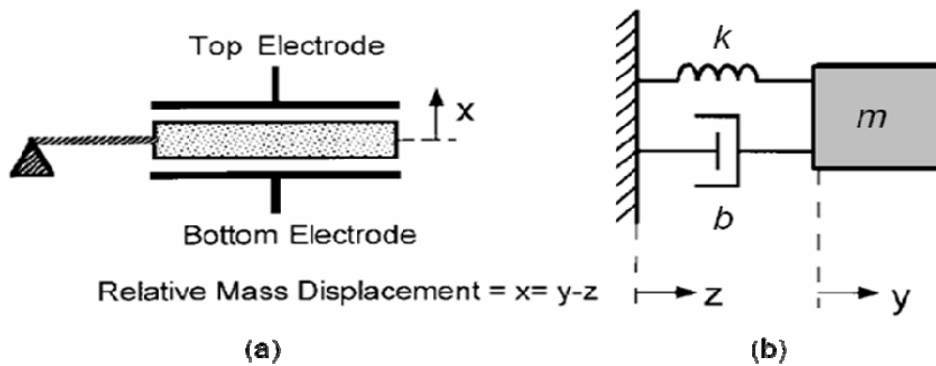
Figure 2.2.2 (a) Generic Accelerometer Structure, (b) Equivalent Mechanical Model

There are several different types of MEMS accelerometers, but all generally contain a proof mass, m, attached to a fixed frame by some sort of rigid beam and a damping mechanism [14]. The rigid beam has a spring constant, K, while the damping factor is denoted by b. Thus, a generic MEMS accelerometer can be modeled as a second order mass-spring-damper system. Figure 2.2.2, from reference [14], shows the structure and equivalent model of this system

description. Modeled as a second order system and using Newton's 2nd Law, the system can be decomposed into the following second-order transfer function:

$$\frac{x(s)}{a(s)} = \frac{1}{s^2 + \dfrac{b}{m}s + \dfrac{k}{m}} \qquad (2.2.1)$$

where a is the acceleration imposed on the structure, and x is the proof mass displacement. Adjusting the parameters of this equation allow the designer to control the sensitivity, resonance, and even noise resistance of the accelerometer. With this relationship, one simply needs a method of sensing the proof mass displacement to obtain the acceleration output.

Many methods exist to sense the motion of the proof mass. These include using piezo-resistive devices, capacitive devices, tunneling devices, resonant devices, thermal devices, piezo-electric devices, and electromagnetic devices. Reference [14] describes each of the sensing methods in detail. Also, new sensing methods are currently being researched for improved performance. In fact, Draper Laboratory is conducting research to develop a cold atom accelerometer capable of extreme sensitivity.

The majority of accelerometers used in missile guidance applications, however, typically fall under one of two categories: pendulous mass capacitive devices or resonator devices [13]. When experiencing an external acceleration, the support frame of a capacitive accelerometer deviates from its equilibrium position. The motion causes the capacitance between the proof mass and a fixed electrode, separated by a very small gap, to vary proportionally with the size of the gap. The fluctuating capacitance is measured by a readout circuit and then converted into an acceleration measurement via a proportionality constant. This sensing method offers very high resolution, allowing for the measurement of incredibly small acceleration deviations, and low nose susceptibility, making them very attractive for inertial guidance purposes [14]. In resonant accelerometers, two parallel beams are attached to the proof mass and are excited with high frequency vibrations. The proof mass is attached to these beams, placing one in tension and the other in compression. In the presence of acceleration, the frequencies at which the beams oscillate will deviate from their original values. The acceleration is then calculated according to the resulting difference in frequencies, multiplied by a scale factor [13]. Figure 2.2.3 shows the two accelerometer types, as fabricated within Draper Laboratory.
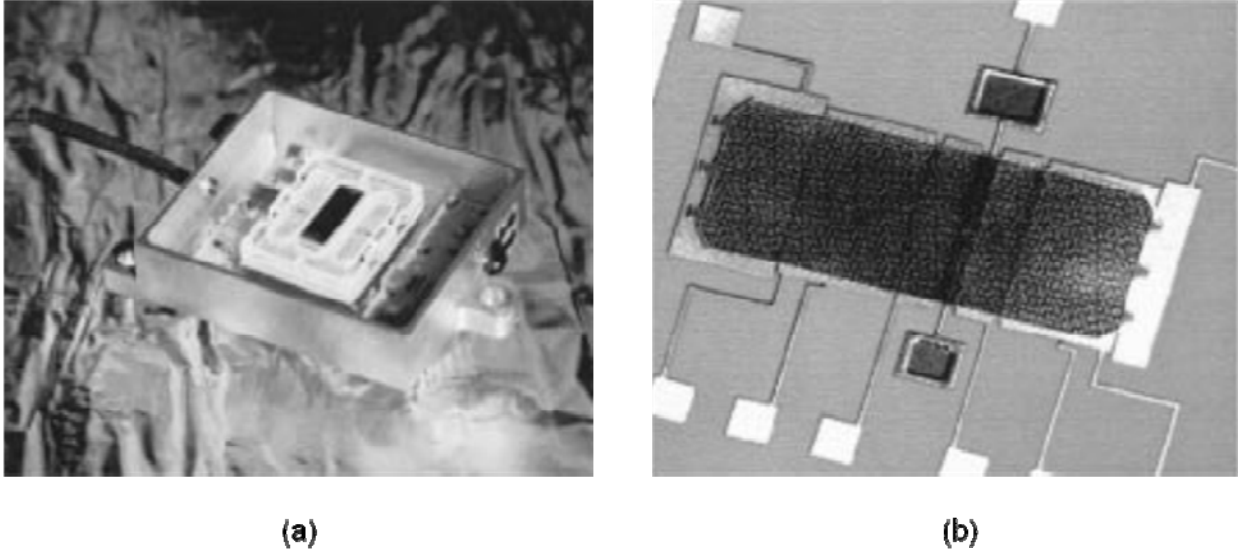
Figure 2.2.3 (a) Draper Quartz Resonant Accelerometer, (b) Draper Pendulous Mass
Accelerometer

Like their accelerometer counterparts, there are many types of MEMS gyroscopes
available on the commercial market. However, nearly all operate with some sort of vibrating
mechanical element to sense rotation. Examples include a collection of tuning forks, a vibrating
beam, a vibrating ring, or a vibrating shell [14]. Regardless of the vibrating element, all MEMS
vibratory gyros operate on the principle that an angular rate applied to a moving body produces a
Coriolis force is upon the body [13]. The Coriolis force is described as an apparent force that is
exerted upon a body in a rotating reference frame, and is proportional to the angular rate. Figure
2.2.4 depicts the generation of a Coriolis acceleration on a particle traveling in a 3-D rotating
reference frame. In the figure, Ω is the rotation rate of the reference frame, $\vec{V}$ is the velocity of
the object of interest, and $\vec{a}_{cor}$ is the generated Coriolis acceleration calculated as follows [14]:

$$\vec{a}_{cor} = 2\vec{V} \times \vec{\Omega}$$
(2.2.2).

Though there are several types of gyros, the tuning fork gyro is a typical example and the
operating principles are easily transferred to the other types. Generally, a MEMS tuning fork
gyroscope, like the one shown in figure 2.2.5, is fabricated by producing a comb of tuning forks
that are excited by a resonating vibration along what is called the "drive" axis. The drive axis

29
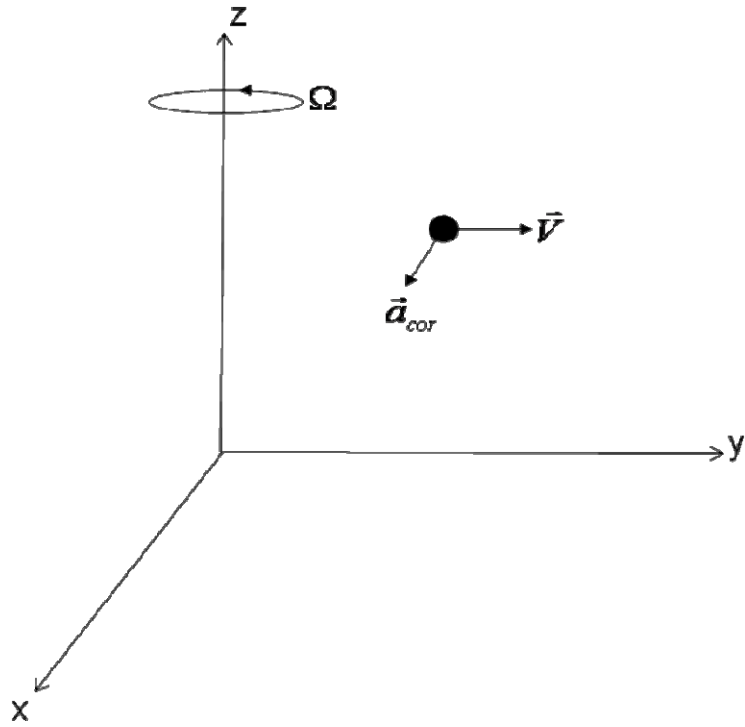
Figure 2.2.4 Apparent Coriolis Acceleration Generated in a Rotating Reference Frame
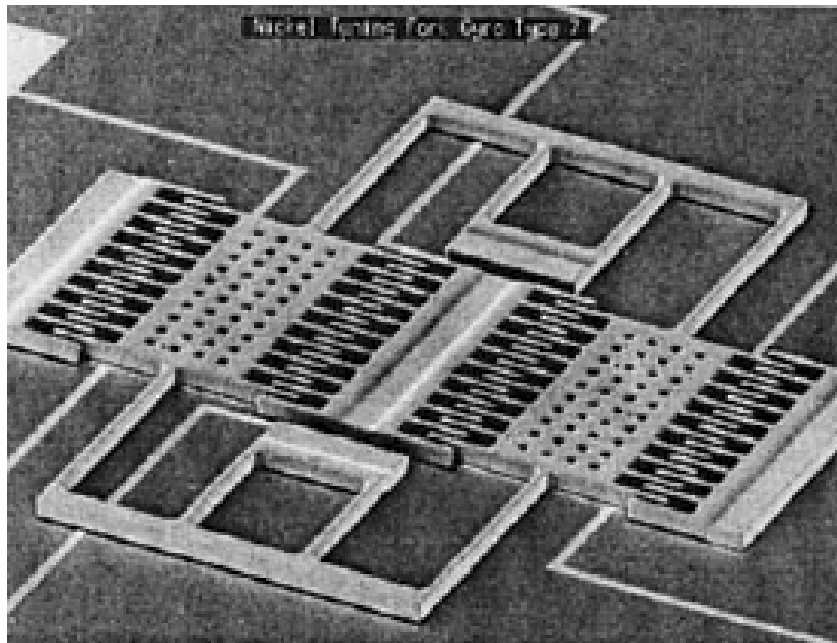
Figure 2.2.5 Draper Lab's first comb drive tuning fork gyroscope

runs parallel to the length of the tuning fork tines. When subject to rotation, the Coriolis acceleration produces torsional forces on the tines, orthogonal to the input vibration along the "sense" axis. The Coriolis force produced along the sense axis causes proportional tine displacements that can be measured capacitively, piezo-electrically, or piezo-resistively [14]. Subsequently, given the mass of the tuning fork tines, the resulting angular rate of the body is obtained using the acceleration calculation in equation 2.2.2.

In missile guidance, the output angular rate measurement is then utilized within the control loop to ensure that that the ordnance position is consistent with a predetermined flight trajectory. Certainly, gyroscope measurement methods are not limited to the vibratory example provided above. In fact, the most accurate gyroscopes commercially available are optical in nature. Ring laser, and fiber-optic gyroscopes, offer vast accuracy improvements over micromachined vibratory gyros [14]. However, these device types are generally bulky and very expensive, making them unattractive for low-cost, small sized applications, such as tactical missile guidance.

On the other hand, while designed to measure rotation, MEMS vibratory gyroscopes do not contain any rotating elements, a key design factor that allows for monolithic batch fabrication possible (generally out of quartz or silicon). The bulk fabrication process is very efficient; in fact, a single 5-in^2 wafer of silicon is able to produce several thousand MEMS gyroscopes [13].

2.2.2 IMU Performance Parameters

The gyroscopes and accelerometers contained by an IMU package dictate the performance of the individual unit. There are several parameters used to describe the performance of an IMU. These include bias (in)stability, angular random walk, scale factor accuracy, and dynamic range.

Bias is the non-zero output of the IMU when it is stationary, or should have a zero output. This quantity also varies in operation is extremely critical to the operational success of the platform that it is employed upon. If the bias were invariable, it could be accounted for and corrected externally. However, external phenomena, such as temperature variations, cause the bias to fluctuate over the course of operation and result in acceleration and/or rate measurements

that deviate slightly from the true values. Bias stability, or instability, is the fundamental determinant of the specific grade of an IMU (rate, tactical, inertial) and is often expressed in *°/hr (or rad/hr)* for angular rate and *milli-g* for acceleration.

Angular random walk in an IMU is the second most dominant factor contributing to the amassed error of the unit during operation. This term refers to the propagation of measurement error over the course of IMU flight. It can be thought of as the variation of the integrated output of a stationary IMU over time. The units are expressed as either *°/hr* or $°/\sqrt{hr}$ *(rad/hr or* $rad/\sqrt{hr}$ *)*.

The scale factor accuracy relates to the repeatability of a measurement. The transduction of the input acceleration or angular rate into an output signal is accomplished by a scale factor. Ideally, the scale factor is identically one value. However, imperfections cause the scale factor to vary. In practice, a varying scale factor may result in two different angular rate measurements when in reality the body is rotating at the exact same speed in both instances. Scale factor accuracy is generally expressed in units of parts-per-million (*ppm*) or percentages.

Dynamic Range refers to the range of acceleration or angular rate that an IMU is able to successfully sense. For example, and IMU may be able to sense a range of ± 300 *rad/s* in angular rate and an acceleration range of ± 1000 *g*. Angular rates or accelerations with magnitudes greater than these values will saturate and the device will output the maximum specified measurement value.

2.2.3 IMU Classification & Application

MEMS inertial sensors have a myriad of consumer, industrial, and military applications. They are used for digital camcorder stabilization (consumer), machine vibration monitoring (industrial), and missile navigation and guidance (military), just to name a few [14]. Despite the vast array of uses, IMU's are generally classified into one of three performance based categories: rate grade, tactical grade, and inertial grade. These classifications spring from the equivalent labels placed upon the gyroscopes within the IMU packaging. Accelerometers contained by an IMU used for any navigation purpose fall within one performance category, navigation grade. While the specifications may vary for navigation grade accelerometers, they are somewhat less

volatile than those of gyroscopes, hence the IMU category nomenclature. Rate grade IMU's are used primarily in the consumer world and in automotive applications, as they are extremely cheap. Tactical and inertial grade IMU's find use mainly for navigation and guidance, including precision missile guidance [14].
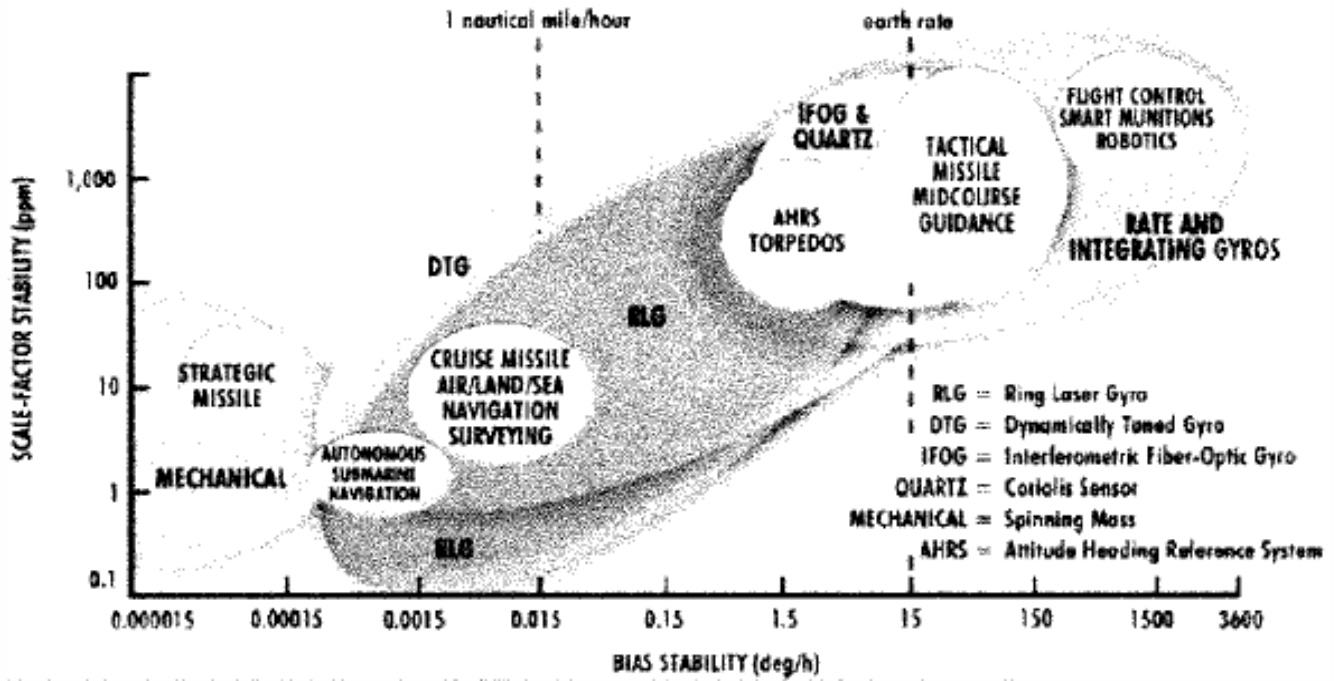
Figure 2.2.6 Gyroscope (IMU) accuracy mapped with accompanying applications

Tactical grade components are employed on aided (with GPS or seeker) smart munitions, while the more expensive inertial grade components are generally utilized for unaided cruise and strategic missiles. Currently, MEMS IMU's are classified in the rate and tactical categories. Reference [13] includes a figure that shows a recent depiction of the state of gyroscope (and IMU) performance along with applications mapped on the same axes. On the x-axis is bias stability, and on the y-axis is scale factor. As expected, unit price is inversely proportional to device accuracy. Thus, as figure 2.2.6 illustrates, MEMS gyros are suitable for a limited number of applications. The current state of the missile guidance industry demands that MEMS IMU's be aided in some fashion due to their inherent inaccuracies.

While developments have seen MEMS gyros achieve inertial grade accuracies, the price for such high performing units remains substantially high. It is the focus of ongoing research to

improve MEMS device accuracy while still allowing for batch fabrication and low unit costs. Promisingly, this research continues to produce more accurate MEMS IMU's coupled with falling price tags. The industry trends suggest that in the near future MEMS IMU's will become the staple on all platforms, perhaps even as stand-alone guidance systems. Until then, MEMS IMU's will likely continue to require the external aid of GPS or a terminal guidance seeker system to be successful for most applications.

3 Analysis and Modeling

3.1 Overview

The analysis and modeling portion of this thesis design study focuses on the three elements listed in section 1.2: (a) MEMS sensor/focal plane analysis, (b) MEMS IMU analysis, (c) Projectile dynamic modeling. Each analysis element is undertaken in order to determine the hardware component performance necessary to meet the mission requirements. While each of the individual investigations of the hardware elements that will make up the system are specifically geared toward the thesis scenario, the author concurrently attempts to go about each component breakdown in a broad manner to lay out an overall design methodology. In this manner, the same logical progression can be used for slightly different design scenarios.

3.2 Optical Sensor Analysis

The optical sensor design and selection is paramount to meeting the requirements of the proposed seeker system's mission. The focal plane must be able to acquire a target signal and, based on the incoming signal, translate the error in the estimated position to the vehicle control system for flight corrections. This action requires fast sensor response times due to the short time window allowed in the seeker controlled portion of flight, as well as adequate performance to distinguish the desired designator signal from the detector from the background noise present.

3.2.1 Requirements

The optical sensor requirements, like those of the other components, flow down from the mission requirements. Because the control handover from the IMU to the seeker head occurs approximately 10-12 seconds from impact, the sensor must distinguish the target from its surroundings at a minimum distance of 1 to 1.5 km. Also, due to the interdependence of the sensor field of view (FOV) and the IMU drift rate, it is important to specify the FOV for subsequent analysis. A minimum sensor FOV of 30° has been selected. Lastly, because the sensor will lock on to the strongest signal within its FOV, a minimum signal-to-noise ratio of 2 (6.00 dB) has been specified at the time of control handover.

3.2.2 Signal Calculations

In designing the focal plane to detect infrared radiation from the pulsed laser designator, one must not only take into account for the fraction of the laser signal arriving at the focal plane surface of the detector, but also the accompanying background radiation at the wavelength of interest contributed by the ambient environment. Figure 3.2.1, from reference [15], illustrates the generic scenario being considered for this analysis. The desired laser signal strength at the detector is derived first.

The output parameters of the designator used for this analysis are typical of systems currently employed for military use [7]. These specifications are listed in Table 3.2.1.

Output Wavelength, λ	1.06 - 1.54	μm
Bandwidth	0.00045	μm
Output Energy, E	80 - 100	mJ
Pulse Duration, t_p	1.0E-08	sec
Beam Divergence	0.15 - 0.30	mrad

Table 3.2.1 Typical Laser Designation System Specifications

As shown in Figure 3.2.1, this analysis assumes that the target designated is much larger than the incident laser beam, so that the entire incident beam is scattered by the target with no overspill onto the surrounding area.
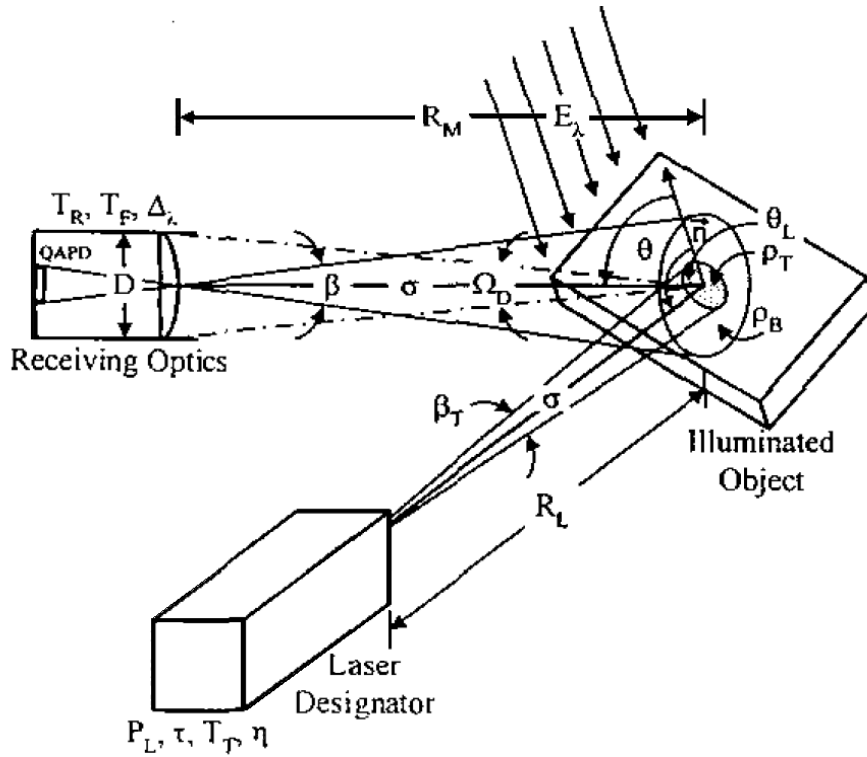
Figure 3.2.1 Simplified Laser Signal Transmission to Detector

The output power for the laser is obtained by dividing the output energy, in units of mJ, by the pulse duration to convert to power in units of Watts. Using the parameters from Table 3.2.1, the output power is given by:

$$P_L = \frac{E}{t_p} \tag{3.2.1}$$

This signal power, upon traversing the path from the designator to the target surface, suffers loss as a result of atmospheric attenuation. According to Beer's Law in equation 3.2.3, the incident power is a function of the distance from the source to the target (R_L) and the atmospheric attenuation coefficient (γ) at the laser wavelength [15]. The attenuation of near infrared (NIR) wavelengths is largely caused by the absorption and scattering of the beam by water molecules present in the atmosphere [16]. Therefore, the laser signal attenuation is highly dependent upon the relative humidity (RH) of the laser's surrounding environment. Experimental data from a Naval Research Labs report titled "Atmospheric Attenuation

Coefficients in the Visible and Infrared Regions", [16], show that γ is exponentially proportional to relative humidity. The following relationship was derived from that data:

$$\gamma = 0.074216 \cdot (1 - RH)^{-0.3717} \qquad (3.2.2)$$

Figure 3.2.2 depicts equation 3.2.3 in graphical form.
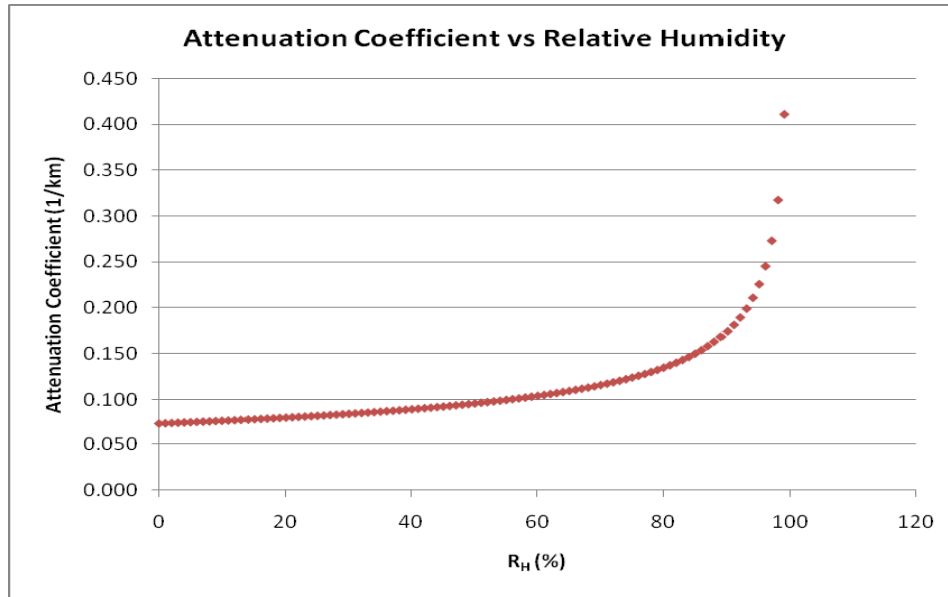
Figure 3.2.2 Relative Humidity vs Attenuation Coefficient at 1.064 μm

Beer's law now provides the attenuated signal power received at the target:

$$P_T = P_L \cdot e^{-\gamma \cdot R_L} \qquad (3.2.3)$$

This incident laser signal is then scattered from the target surface. While the majority of surfaces exhibit both specular (directional) and diffuse (equal in all directions) reflection (Figure 3.2.3, [17]), this thesis limits itself to targets having perfectly diffuse (or Lambertian) reflection characteristics. Reference [18] provides a detailed discussion of diffuse and specular reflection.

Making the conservative assumption that the target surface is perfectly Lambertian requires that the designed focal plane be able to detect a minimum scattered power (the diffuse value). Many materials present candidate surfaces for the designated target; however, because this thesis is designing a seeker for an urban environment, the choices have been limited to those listed in Table 3.2.2.

Ideal Diffuse Reflection
(Lambertian Surface)

Diffuse Reflection with
Specular Component
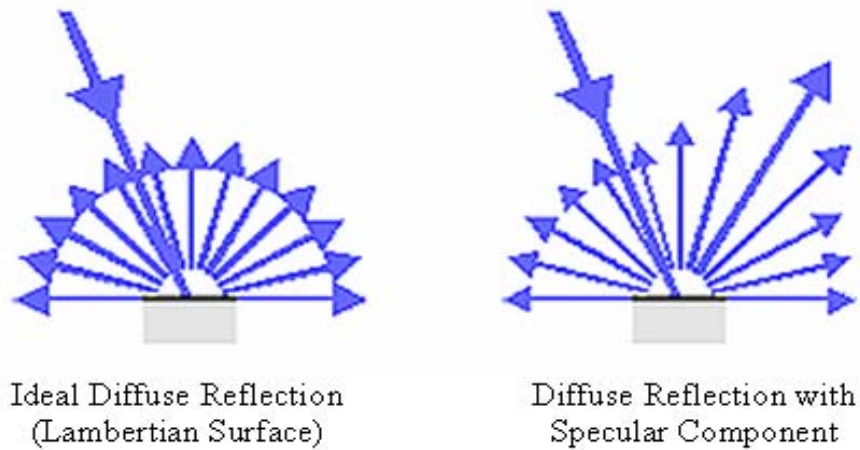
Figure 3.2.3 Surfaces Exhibiting Diffuse and Hybrid Reflection

Material/Surface	ρ_T
Concrete	10 - 20%
Asphalt	10 - 25%
Unpolished Aluminum	55%
Vegetation	30 - 70%
Brick	55 - 90%
Limestone, clay	60-75%
Carbonate sand (dry)	57%

Table 3.2.2 Example Target Diffuse Reflectance Values

Given the incident power and the target's reflection characteristics, the fraction of the diffusely reflected radiation captured by the detector (dP_T) is calculated by applying a solid angle function [10]. This function determines the radiation exchange between two areas, the target surface and the focal plane of the detector. The final reflected power value is dependent upon (a) the areas of the source and detector (dA_s & dA_d), (b) the angle between the target normal and the incident designator signal (Φ) and (c) the angle between detector's focal plane normal and the vector from the detector to the source (θ). See figure 3.2.4 for a cartoon illustration of these parameters, the drawing is not to scale. The solid angle calculation is carried out according to equation 3.2.4 [10].

$$dP_T = \frac{P_T dA_S \cos(\Phi) dA_d \cos(\theta) \rho_T}{\pi R^2} \quad (3.2.4)$$
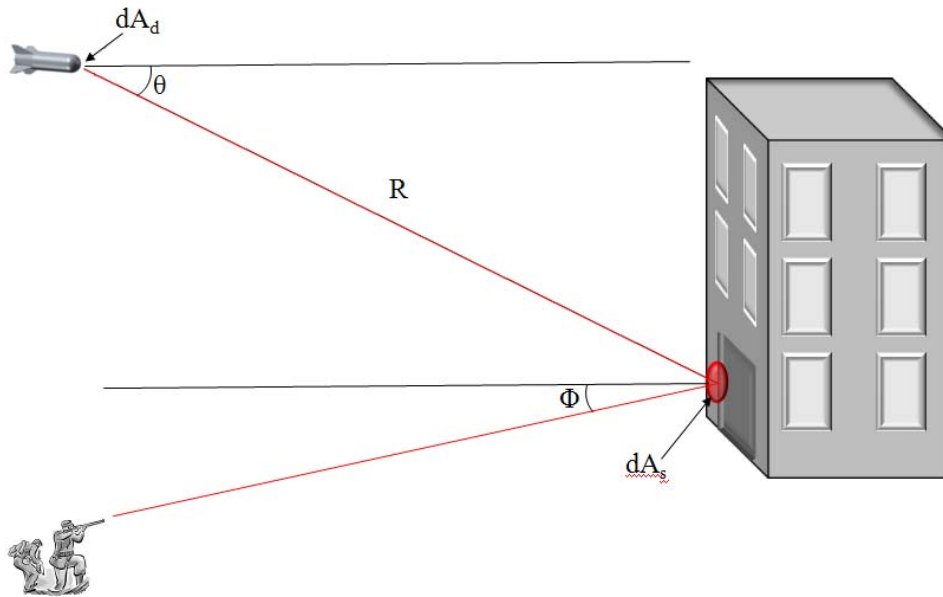
Figure 3.2.4 Solid Angle Cartoon Illustration

The final consideration in calculating the detected power level is to factor in atmospheric signal attenuation along the path from the target to the focal plane using equation 3.2.3, by inserting the distance from the target to the sensor's focal plane in the exponential term.

The methodology described in this section was compared to several other methods listed in literature to confirm the validity of the selected approach [15, 19, 20]. A sample calculation employing the several methods was conducted for a common generic scenario. The results outlined were largely consistent with each other, and are presented in the table below.

	Detected Power (W)	% Difference
Selected Method	2.30E-05	N/A
Published Method #1	2.30E-05	0.00 %
Published Method #2	2.62E-05	14.01 %
Published Method #3	2.70E-05	17.54 %

Table 3.2.3 Comparison of Calculation Methods

The larger differences between the selected approach and methods 2 and 3 are attributed to the more conservative assumptions involved with the author's technique of carrying out the calculations.

3.2.3 Noise Calculation

For a functioning system, the detector must be able to resolve the incoming signal power amidst the noise present. There are two types of noise to consider in the scenario under consideration, the background noise from the environment and the noise inherent in the detector. Background noise, from any hot-body emission or solar radiation reflection from the target's surroundings, degrades the desired signal resolution within the detector. So does detector noise, which arises from two sources: shot (or photon) noise, caused by fluctuations in the dark current of a photodetector, and Johnson noise, due to the thermal environment in which the detector is operating [10]. Background noise is addressed first.

Background noise from hot-body emission of radiation is not included in this analysis, since all terrestrial objects emit radiation only at infrared wavelengths above approximately 3.7 μm, far removed from the 1.064 μm laser beam wavelength of interest [20, 21]. So, only the solar irradiance reflected in a narrow 10 nm bandwidth straddling 1.064 μm is relevant for calculating the background noise collected by the detector. The calculation is very similar to that for determining the desired signal strength in section 3.2.2 above, the slight differences existing mainly as the source of radiation and the area of that source, which in this case equates to the entire area seen within the detector's field of view. The background noise can be calculated from the following expression [15]:

$$P_B = \frac{\pi}{16} E_\lambda \Delta\lambda \rho_B \beta^2 D^2 T_R T_F e^{-\sigma R_M} \tag{3.2.5}$$

where E_λ is the solar irradiance reaching the earth's surface, $\Delta\lambda$ is the 10 nm bandwidth, β is the receiving optics field of view, D is the diameter of the receiver aperture, T_R is the receiving optics transmission coefficient, and T_F is the optical filter transmission coefficient. All other variables are as described previously.

Values for E_λ at specific wavelengths can be found in references [22] and [23]. It should be noted that equation 3.2.5 calculates the background signal power under the assumption that it is emitted from a circular area at a normal range of R_M from the detector. The true footprint of the sensor's FOV, however, is elliptical, as illustrated schematically in Figure 3.2.5. The consequence of the elliptical footprint is such that part of the background signal is emitted from components located closer than R_M, and hence stronger than those emitted at R_M. However, by the same token, other portions of the elliptical area viewed from the sensor will be at distances greater than R_M, rendering that fraction of the IR power flux weaker than those at the target range R_M. The total background signal strength is simply that emitted from the elliptical FOV, circularly projected onto the sensor focal plane. The integrated value of the circular projection very closely reflects the value calculated using equation 3.2.5, making its utility valid for this scenario.

True "Guidance Footprint"   Assumed "Guidance Footprint"
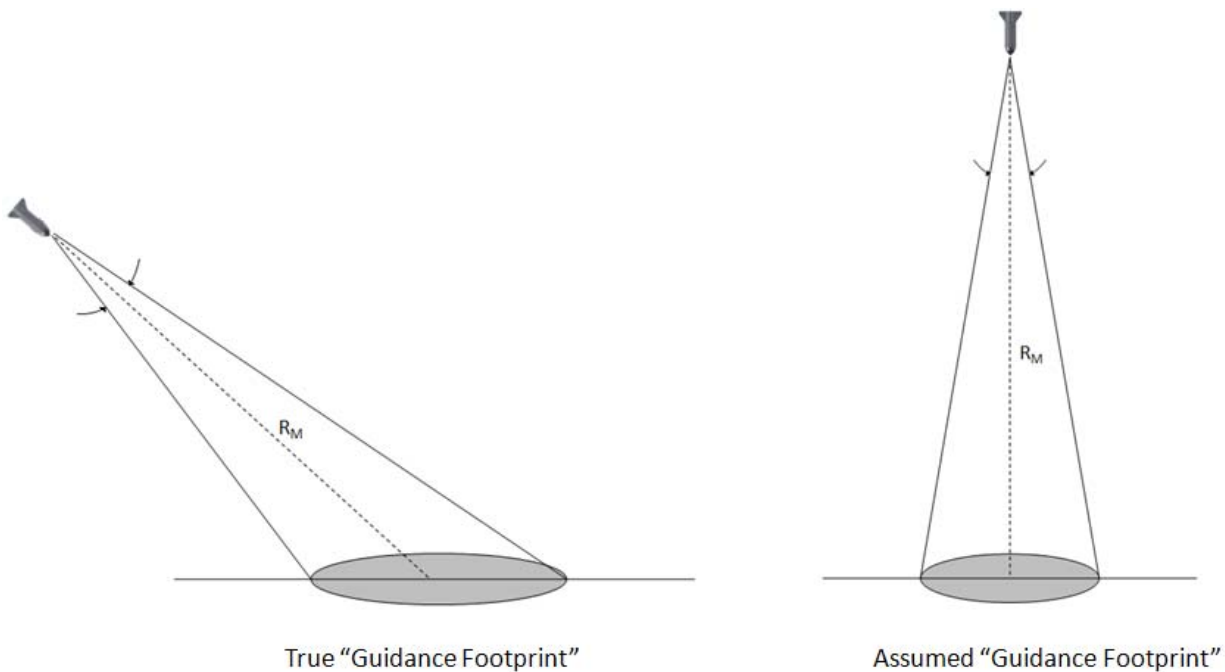
Figure 3.2.5 Guidance Footprint Comparison

A second caveat to this calculation is that the pulse repetition rate must be taken into account in the computation of accurate background noise levels. Reference [24] notes that for many systems, the sensor and designator work cooperatively, so that the sensor looks for the particular laser pulse repetition rate (PRF code) to distinguish its designated target from other clutter or countermeasures. The unique PRF codes allow multiple seekers (i.e. multiple

munitions) to be utilized in the same area with different designation systems; they also allow for increased SNR by collecting the signal only during the 10 ns pulse width of the designator. Equation 3.2.5 assumes that the noise signal is being continuously collected when in reality the sensor is acting as a shutter, periodically blocking out the noise during the time that the laser designation signal is not emitted. So, to account for the fact that the sensor will not be collecting incoming power continuously, the background power calculated in equation 3.2.5 must be multiplied by the PRF window function, or the ratio of time that the radiation is being collected (1×10^{-8}).

The inherent detector noise is also an important consideration in determining the maximum effective range of the sensor. The majority of infrared seekers utilize some variation of a silicon quadrant detector photodiode array to detect the designator signal and pass on its position information to the flight computer. The low end of the dynamic range for a quadrant detector is determined by the amount of the intrinsic noise in the detector. The noise levels of photodiodes operating with a reverse bias voltage in the photoconductive mode are dominated by shot (or photon) noise and Johnson noise [10]. The laser signal power at the detector must exceed the combined noise equivalent power (NEP) from these sources beyond a threshold SNR requirement of the detector in order to be recognized as the signal of interest.

Photodetector shot noise is calculated as follows [10]:

$$I_S = \sqrt{2eI_D \Delta f} \tag{3.2.6}$$

where e is the elementary charge of an electron (1.602×10^{-19} Coulombs), I_D is the dark current specific to the detector in Amps, and Δf is the bandwidth of the system in Hz. The Johnson noise is calculated [10]:

$$I_J = \sqrt{\frac{4kT\Delta f}{R}} \tag{3.2.7}$$

where k is Boltzmann's constant ($1.38 \times 10^{-23} \frac{kg \cdot m^2}{s^2 \cdot K}$), T is the operating temperature in Kelvin, and R is the detector shunt resistance in Ohms.

Having derived the signal power, as well as background and detector noise equations, the maximum range of the detector may now be calculated. This range value is highly dependent

upon the type of detector employed. In this thesis, the initial analysis was carried out using Hamamatsu, Inc. photodetectors as a baseline from which to build subsequent analysis. The signal and noise power levels were calculated across a broad spectrum of relative humidity in order to ensure proper detection under all conditions.

The following assumptions were made for the calculation process: the focal plane's field of view and detector aperture diameter are 30°, and 1", respectively, and 10% of the incident signal and background radiation is reflected from the target surface. Also, it may be recalled (section 2.3) that photodiodes produce a photocurrent proportional to the total signal power collected at the detector focal plane. The analyses were performed for a 2-D Hamamatsu Si photodiode array with a published photosensitivity of 0.4 A/W at 1.064 μm, and a Si APD with a photosensitivity of 30 A/W [12]. The following additional values from the Hamamatsu product data sheets, [12], were used for the detector noise calculations:

Dark Current, I_D	50	nA
System Bandwidth, Δf	45	kHz
Shunt Resistance, R	175	MΩ
Operating Temperature, T	323	K

Table 3.2.4 Photodiode Characteristic Values for Detector Noise Calculation

Calculating the detector noise for both sensor types according to equations 3.2.6 and 3.2.7 yielded a shot dominated detector noise of 2.7×10^{-11} A, equivalent to an NEP of 4.5×10^{-11} W. This may be compared with the highest possible background noise calculated according to equation 3.2.5 (including the window function) of 1.6×10^{-13} W, more than an order of magnitude smaller than the intrinsic detector noise. This means that the inherent detector noise establishes the threshold for detection of the scattered laser signal at the detector, which must exceed the shot-limited NEP.

From evaluating the signal strength at increasing distances for all levels of relative humidity, one finds that the desired signal matches the detector noise strength at a threshold distance of approximately 35.5 km (35 km horizontal distance, 5 km above the earth's surface) for a generic photodiode array. The APD nearly doubles this distance by adding the increased internal gain factor. Nevertheless, for both types of detectors, an SNR of greater than unity is required for the detector to distinguish the desired signal from its surroundings. While other

applications may have use for such large detection distances, the application presented in this thesis does not. Therefore, it is necessary only to consider the horizontal launch distance of 5 km defined by the mission constraints and a vertical launch distance of 2 km. If the detector is able to adequately sense the designated signal at this distance, the resolution and signal-to-noise ratio will only improve as the projectile progresses towards the target. Modeling of this scenario confirmed that while the APD produces larger photocurrents than the PSD, both photodiode arrays more than adequately meet the detection threshold requirements. The comparative results of each iteration are shown in tables 3.2.5 and 3.2.6, respectively.

Relative Humidity	Signal Current (µA)	Noise Current (µA)	SNR (dB)
30%	9.22E-01	2.68E-05	90.72
40%	8.91E-01	2.68E-05	90.42
50%	8.53E-01	2.68E-05	90.05
60%	8.06E-01	2.68E-05	89.55
70%	7.43E-01	2.68E-05	88.85
80%	6.52E-01	2.68E-05	87.72
90%	4.96E-01	2.68E-05	85.34

Table 3.2.5 Results for Hamamatsu PSD (5 km horizontal; 2 km vertical)

Relative Humidity	Signal Current (µA)	Noise Current (µA)	SNR (dB)
30%	6.92E+01	2.68E-05	128.22
40%	6.68E+01	2.68E-05	127.92
50%	6.40E+01	2.68E-05	127.55
60%	6.04E+01	2.68E-05	127.05
70%	5.57E+01	2.68E-05	126.35
80%	4.89E+01	2.68E-05	125.22
90%	3.72E+01	2.68E-05	122.85

Table 3.2.6 Results for Hamamatsu APD (5 km horizontal; 2 km vertical)

Recalling that the mission only calls for approximately 10 seconds or less of true seeker controlled flight, any distance beyond 1-1.5 km (the distance typically traversed by the projectile during 10 s) over which the detector demonstrates adequate sensitivity exceeds the requirement for threshold detection range. These results demonstrate that both types of detectors greatly surpass the requirement for SNR at the distances of interest. Accordingly, the extra gain (and cost) associated with the avalanche photodiode is unnecessary, so further consideration of APD detectors is omitted in later sections when searching for available or forthcoming technology to employ for the optical sensor in the designed seeker head.

3.2.4 Technology Survey

While the previous analyses were based on Hamamatsu Photonics Si photodiode arrays, other technology alternatives were examined for completeness. This section provides a comparison of the focal plane technologies currently available as well as those in development to determine which option best satisfies the design trades of performance and cost.

The majority of seeker assemblies currently in use employ Si quadrant photodiode detectors with the capability of centering the incoming radiation beam to achieve direct impact with the target. Numerous companies offer infrared detector technology as a product staple. Their photodiode array products and pricing are largely similar, with minor differences existing in product designed for certain specialized applications, such as laser alignment in control systems or the medical industry, or for laser guided munitions. The analysis in Section 3.2.3 has demonstrated that standard Hamamatsu photodiode arrays meet the mission requirements. Based on those results and the fact that virtually all photodetectors offer similar performance characteristics, it is reasonable to assume that a wide range of products are available for the mission of interest.

The next step is to maximize the performance of the sensor while attempting to minimize the cost. This design trade analysis can be made possible by comparing the performance specifications of the current photodiode technologies offered by the various manufacturers. The next few paragraphs will focus on providing a brief overview of competing state-of-the-art focal plane array technologies.

Photosensitivity

Typical responsivity for Si detectors at a wavelength of 1.064 μm is 0.3-0.4 A/W. It is possible to increase the photosensitivity value with some alteration, however. Advanced Photonix achieves this by offering a Si quadrant detector optimized for laser guided munitions with a photosensitivity of nearly 0.5 A/W at the desired wavelength [25]. Indium Gallium Arsenide (InGaAs) detectors that offer responsivities on the order of 0.7-0.8 A/W are also available [26]. InGaAs is characterized with higher electron velocity than compared with Si, yielding a higher photosensitivity.

Dark Current

Dark current values are directly proportional to the active area of the device. A larger active area introduces more dark current than a smaller array. To obtain a comparable metric to determine the optimal dark current values it is necessary to divide the dark current of a detector by the active area. This calculation generates values ranging from 0.05 nA/mm^2 to approximately 2 nA/mm^2 for the detectors currently available. The differences among the detectors for this metric are insignificant since the dark current only minimally affects the signal detection capability for this application.

Response Time

Response times (also called rise times) for the detectors currently on the market are extremely fast. Virtually all manufacturers publish response times on the order of 10-15 ns, with some slower detectors having response times of 5-10 μs. Again, because of the higher electron velocity within InGaAs materials, the response times for those detectors are expected to be faster than those made from Si. Nevertheless, the response time values for both detector types are sufficiently fast for the munition application presented in this thesis.

G-Survivability

The sensors employed on the munition will be subjected to a harsh operating environment. Therefore, the focal plane must not only survive through the shock at launch, it must also perform satisfactorily during the high-g flight environment imposed by the dynamics of the flight. Empirical data on typical commercial photodiode arrays used on similar platforms suggest that these sensors are sufficiently resilient for the considered application. Quadrant detectors have demonstrated successful operation with precision guided weapons for quite some time. The ubiquitous AIM-9 Sidewinder, the U.S. Navy's Paveway II missile, and the Army's Advanced Precision Kill Weapon System are just a few of the many systems that have successfully employed photodiode quadrant detector arrays. These weapon systems reach speeds of up to Mach 3 and are launched from various aircraft platforms, including helicopter gunships [27, 28]. Thus, commercial quadrant detectors are presumably robust with respect to g-tolerance for the thesis application.

<u>Aero-thermodynamic Heating</u>

The system designer must also be sure that the aero-thermodynamic heating of the un-cooled focal plane will not expose it to temperatures beyond that of its normal operating range, which is nominally -20° C to 60° C (253 K to 333 K) for the most limited photodiode array. Cooled sensors add unwanted cost and complexity to the design process, along with taking up a larger amount valuable space within the munition itself. Thus, with small munition geometry and a low price ceiling, the designer must be confident that the un-cooled sensor will perform to expectations.

The seeker assembly is typically mounted in the nose cavity of the munition, so the temperature in the nose region must not exceed the proposed limits to ensure proper operation during flight. The dominant temperature fluctuations brought about during flight are a function of the speed of the munition as well as the shape of the nose of the missile. The shape of the designed munition is similar to other missile geometries. The temperature due to aero-thermodynamic heating at the outer surface of the missile nose is calculated using the following expression [29]:

$$T_S = T_a(1 + 0.17M^2) \qquad (3.2.8)$$

where T_S is the surface temperature of the missile nose in Kelvin, T_a is the temperature in Kelvin of the ambient surroundings, and M is the Mach number at which the munition is traveling.

The above equation shows that the surface temperature rise is a function of the speed at which the munition is traveling, and that significant heating can occur at supersonic and hypersonic speeds. However, since this thesis is focusing on speeds of 0.2 M – 0.6 M, the temperature rise due to flight dynamics is acceptably low. The table below lists expected surface temperatures given an ambient temperature of 37.8° C (100° F, 310.8 K).

Speed	Max Acceptable Temp	Surface Temp (T_s)
Mach 0.6		56.8° C
Mach 0.4	$\sim 60\,^{\circ}$ C	46.3° C
Mach 0.2		39.9° C

Table 3.2.6 Expected Surface Temperatures in Operation

This conclusion is further reinforced by the demonstrated success of un-cooled IR photodiode arrays on platforms traveling at speeds ranging from the subsonic to the low-

supersonic regimes. The Sidewinder, along with the Navy's PAVEWAY II, have both successfully implemented un-cooled focal planes [27, 28].

Price

Price is the main discriminator in this analysis, but it is also the most volatile and least documented of all specifications. The wide fluctuation arises for several reasons. Some detectors are optimized for use on demanding platforms, such as laser guided munitions. These detectors must be rigorously tested to ensure their performance regardless of the physical environment. As a result, the testing expenses drive the unit cost higher. To a lesser extent, the price variance is also a consequence of select detectors providing the very best of all possible metrics listed above, others providing a combination of the high end and low end metrics, and some simply containing the low end. Finally, the material used for the sensor face also influences the cost. For example, Silicon arrays are generally cheaper than their InGaAs counterparts. Taken as a whole, the alternatives comprise a broad cost range from approximately $20.00 for a basic detector array to nearly $1400.00 for an optimized quadrant detector.

The descriptions above provide a general overview of quadrant detector performance measurements. It is likely that the future system design will employ a custom designed sensor with performance specifications falling within the range of the individual specifications presented above. However, the goal of this thesis is to create a design utilizing off-the-shelf. For that reason, candidate quadrant photodetectors that meet the requirements of the current mission have been tabulated and outlined in Table 3.2.6.

While photodiode and quadrant detector technology is indeed quite mature, with detectors already utilized in precision guided munitions, there are emerging options undergoing research that may have a role to play in these applications as well. One of these is MEMS micro-bolometer antennas that have the capability to detect infrared radiation [30]. This technology promises to offer very high signal-to-noise ratios while introducing the possibility of low production cost. Although the testing has simply looked at 2-D arrays to this point, there is little doubt that the demonstrated performance success will easily translate to a quadrant detection scheme. With more testing to determine the robustness of the antennas across a broad spectrum

of NIR and IR wavelengths, these MEMS antennas should certainly be considered if they are able to provide the necessary detection characteristics while keeping the fabrication cost low.

Company	Material	Active Area (mm²)	Min λ	Max λ	Peak λ	PS @ 1.06	I_D (nA)	Tmin (°C)	Tmax (°C)	Unit Price
Advanced Photonix	Si	5.4	300	1100	950	0.3	6.5	-40	125	$90.50
Advanced Photonix	Si	17.8	300	1100	950	0.3	27	-40	125	$207.10
Advanced Photonix	Si	38.5	300	1100	1064	0.48	40	-40	125	$1300.00
Melles Griot	Si	100	350	1100	900	0.35	110	N/A	N/A	$775.00
ThorLabs	InGaAs	3.14	900	1700	1550	0.68	5	-40	85	$1386.00
Judson Tech	Ge	100	800	1800	N/A	0.5	N/A	-20	60	N/A
Hamamatsu	Si	16	320	1100	960	0.4	10	-20	60	$23.00
Hamamatsu	Si	81	320	1100	960	0.4	50	-20	60	$58.00

Table 3.2.7 Listing of Available Quadrant Detectors with Performance Specifications

The main goal of this design process is to optimize all parameters for the application for which the detector will be used. The analysis up to this point lays the foundation to conduct an in-depth design trade discussion. However, the inertial guidance provided by the IMU must also be considered to ensure that all integration factors are accounted for prior to finalizing a system. The next subsection will address this area.

3.3 Inertial Sensor Analysis

The ability to create an inexpensive, accurate seeker system hinges upon the IMU cost and performance characteristics. It is the main discriminator of cost and performance. The optical sensor development showed that the differentiation amongst the many focal plane options is not well defined. Commercial IMU's, based on the application, vary in performance and price with great distinction. Therefore, the IMU remains the design factor that will determine the success of this endeavor.

The munition will rely upon the IMU to control its flight path from launch to the control handover to the optical sensor, or approximately 50 seconds of flight time, or less. Directing the flight trajectory for more than 80% of the time, the IMU's performance is of extreme importance to achieving a successful impact. Thus, the IMU must be capable of placing the munition within a so-called "acquisition basket", the spatial region within which the focal plane's FOV contains

the target signature. The following paragraphs will outline the design process necessary to meet this stringent performance requirement.

3.3.1 Requirements

The mission requirements dictate the necessary component performance of the IMU. The IMU will have control for the majority of the expected trajectory, with the munition traveling approximately 4-8 km under its guidance. Assuming the coordinates of the launch position are known *a priori*, the IMU must place the munition in the correct location, with an adequate orientation, to ensure that the target signature remains within the seeker's FOV. With a dependence upon the defined FOV of the focal plane, the paramount requirement is that the aggregate of the angular drift, caused by the bias instability and random walk of the IMU, must not allow longitudinal axis of the munition to deviate beyond 15° from the estimated target location. This would render the focal plane unable to locate the target signature and cause mission failure. Placing the munition within this region allows the seeker focal plane to locate the target and eventually guide the munition to an accurate impact.

3.3.2 Allowable Drift Calculations

Analyzing the total allowable drift for an all-IMU guidance system will aid in this analysis by establishing a baseline for comparison with a seeker-aided system with a 30° FOV. Similar analyses can be undertaken both systems. With this FOV, the seeker-aided munition's longitudinal axis is allowed to deviate 15° from the target before the target is wholly out of the seeker's sight. The all-IMU system, on the other hand, is only allowed to drift a perpendicular distance of 1.5 m from the original (correct) course heading. This stringent requirement equates to a much smaller angular deviation allowance. The following paragraphs develop the investigations in further detail.

For both analyses, one must account for the accumulation of the error as the IMU propagates it along the flight path. Assuming that the error manifests itself consistently for the duration of the flight, the IMU will deviate both in local and global spatial orientation. "Local"

refers the body axes of the munition and "global" denotes the earth fixed domain containing both the munition and target.

For both situations, the author assumes the worst case scenario that the error propagates in a single direction, away from the correct course heading. The drift analysis takes place within a two-dimensional subspace, with the designer spying the trajectory of the munition from above to evaluate the flight in x- and y-space. For the seeker aided analysis, the author defines two pertinent angular quantities. The first is ε, a measure of the angular deviation from the original heading in the local coordinate frame of the munition. The second, η, is a measure of the angular deviation in the global coordinate subspace due to spatial error caused by the IMU drift. As figure 3.3.1 depicts, the summation of ε and η must be less than 15° in order to ensure that the target is within the focal plane's FOV.
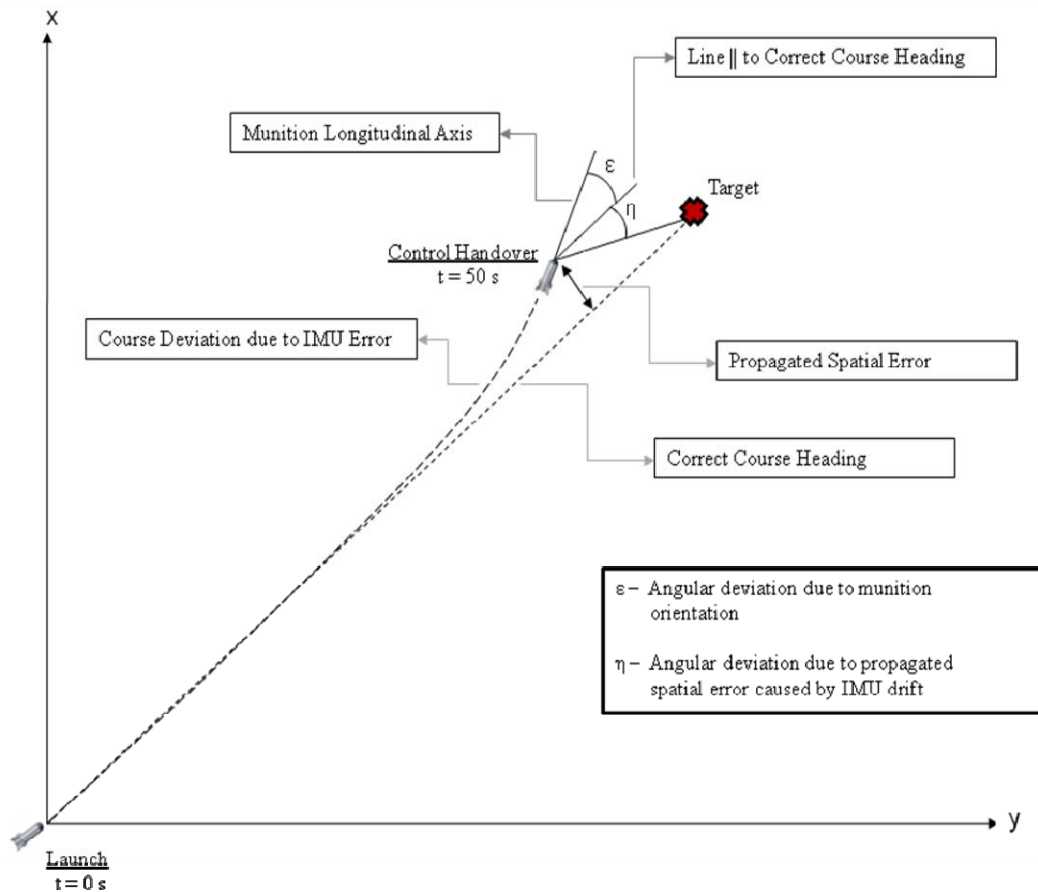
Figure 3.3.1 Allowable Drift Scenario Depiction

To determine the drift allowances for the seeker aided and all-IMU systems, the author developed a Matlab script (listing available in Appendix A). Note that only the first 38 lines of coding in the script are necessary for the all-IMU model. The remaining code exists to compute the maximum allowable IMU drift while simultaneously optimizing the relationship between the two angles (ε & η), keeping their sum below a value of 15°. The max drift calculation is developed by the following equation, which outlines an approximate formula for the spatial error propagated by the IMU drift:

$$d = \sum_{i=0}^{n} V \sin(e \cdot t_i) \qquad (3.3.1)$$

where V is the velocity at which the munition is traveling in m/s, e is the IMU drift in rad/s, and t_i designates the flight time of the munition. The summation of the equation indicates that the error accumulates over the duration of the munition's flight trajectory, where $t_0 = 0$ s, and t_n is the time at impact.

In the seeker-aided model, the control handover takes place 10 s prior to t_n, at which point the seeker head governs the flight trajectory to final impact. Subsequently, η is calculated according to a simple geometrical calculation:

$$\eta = \tan^{-1}(d / d_{go}) \qquad (3.3.2)$$

where d_{go} is the distance-to-go to hit the target along the line parallel to the correct flight path. By the same token, ε is simply calculated as:

$$\varepsilon = e \cdot t_n \qquad (3.3.3)$$

because the local angular deviation is merely the IMU drift value multiplied by the time in flight.

The author ran the model to produce results for munition speeds of Mach 0.2, Mach 0.4, and Mach 0.6 approaching target distances of 5 km, 7.5 km, and 10 km. Table 3.3.1 outlines the meaningful results of the seeker aided analysis that produces max drift allowances to keep the sum of ε and η below 15°. Table 3.3.2 provides a side-by-side comparison of the seeker aided vs. all-IMU system.

Table 3.3.2 shows that an all-IMU system indeed demands ultra-accurate devices to retain an acceptable CEP value. Although the market trends for MEMS IMU's suggest that such accurate devices will eventually become available at reasonable prices, the current prices for

units with that type of accuracy would significantly exceed the $15,000 cost ceiling imposed on the entire seeker system by the requirements of the design.

Speed	Target Distance	Allowable IMU Drift for 15° HE	d_{go} @ handover	d @ handover	η @ handover	ε @ handover
M = 0.2	5 km	193.2°/hr	648 m	132.5 m	11.56°	3.44°
	7.5 km	83.5°/hr	632 m	141.8 m	12.65°	2.35°
	10 km	45.8°/hr	616 m	144.9 m	13.24°	1.76°
M = 0.4	5 km	826.2°/hr	1328 m	205.7 m	8.8°	6.2°
	7.5 km	331.8°/hr	1244 m	236.4 m	10.76°	4.24°
	10 km	193.3°/hr	1296 m	265.1 m	11.56°	3.44°
M = 0.6	5 km	1915.1°/hr	1880 m	231.4 m	7.02°	7.98°
	7.5 km	790.1°/hr	1884 m	300.9 m	9.07°	5.93°
	10 km	435.6°/hr	1888 m	342.4 m	10.28°	4.72°

Table 3.3.1 Drift Allowance Analysis Results for a **15° HE** at Control Handover

Speed	Target Distance	All-IMU System	Seeker Aided System
M = 0.2	5 km	1.64°/hr	193.2°/hr
	7.5 km	0.73°/hr	83.5°/hr
	10 km	0.42°/hr	45.8°/hr
M = 0.4	5 km	3.24°/hr	826.2°/hr
	7.5 km	1.43°/hr	331.8°/hr
	10 km	0.82°/hr	193.2°/hr
M = 0.6	5 km	4.58°/hr	1915.1°/hr
	7.5 km	2.12°/hr	790.1°/hr
	10 km	1.21°/hr	435.6°/hr

Table 3.3.2 Comparison of Allowable Drift Values for 1.5 m CEP

The analysis above demonstrates the utility of the addition of a terminal guidance seeker by greatly relaxing the requirements imposed upon the IMU performance. Looking at the mission constraints of a munition impacting a target at a range of 5-10 km, the allowable drift value climbs significantly at each modeling speed and target distance. In fact, for every engagement situation the seeker-aided drift requirement is more than 100 times that of an all-IMU system. This performance difference undoubtedly translates into huge cost savings.

The most demanding IMU drift value of 45.8°/hr exists at a munition speed of Mach 0.2 engaging a target 10 km away. While it is beneficial to include the model results for that situation, it is likely that it will never be realized as a faster moving munition will be used for a longer range target. A munition moving Mach 0.2 will likely only be used to engage a target at 5 km or less. As such, the requirement for IMU accuracy is likely more relaxed than the 45.8°/hr for a 10 km target or even the 83.5°/hr for a 7.5 km target. Certainly, the design engineer will desire to include some sort of a "factor of safety" in the system fabrication, so for the present analysis the author will set the maximum allowable drift at a value of 100°/hr. Even with the added safety factor, the addition of the seeker allows the designer to find a MEMS IMU that is both commercially available and able to meet the price ceiling set forth by the mission constraints.

The author reiterates that the analysis conducted in this subsection is a very pessimistic formulation. It does not model drift as a random process, but instead in a deterministic manner with a constant drift rate biased to one side throughout. Should a system designer wish to model the IMU drift less conservatively, Matlab will support the random drift simulation quite nicely.

3.3.3 Technology Survey

Figure 2.2.6 is a plot containing a recent depiction (2001) of the state of the IMU industry. Those IMU's that carry the smallest error (lower left region) also carry the most extreme cost and size. MEMS IMU's, comprising the majority of the upper right region of the figure are relatively cheap, but also bear accuracy issues. MEMS IMU development, however, is rapidly improving performance while keeping costs down. This section takes a close look at the expected trends with respect to MEMS IMU price and performance and brings to light the types of devices currently available that meet both the price and accuracy requirements of the thesis mission.

As with the optical sensor devices, there are many companies that produce MEMS IMU's for the application under consideration. However, unlike the optical sensors, there is significant variation among both the performance and the cost characteristics of MEMS IMU's commercially available. The tradeoff between cost and performance (as well as size/weight & performance) must be optimized to achieve a system design that will perform up to the mission requirements while minimizing the cost to the end user. While section 2.2.2 presented the

performance parameters of MEM's IMU's that was purely descriptive, the subsequent paragraphs will provide the reader a brief qualitative synopsis comparing these state-of-the-art MEMS IMU performance characteristics.

Bias Instability

Depending on the design application, a survey of available IMU's shows that bias instabilities spread quite a broad range. In general, the accelerometer bias characteristic is somewhat inconsequential, as the gyro angular rate bias shows a more profound volatility. The candidate IMU's for the thesis study publish gyro rate biases from a miniscule 1°/hr to nearly 20000°/hr. The majority, however, fall within the specified constraints imposed by the analysis of section 3.2.2.

Angular Random Walk

As a secondary factor in the performance classification of IMU's the angular random walk (ARW) characteristics encountered within the survey proved to be satisfactory. Most of the surveyed IMU's offer ARW values of less than 2.5°/rt-hr, with one outlier at a substandard 60°/rt-hr. Save for the IMU with 60°/rt-hr, the random walk performance characteristics published are well suited to provide the type of performance necessary to attain a successful design.

Scale Factor Accuracy

A tertiary concern in the measurement of an IMU's performance level, scale factor accuracies of the vast majority of the surveyed devices are acceptable. These values ranged from 150 ppm to 20000 ppm. The high values for scale factor error arise in the lower grade IMU's. These lower quality devices are more sensitive to changes in the operating environment and ambient temperature, causing the degradation of scale factor accuracy.

Dynamic Range

Nearly all specified measurement ranges encountered in the survey prove to be satisfactory. The scope of the mission considered in this thesis does not call for highly dynamic maneuvers and thus will not require an extensive range of measurement. Dynamic range values for the lower

quality IMU's stands around 100°/s while the more robust units offer measurement ranges of up to 1500°/s. Measurement resolution may prove to be a troubling issue for those IMU's with higher dynamic ranges. This matter will be addressed when the candidate systems are formed.

G-Survivability

While the operational environment of the munition is demanding, the expected loads placed upon the munition during flight are not extremely harsh. Many of the surveyed IMU's have g-measurement ranges well beyond those it is expected to encounter during flight. Nevertheless, several IMU's on the market have been high-g tested and are able to withstand upwards of 20K g's, a consideration that is paramount if the mission of the designed munition is to be expanded upon down the road. For the present analysis, however, it will suffice to point out that the IMU's currently on the market have demonstrated success on munitions that operate in more severe environments. Thus, they can be expected to perform suitably within the defined mission scenario.

Aero-Thermodynamic Heating

The majority of the surveyed IMU's had specified temperature ranges of approximately -55° C to 85° C. As was the conclusion of the analysis of aero-thermodynamic heating of the IR focal plane according to equation 3.2.8, the ambient temperature affecting the IMU will not deviate outside this acceptable operating range. Therefore, it is reasonable to expect that the published performance characteristics will not be overtly affected by the ambient temperature.

Price

Device cost is a very important driver in the design process. Several IMU manufacturers are well established in the defense community and have the capability offer high performance MEMS units at low cost. Others are still emerging in the MEMS area and have yet to develop their technology to that point. Thus, the prices of the surveyed components vary significantly, from nearly $2,000 to $30,000. However, the reader should note that these cost estimates are single unit prices, and all values will be significantly lower in production level quantities.

The descriptive paragraphs above give the reader general insight into the performance trends of the IMU's currently available on the commercial market. As with the optical sensors,

the selected system will fall within the operating range of the performance specification listed in the brief synopsis. However, unlike the IR focal planes, commercial IMU's are very divergent with respect to performance. Nearly every one of the pertinent performance measurement parameters vary greatly from unit to unit. For this reason, the author generated a concise listing of IMU systems that is helpful for the design process of the proposed seeker system.

It is important to note that the performance characteristics and costs of IMU's are continually changing. The table below attempts to outline the current state of the industry. However, it is by no means comprehensive; and with the trends of the industry moving towards higher performance with lower costs, it is likely that the values will change for the better in the very near future.

System	Volume (in^3)	Mass (lbs)	Approx Cost (K\$)	Gyro Bias (°/hr) 1σ	Accel Bias (milli-g) 1σ	Remarks
Honeywell HG1930	4	0.35	3.5	20	4	High G tested
Honeywell HG1700AG	33	1.6	N/A	1	1	RLG
AIS SiIMU02	7.3	0.463	4.5	6.5	0.5	High G tested - Silicon Sensing
AIS SiIMU04	10.35	0.5512	4.5	8	3	Marketed by Silicon Sensing
Xbow IMU440CA	28.125	1.3	2	7200	15	MEMS design
Xbow IMU700CB	120	3.5	11.5	20	12	FOG, Si Accelerometers
MEMSense μIMU	5.53	0.0294	2.5	2016	2.1	
Systron Donner MMQ50	9	0.5	5	50-200	2.5	Single unit price
Xsens Mti	4.52	0.1102	3	18000	2.04	
Litton LN200	32	1.54	30	10	1000	FOG, MEMS Si Accelerometers
Draper MMIMU	8	0.62	30	10	3000	MEMS, non-production design
Micro-Aero MASIMU01	7.7	0.1764	4	60	n/a	Utilizes Analog Devices Gyros

Table 3.3.3 Listing of Available IMU's with Performance Specifications

The table outlines an abbreviated record of the important parameters surrounding the design process. For a complete listing of all performance characteristics, see the table in Appendix B.

As there is generally a great deal of product specification information available on MEMS IMU devices, as outlined in the table above, the designer will seek to narrow the design choices in some fashion. One method that is useful for this type of analysis is to plot the most vital performance parameters on a single plot and determine visually which options will optimize each of the individual areas. The author plotted the volume, cost, and gyro bias characteristics of each of the IMU's listed by Table 3.3.3 to attempt to determine the options prove to be best suited to move forward with in the design process. Figure 3.3.2 plots the three performance characteristics in a three-dimensional setting.
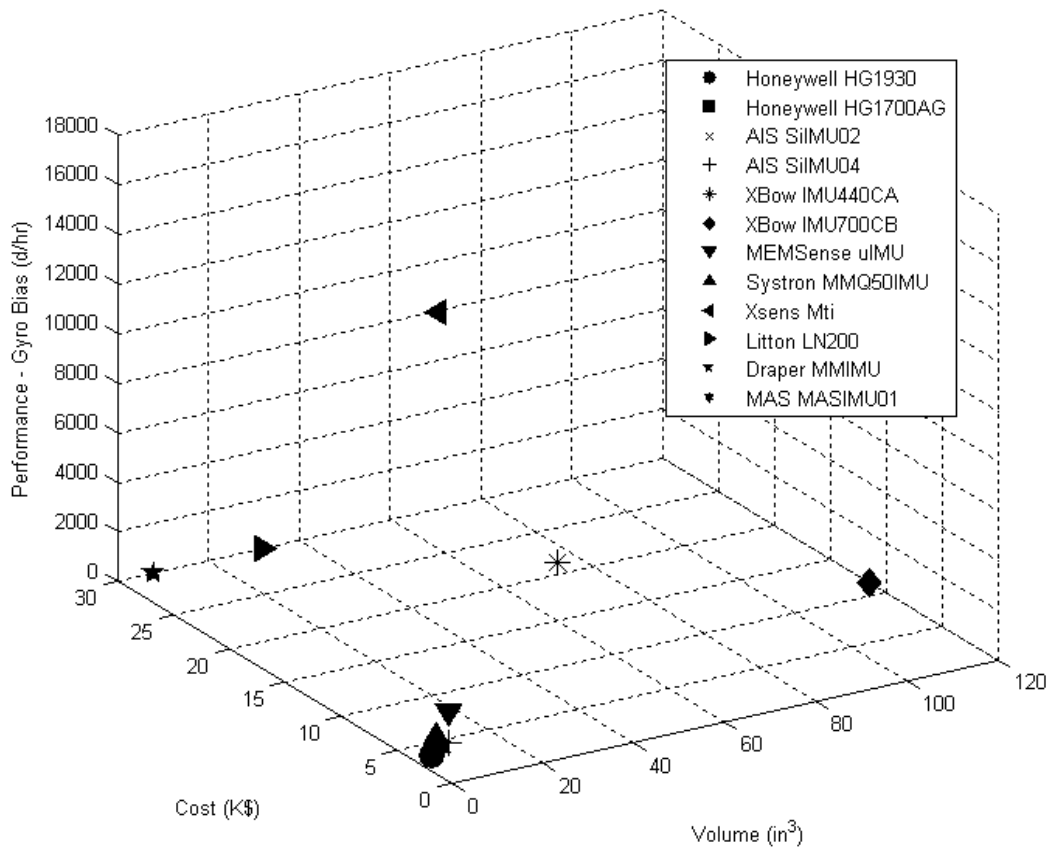
Figure 3.3.2 IMU Trade-Off Parameters Depicted in a 3-D Setting

The plot clearly shows the distinct spread of the vital selection criteria. Because of the large differences, the designer seeks to move forward with a narrowed selection of IMU's to place in candidate seeker system designs. Only those IMU's in the near the origin on all three axes are able to meet the requirement, so only these will be considered from this point forward. Figure 3.3.3 illustrates a closer look at the five IMU's to be considered beyond this point in the analysis.

Each of the remaining IMU's is priced such that such that there is plenty of latitude remaining with which to design the rest of the system while still meeting (or exceeding) the requirements for total a system cost of $15,000. Additionally, each of the IMU's are small enough in size to fit within a projectile with a maximum diameter of 4". The Honeywell, Micro-Aerospace Solutions, and AIS IMU options are completely satisfactory with respect to the accuracy requirement. The Systron Donner IMU doesn't allow for a large safety factor with respect to gyro bias stability, but should be considered as a result of its other attractive features.
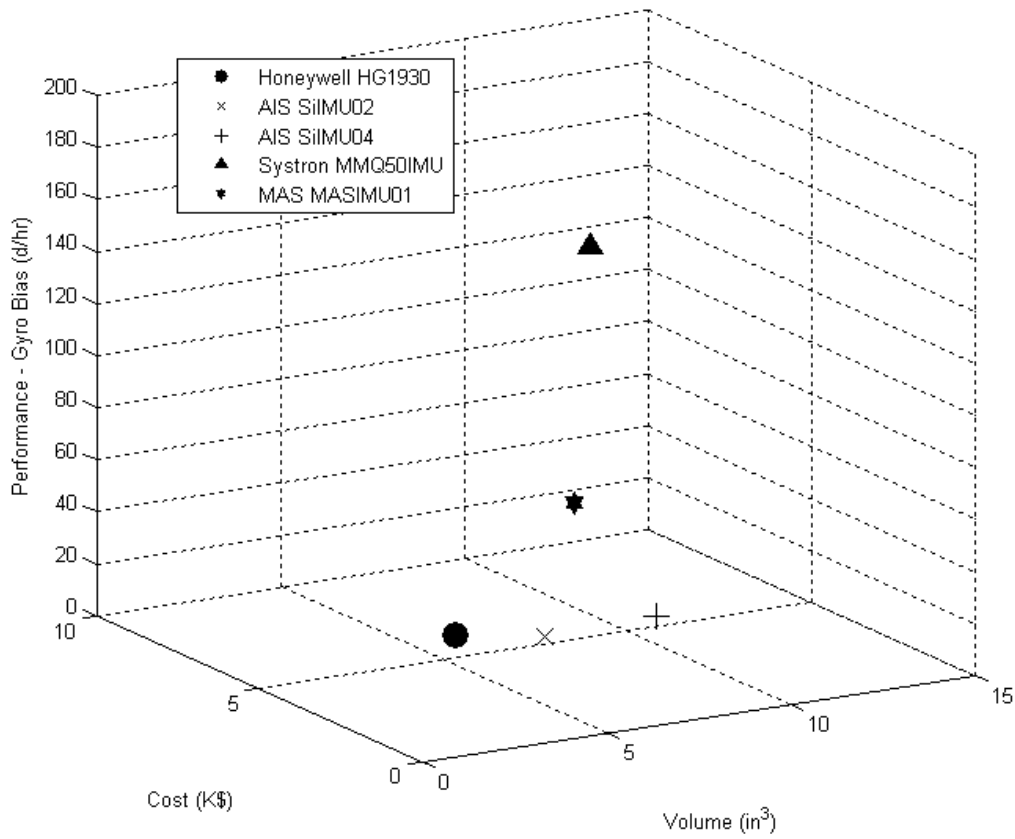
Figure 3.3.3 Final Five IMU Candidates

Finally, to provide a basis for comparison for later models, the author obtained miss distance estimates for an all-IMU system containing each of the final five IMU candidates. Outlining these expected miss values for each of the candidates allows a designer to quantify the benefit of adding a terminal guidance seeker in later analyses. The expected miss values for each of the five IMU's are displayed in tables 3.3.4-3.3.6.

Option	All IMU Miss - 5 km Tgt (m)	All IMU Miss - 7.5 km Tgt (m)	All IMU Miss - 10 km Tgt (m)
Honeywell HG1930	18.44	41.31	73.28
AIS SiIMU02	5.92	13.28	23.55
AIS SiIMU04	7.25	16.23	28.79
Systron Donner MMQ50	137.30	307.46	545.15
Micro-Aero MASIMU01	55.00	123.19	218.50

Table 3.3.4 All-IMU System Miss Distances – Mach 0.2

Option	All IMU Miss - 5 km Tgt (m)	All IMU Miss - 7.5 km Tgt (m)	All IMU Miss - 10 km Tgt (m)
Honeywell HG1930	9.34	21.21	36.89
AIS SiIMU02	3.00	6.82	11.86
AIS SiIMU04	3.67	8.33	14.49
Systron Donner MMQ50	69.58	157.95	274.61
Micro-Aero MASIMU01	27.87	63.26	110.00

Table 3.3.5 All-IMU System Miss Distances – Mach 0.4

Option	All IMU Miss - 5 km Tgt (m)	All IMU Miss - 7.5 km Tgt (m)	All IMU Miss - 10 km Tgt (m)
Honeywell HG1930	6.61	14.29	24.90
AIS SiIMU02	2.12	4.59	8.00
AIS SiIMU04	2.60	5.61	9.78
Systron Donner MMQ50	49.20	106.41	185.42
Micro-Aero MASIMU01	19.70	42.62	72.27

Table 3.3.6 All-IMU System Miss Distances – Mach 0.6

A traditional IMU will certainly provide the angular measurement capability to satisfy the demands of seeker-aided guidance for the mission considered by this thesis. In fact, with the IMU-controlled flight time expected to be relatively short, the IMU is perhaps over-designed for the application. Just as there exist alternatives to the photodiode arrays detecting the designation signal, there are also simpler, non-IMU, options that could potentially be considered for the initial guidance of the projectile. An option that may warrant consideration as a replacement for the IMU in such tactical situations is a simple rate sensor. This type of device consists of multiple gyros aligned along two (or more) axes to provide angular rate information for the platform it is supporting (i.e. no accelerometers). The advantage of this type of system is that it allows for much smaller packaging and significantly reduced costs over an IMU with the same gyro accuracy. Systron Donner sells the Quartz Dual Axis Rate Sensor (Figure 3.3.4), whose design application relates very well to the thesis scenario [31]. One can see from the figure that the unit size makes this option very desirable when space within a munition housing is at a premium. While a rate sensor may not be beneficial in all situations, it certainly warrants further research to determine if it is effective in scenarios similar to that considered by this thesis.
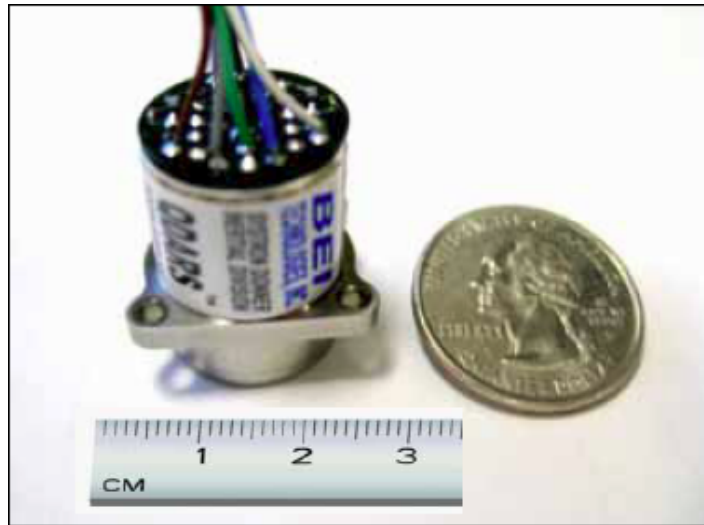
Figure 3.3.4 Systron Donner Quartz Dual Axis Rate Sensor (QDARS)

The IMU analysis conducted above adds to the foundation from which to conduct component trade studies to achieve the optimal seeker design. With the optical sensor and IMU analyses complete, there remains just the projectile modeling analysis element to address. The next section will take the reader through this specific portion of the study. After dealing with the projectile dynamics issues, the designer is able to more deeply develop the total system design trade-offs.

3.4 Projectile Modeling

The final subsection in the analysis and modeling chapter will focus on the flight dynamics of the projectile. Because the mission specifies that the ordnance will be employed in an urban environment, the designer must be certain that the projectile retain adequate maneuverability to sustain stable flight in areas densely packed with structures. As such, the goal of this section is to determine a generic projectile design (with dimensions that can be extrapolated to be compared with tactical munitions currently used by the military) and model it to determine its corresponding flight dynamics. In this manner, the author can prove that the projectile (and those similar to it) will satisfy the demands of the situations for which it will be used.

3.4.1 Projectile Design Rationale & Dimensions

The first step in the process of modeling the projectile is to formulate its geometrical design. This thesis aims to create a generic scenario that will relate to the myriad of projects being considered for precision guidance in todays military. There are several projects currently underway that would benefit from a cheap, reliable seeker system, such as the system this thesis proposes. Two of these are the Air Force's Destructible Expendable (DEX) projectile program and the Army's Precision Guided Mortar Munition (PGMM) program [4, 5]. Each of these investigations is seeking to add precision guidance to tactical strike packages. DEX is attempting to employ actively controlled rocket powered missiles to replace the passive aircraft self-protection measures currently in use, while PGMM looks to add terminal guidance to the Army's mortar platforms. The defined requirements of a projectile diameter of 4" or less and a maximum weight of 50 lb satisfy the constraints of the aforementioned scenarios perfectly.

Keeping these applications in mind, the author designed a projectile of general dimensions, allowing the specific scenario analyzed in this thesis to be easily related to the investigations presently in progress. The missile body is an axisymmetric cylinder with a hemi-spherical nose and a boat-tailed aft section. Figures 3.4.1 and 3.4.2 outline the missile design and dimensions that will be input into a projectile modeling software program to complete the necessary analyses for this section of the thesis.

The low nose fineness ratio (defined as the length of the nose divided by its diameter) created by the domed nose reduces seeker dome error by providing a geometry that limits the bending (refraction) of the incoming EM waves the seeker is tracking [32]. A high nose fineness is does the opposite but is ideal for supersonic travel because of low drag characteristics. Low nose fineness is preferred for this design because the projectile is expected to travel at speeds in the subsonic and transonic regimes. The boat-tail aft portion is also ideal for subsonic travel as it significantly reduces base airframe drag at lower speeds [32]. The projectile has four symmetrically located fins to provide for the control of the missile. The four aerodynamic control surfaces maintain integrated control of the pitch, yaw, and roll axes for the projectile.
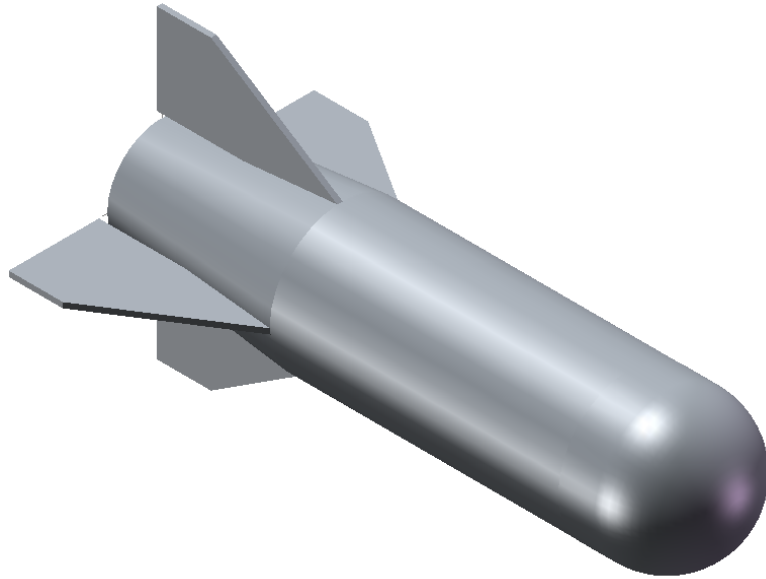
Figure 3.4.1 Isometric View of the Modeled Projectile
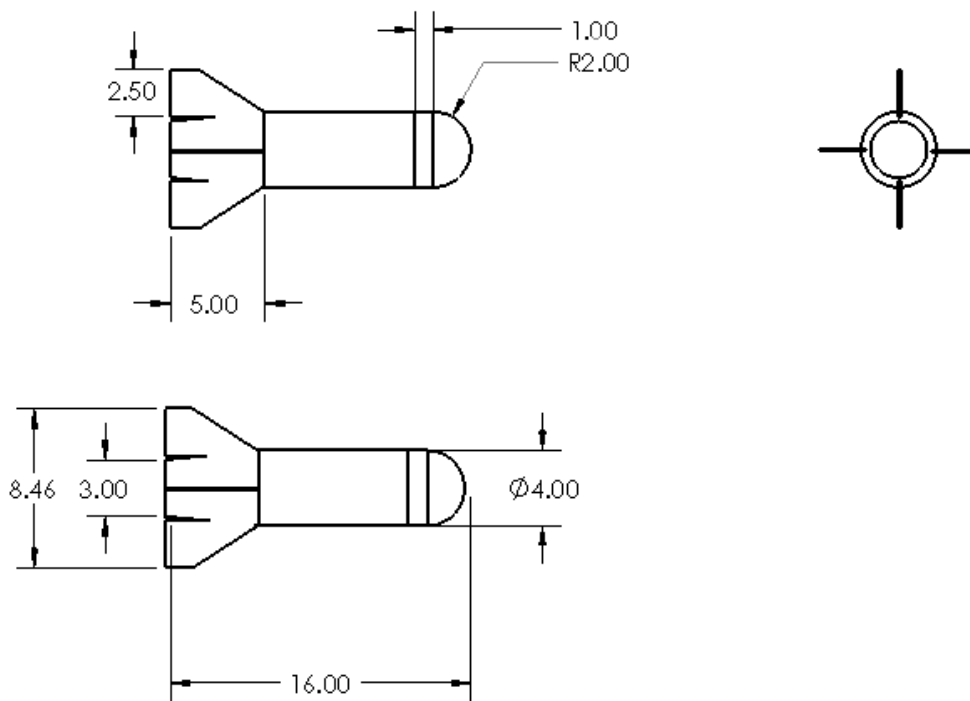
Figure 3.4.2 Standard Three View Drawing of Projectile with Dimensions (in)

3.4.2 Overview of Missile DATCOM

The U.S. Air Force has long had great interest in the projectile modeling. For that reason, engineers of the Air Force Research Laboratory (AFRL) have developed Missile DATCOM, a stand-alone projectile modeling program to address this need. Missile DATCOM is an engineering level computer program designed calculate aerodynamic forces, moments, stability derivatives, and control characteristics as a function of angle of attack and Mach number for a variety of missile arrangements [33]. It is widely used in the aerospace community and has been in continuous development since the late 1980's. Ongoing updates to the code have addressed slight flaws, and AFRL engineers continue to make the program more robust by updating the code based on new empirical data comparisons with simulated outputs from Missile DATCOM.

The program applies a component build up method, calculating output characteristics for the fins and body separately, and then summing the two to obtain overall force and moment coefficients [34]. The input missile parameters are missile size and shape, angles of attack, speed, as well as geometries of fin sets and/or other protuberances that may be present on the missile's exterior surface. Missile DATCOM will uses these inputs to produce coefficients of normal force, axial force, pitching moment, as well as lift and drag characteristics.

3.4.3 Demonstration of Basic Dynamic Capability

This subsection begins with the Missile DATCOM modeling of the designed projectile in order to determine its fundamental aerodynamic attributes. DATCOM's calculation of aerodynamic coefficients yields basic level insight into the expected stability and turning performance of the munition in flight. The author discusses these performance parameters and how they relate to the governing aerodynamic equations on a very basic level to lay the foundation for more involved and complex analysis to take place in later subsections with the construction of a dynamic projectile model. The goal of the final model is use these governing equations of motion to simulate and predict the actual in-flight performance of the designed munition to determine expected target miss distances.

The munition design was input into Missile DATCOM with the assumption that the Reynolds number of the surrounding air flow is 3×10^6, signifying transitional boundary layer flow typical of all winged airframes. The munition was again modeled at speeds of Mach 0.2,

Mach 0.4, and Mach 0.6. Finally, all aerodynamic outputs were measured at angles of attack ranging from -28° to +28° at 4° intervals. In this manner, the author can determine the basic stability and turning capability characteristics over a significantly large range of heading variation.   These parameters were input into Missile DATCOM (refer to Appendix C for example input code), producing the desired output characteristics. Tables 3.4.1-3.4.3 summarize the pertinent output parameters.   Note that α is the angle of attack in degrees, C_N is the coefficient of normal force, C_M is the pitching moment coefficient, C_A is the axial force coefficient, and C_L and C_D signify the coefficients of lift and drag, respectively.

α	C_N	C_M	C_A	C_L	C_D
-28	-2.4765	0.3832	0.1234	-2.1287	1.2716
-24	-2.3759	0.6505	0.1389	-2.1140	1.0932
-20	-2.1842	0.8126	0.1542	-1.9997	0.8919
-16	-1.8883	0.8436	0.1679	-1.7689	0.6819
-12	-1.4973	0.7496	0.1788	-1.4274	0.4862
-8	-1.0078	0.5193	0.1863	-0.9721	0.3247
-4	-0.4886	0.2436	0.1903	-0.4741	0.2239
0	0.0000	0.0000	0.1912	0.0000	0.1912
4	0.4886	-0.2436	0.1903	0.4741	0.2239
8	1.0078	-0.5193	0.1863	0.9721	0.3247
12	1.4973	-0.7496	0.1788	1.4274	0.4862
16	1.8883	-0.8436	0.1679	1.7689	0.6819
20	2.1842	-0.8126	0.1542	1.9997	0.8919
24	2.3759	-0.6505	0.1389	2.1140	1.0932
28	2.4765	-0.3832	0.1234	2.1287	1.2716

Table 3.4.1 Output Parameters for Mach 0.2

α	C_N	C_M	C_A	C_L	C_D
-28	-2.5000	0.3796	0.1215	-2.1503	1.2810
-24	-2.3594	0.6073	0.1385	-2.0991	1.0862
-20	-2.1759	0.7941	0.1550	-1.9917	0.8898
-16	-1.8923	0.8507	0.1695	-1.7723	0.6845
-12	-1.5083	0.7702	0.1810	-1.4377	0.4906
-8	-1.0196	0.5410	0.1888	-0.9835	0.3288
-4	-0.4951	0.2555	0.1929	-0.4804	0.2269
0	0.0000	0.0000	0.1938	0.0000	0.1938
4	0.4951	-0.2555	0.1929	0.4804	0.2269
8	1.0196	-0.5410	0.1888	0.9835	0.3288
12	1.5083	-0.7702	0.1810	1.4377	0.4906
16	1.8923	-0.8507	0.1695	1.7723	0.6845
20	2.1759	-0.7941	0.1550	1.9917	0.8898
24	2.3594	-0.6073	0.1385	2.0991	1.0862
28	2.5000	-0.3796	0.1215	2.1503	1.2810

Table 3.4.2 Output Parameters for Mach 0.4

α	C_N	C_M	C_A	C_L	C_D
-28	-2.5679	0.3800	0.1174	-2.2122	1.3092
-24	-2.3392	0.5320	0.1385	-2.0806	1.0780
-20	-2.1326	0.7205	0.1580	-1.9500	0.8779
-16	-1.8849	0.8394	0.1739	-1.7639	0.6868
-12	-1.5222	0.7934	0.1863	-1.4502	0.4987
-8	-1.0380	0.5708	0.1946	-1.0008	0.3372
-4	-0.5063	0.2735	0.1990	-0.4912	0.2338
0	0.0000	0.0000	0.2000	0.0000	0.2000
4	0.5063	-0.2735	0.1990	0.4912	0.2338
8	1.0380	-0.5708	0.1946	1.0008	0.3372
12	1.5222	-0.7934	0.1863	1.4502	0.4987
16	1.8849	-0.8394	0.1739	1.7639	0.6868
20	2.1326	-0.7205	0.1580	1.9500	0.8779
24	2.3392	-0.5320	0.1385	2.0806	1.0780
28	2.5679	-0.3800	0.1174	2.2122	1.3092

Table 3.4.3 Output Parameters for Mach 0.6

The first aerodynamic attribute of primary concern is stability. The missile must be stable over the range of course corrections expected from the munition's guidance system to ensure successful operation. If airframe stability is not present over the minimum range of ±15° dictated by the sensor's FOV, the missile may be lost due to the lack of sufficient control necessary to make the required course correction. The output parameters from Missile DATCOM allow for the calculation of the stability range of the designed projectile.

Missile and aircraft stability are heavily dependent upon the pitching moment acting upon the aircraft during flight. The pitching moment refers to the moment created about the airframe center of gravity (c.g.) due to the distribution of forces along its length [35]. This moment tends to rotate the nose either up or down, with a positive moment defined as one that will push the nose up, in most cases (because this thesis considers an axi-symmetric projectile, the moment to the left or right, the yawing moment will relate closely to the pitching moment, although affected by gravity slightly differently than the true pitching moment).

An airframe is said to be "stable" if it tends to return to its equilibrium state when disturbed [35]. The entity that will cause the return to equilibrium, or the so-called "trim condition", is the pitching moment, given by:

$$M = \frac{1}{2}\rho v^2 S_{ref} c C_M \qquad (3.4.1)$$

where ρ is the ambient air density, v is the velocity of the munition, S is the reference area of the lift producing devices (fins and body), c is the airfoil (fin) chord length, and C_M is the pitching moment coefficient. The two factors in equation 3.4.1 that are not inherently constant for all angles of attack are v and C_M, and because the munition is expected to maintain a fairly constant velocity over the course of its 60 second flight interval, the pitching moment coefficient is the one true factor that will be altered as the ordnance changes its flight path. Thus, with all other factors remaining constant, the stability of an airframe is most heavily dependent upon the pitching moment coefficient, as it is the only variable in equation 3.4.1. Before demonstrating the results of the analysis, however, it is desirable that the particulars of airframe stability be developed in more detail.

If a missile is traveling in trim condition and a disturbance causes the nose to pitch downward to a negative angle of attack, the missile must create a positive moment to return to a

stable condition. Likewise, if the nose pitches upwards (positive angle of attack), the munition requires a negative pitching moment to return to the stable trim condition. Consequently, because the moment itself varies directly with the pitching moment coefficient, these two cases would require positive and negative C_M's, respectively, for stability. Furthermore, a more negative or positive change in the angle of attack will correspondingly require a greater change in the moment coefficient. In sum, this explanation simplifies into the statement that the slope of the plot of C_M vs. α ($C_{M\alpha}$) should always be negative for airframe stability [36].

The missile design utilized by the author was subjected to this test based on Missile DATCOM's output of pitching moment coefficient for each of the three mach numbers considered. Figure 3.4.3 outlines the results of this analysis.
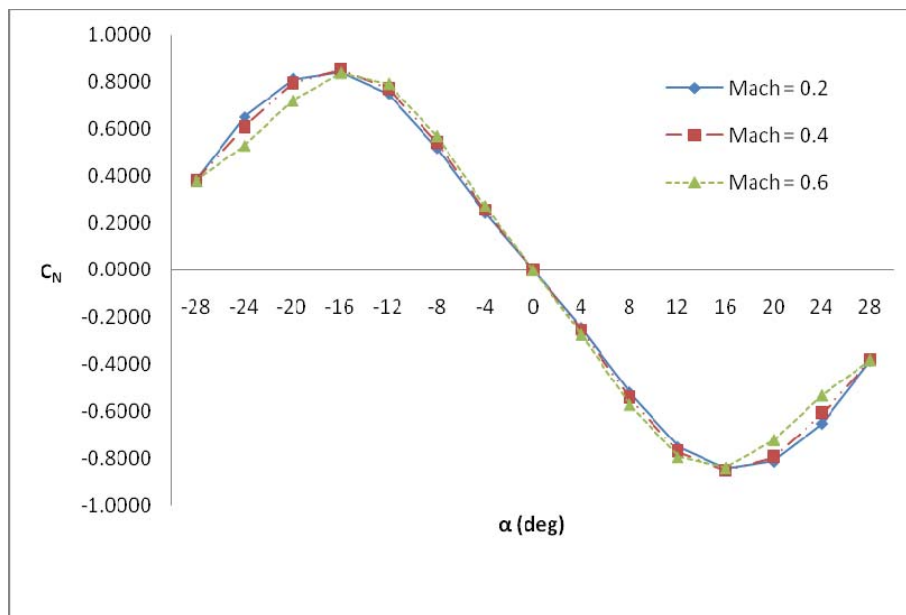
Figure 3.4.3 Pitching Moment vs Angle of Attack

The results show that over the range from -16° to 16° the basic missile design maintains a negative slope, indicating stability. The addition of a control system to provide actuation for the fins will allow the projectile to remain within this stable window in the event the angle of attack becomes too large to retain stability. In this manner, the control system will ensure that the munition does not deviate from its stable range and become lost as it attempts to drive the heading error to zero. After executing a maneuver, the munition will eventually settle back down to its trim condition in a finite amount of time. This "settling time" becomes paramount in

the time constrained engagement situation. As such, the designer should model and determine this time value to ensure that it does not exceed the time allowed by the scenario. Before discussing this issue at length in the following subsections, the author will address the other aerodynamic concern on a primary level.

The next characteristic of concern is turning capability. The drift present within the IMU will undoubtedly cause the sensor's line of sight to point somewhere other than directly at the target. Provided that the target is still within the sensor's FOV when the control hand-off is made, the quadrant detector will supply the necessary control input signals to be processed by the guidance system. The processed signals will then prompt control flap deflections to change the heading to the point that the munition is oriented in-line with the laser designation signal reflecting from the target.

The outputs of Missile DATCOM allow for a basic calculation of approximate turning capability as well. Note that the following calculations are highly simplified and are meant only to produce a broad prediction of whether or not the dynamic turn capability of the designed projectile will be satisfactory. Performing the simplified analysis prior to developing an involved model allows the system designer to identify an insufficient area before becoming too deeply entrenched in the design process. A more involved approach is undertaken in a later subsection.

Generally, turn performance is defined in terms of an acceleration load factor, a measure of the acceleration normal to the missile body in g's, where 1 "g" is the acceleration due to gravity (9.81 m/s^2). The load factor can be thought of as analogous to centripetal acceleration exerted on a body during a turn. The calculation of the load factor of any airframe is ultimately determined from the normal force incident upon the projectile during a turn [35]. The normal force is calculated according to:

$$N = \frac{1}{2}\rho v^2 S C_N \tag{3.4.2}$$

where C_N denotes the coefficient of normal force computed by Missile DATCOM and all other factors are identical to those in Equation 3.4.1. It should be noted here that because of the symmetry of the modeled projectile, the C_N calculated for the different pitching angles will be used to calculate the normal force. Although a change in the pitching angle of the projectile will

not cause a turn, this transition is possible because the coefficient of normal force will be the same for an identical change about either of the pitch or yaw axes.

To determine the load factor, the only remaining necessity is to know the mass of the munition itself. The mass, m, of the projectile can estimated without difficulty knowing the volume of the munition and the materials that will make up the components. Given the normal force on the projectile and its mass, the load factor is computed as [37]:

$$n = \frac{N}{m} \tag{3.4.3}$$

The Air Force's DEX program lists the mass of its 16" missile version at roughly 9-12 kg [5]. To remain consistent with both dimensions and mass, the mass of the modeled projectile will be estimated at 9 kg (19.8 lbs). Calculating the normal force for each of the three modeled mach numbers at a pitching angle of 16° (largest pitching angle that retains stability) and dividing by the mass of the projectile yields the following load factors:

Speed	n (m/s^2)	n (g's)
Mach 0.2	21.52	2.19
Mach 0.4	86.25	8.79
Mach 0.6	193.30	19.70

Table 3.4.4 Projectile Load Factors at Pitching Angle of 16°

Making the simplifying assumptions that the turn radius of the modeled projectile during its final stage of flight is approximately equal to the radius in a level turn and that there is no sideslip occurring during flight, it is now possible to determine the approximate turning capability of the projectile. Performing a force balance of aerodynamic forces that include the normal force yield the following expressions for turn radius and turn rates in a level turn [35]:

$$r = \frac{v^2}{g\sqrt{n^2 - 1}} \tag{3.4.4}$$

$$\omega = \frac{v}{r} \tag{3.4.5}$$

Evaluating Equations 3.4.4 & 3.4.5 for each modeled speed produces turn radii and corresponding turn rates outlined in table 3.4.5. These parameters are also illustrated in figure 3.4.4(a). Note that v in the figure denotes the instantaneous tangential missile speed, the Mach

number in this case. Combining these two performance metrics, one is able to establish an accurate estimation of the turning capability of the munition.

Speed	r (m)	ω (rad/s)
Mach 0.2	241.88	0.281
Mach 0.4	216.22	0.630
Mach 0.6	215.94	0.946

Table 3.4.5 Turn Radii and Turn Rates for Modeled Speeds

While the maximum distance correction possible can be determined with the values in Table 3.4.5, the distance correction that is truly necessary within the 10 second window is dictated by the FOV of the sensor. Assuming the projectile is 1.5 km from the target when the seeker acquires control of the munition, and that the FOV of the sensor is 30°, simple geometry reveals that the maximum required correction is on the order of 0.4 km. The maximum turn radius and slowest turn rate listed in Table 3.4.5 (Mach 0.2) indicates the initial capability to achieve this requirement. Figure 3.4.4(b) shows this claim graphically, the drawing is to scale.
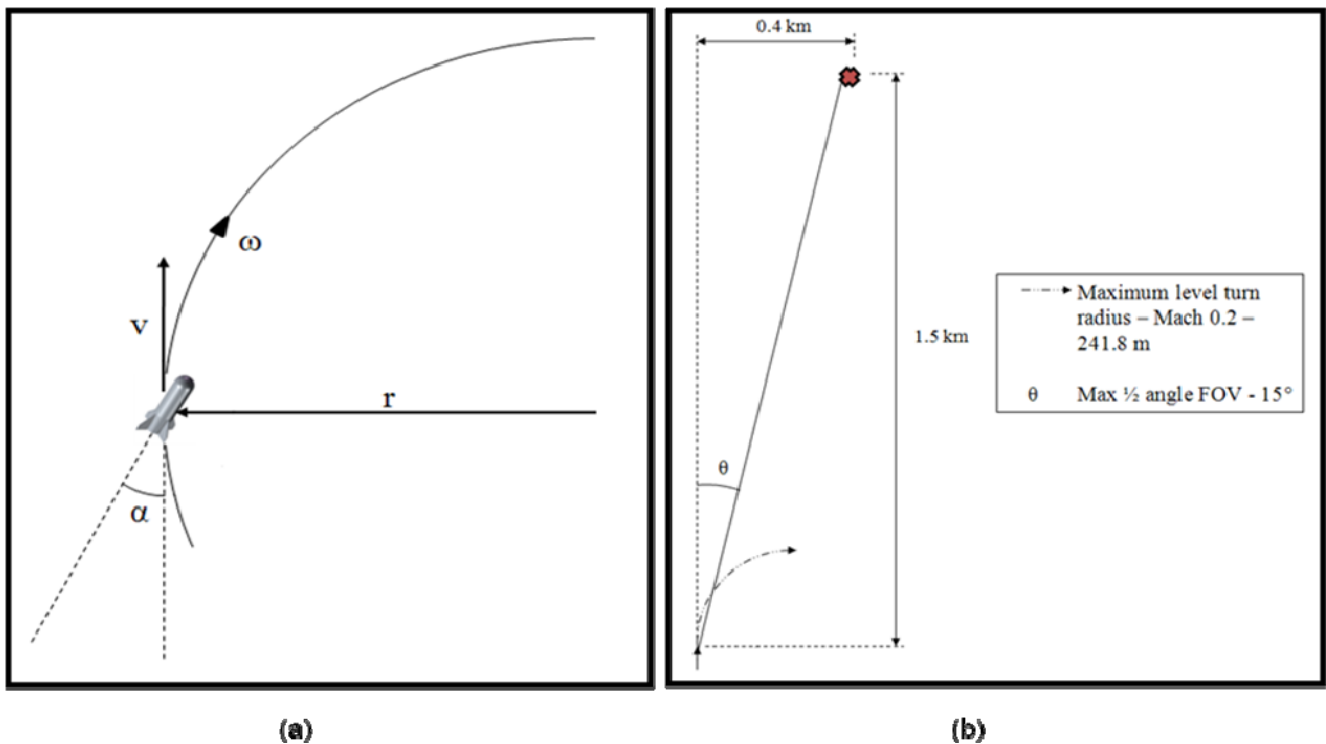
Figure 3.4.4 (a) Maneuverability Parameters, (b) Diagram Demonstrating Initial Turn Capability

More analysis is required, however, to achieve a complete dynamic model. The rough turn radii calculated and presented above are also affected by aerodynamic disturbances and missile control system dynamics such as time lags presented by the control loop. These issues must be addressed in depth to ensure that the munition will perform adequately in its flight environment. The author developed a simplistic flight simulation package in Matlab's Simulink that will allow for these factors to be included in the determination of the munition's true maneuverability characteristics.

3.4.4 Flight Simulation Description

Allowing for the inclusion of the time lags, noise, and other disturbances introduced during flight is essential when attempting to establish the performance metrics of the overall seeker system. The designer must be confident that the settling time of any control corrections or aerodynamic disturbances are less than the remaining time of flight in order to achieve a small miss distance. For this reason, the terminal stage of flight (final 10-12 seconds, seeker controlled flight) is modeled in order to obtain an accurate prediction of miss distances for the scenario previously introduced. The analysis operates under the assumption that the IMU places the projectile within the previously defined "acquisition basket", thus the initial IMU controlled portion of flight is not modeled.

A proportional navigation scheme, developed extensively in [37], is used as the guidance law to develop the missile feedback control algorithm. Proportional navigation operates by issuing acceleration commands perpendicular to the missile-target line-of-sight (LOS). The acceleration commands given to the missile control system are proportional to the rate of change of missile LOS (called the LOS rate) and the closing velocity of the missile with respect to its target. In equation form, the PN guidance law is stated as:

$$n_c = N'V_c\dot{\lambda} \tag{3.4.6}$$

where n_c is the acceleration command (m/s^2), N' is a unitless proportionality design gain (generally ranging from 3 to 5) called the effective navigation ratio, V_c is the missile closing velocity (m/s), and $\dot{\lambda}$ is the LOS rate (rad/s) [37].

In tactical missile seeker systems utilizing IR homing and proportional navigation guidance, λ and its time-derivative are measured by the focal plane of the seeker as described in section 2.1.2, while V_c is either estimated or measured on board the airframe.

The missile flight by proportional navigation is modeled in a two-dimensional subspace. For simplicity the model is assumed to be linear, a reasonable conjecture as all relevant flight angles are small (< 30°). Reference [37] demonstrates that linearized flight models produce results in close agreement with the non-linear models for most proportional navigation guidance simulations. This linearized model essentially claims that an acceleration command normal to the instantaneous LOS is approximately equivalent to a missile acceleration perpendicular to the velocity vector by relying on the fact that all angles are small [37]. Furthermore, the model assumes a flat, non-rotating earth and that the missile is traveling at a constant velocity towards a stationary target. Figure 3.4.5 depicts the 2-D simulation scenario.
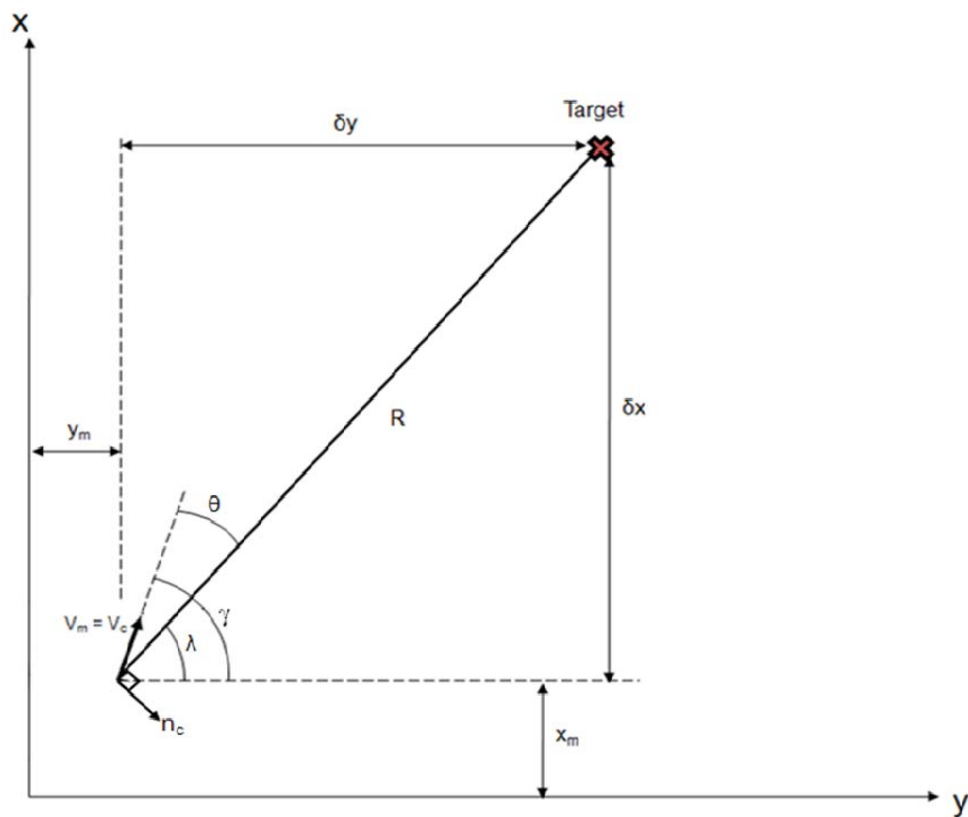
Figure 3.4.5 Two-Dimensional Simulation Geometry with Stationary Target

Examining Figure 3.4.5, the LOS (λ) is the imaginary line connecting the missile and target, θ is the heading error (HE), or the initial angular deviation of the missile from a collision course, and γ is the velocity vector angle. λ and γ are measured from a fixed reference, while θ is the difference between the two. γ is continuously changing via acceleration commands from the guidance loop in an attempt to match λ. Once the two angles are identical, the heading error angle will be zero and the missile will be on a collision course with the target.

The author is defining miss distance, also called the zero-effort-miss (ZEM), as the separation between the missile and target at the intersection of the instantaneous missile velocity vector and the line perpendicular to the velocity vector that intersects the target. Figure 3.4.6 portrays this concept pictorially. The "zero-effort" refers to the idea that if, at a certain point in the flight trajectory, control is abandoned and no effort is made to correct the course heading the miss distance will be dictated by the present heading error angle and range from the missile to target. In the model, a miss to the left of the target (as in the figure) is defined as positive (+), while a miss to the right is considered negative (-).
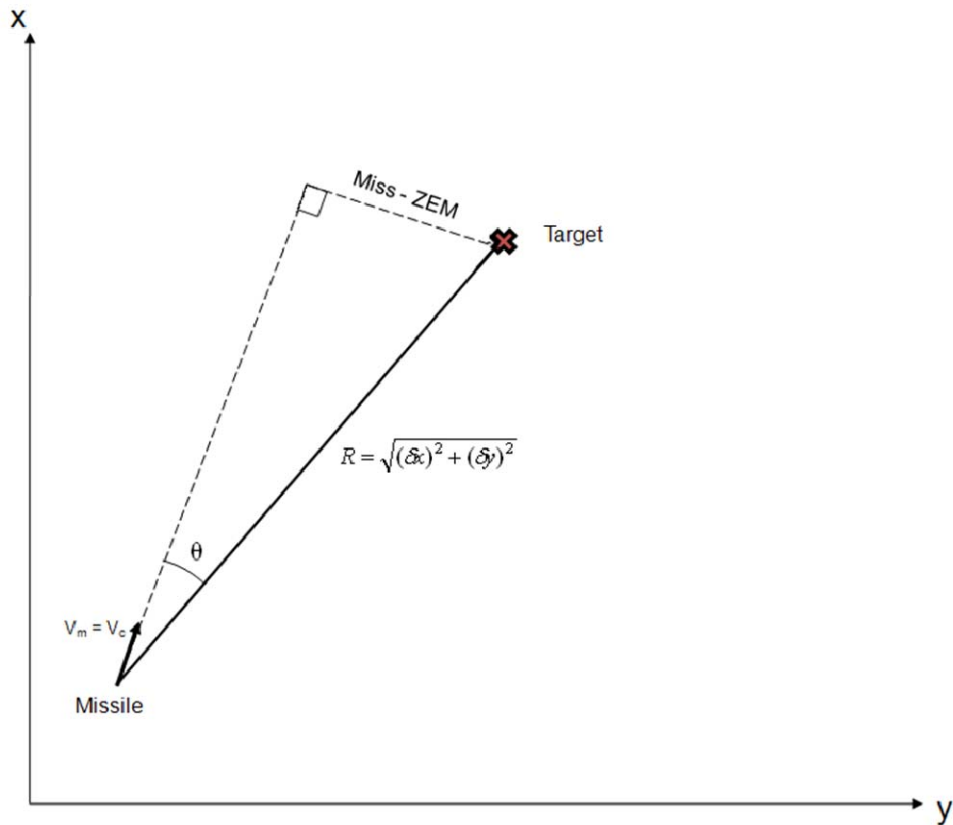
Figure 3.4.6 Miss Distance Geometry

75

3.4.5 Simulation Set-Up

The governing proportional navigation loop will begin with a set of initial conditions and will iterate until both missile-target heading error and LOS rate are driven to zero, indicating a collision course. The generic guidance loop resembles the block diagram shown in Figure 3.4.7. In tactical munition guidance, the quadrant detector seeker focal plane sets the desired heading error at zero ($\theta_d = 0$), concurrently defining a desired LOS (λ_d). Additionally, as demonstrated in section 2.1.2, the seeker focal plane performs the subtraction of λ from γ that yields the true heading error, aiming to set it to zero by making the two equivalent. The electrical circuit that measures LOS error (λ_e) in practice also differentiates it to produce the LOS rate ($\dot{\lambda}$). This line-of-sight rate measurement is fed into the guidance algorithm to compute the required acceleration command. The commanded acceleration (n_c) is then given to the flight control system, which prompts the control system actuators to deflect through the appropriate angle to produce the achieved airframe acceleration (n_A). The quantity is subsequently integrated twice to achieve an (x,y) position estimate to produce λ_t, completing the loop progression.

In practice: Seeker performs all operations within box
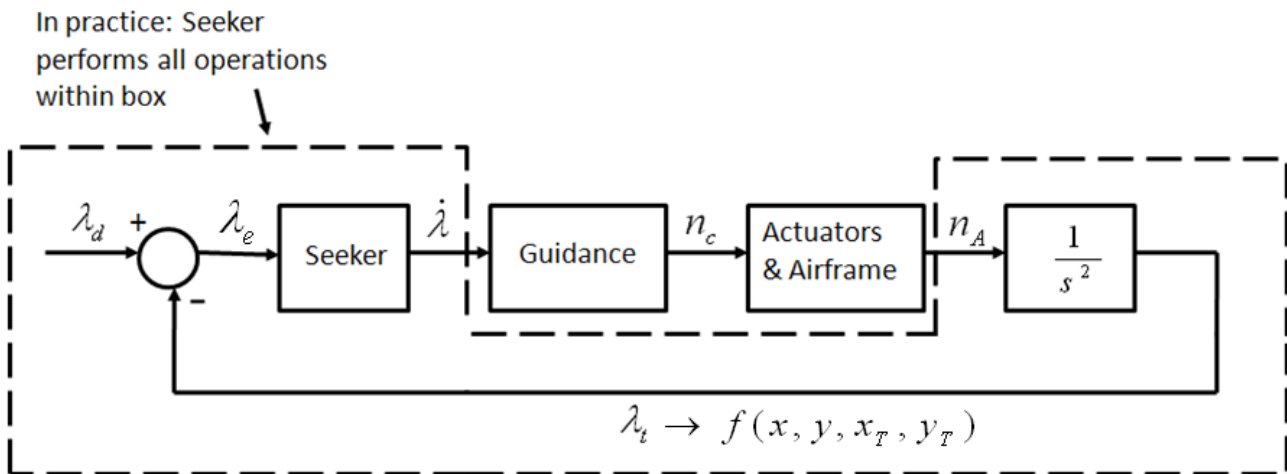
Figure 3.4.7 Simplified Proportional Navigation Guidance Loop

Using Simulink to develop the model above in two-dimensional space requires a more involved approach. Each of the components is modeled according to its physical operating characteristics. Additionally, some blocks require expansion to satisfy the demands of the more complex, two-dimensional, model. The block descriptions in the following paragraphs demonstrate the physical progression of the signal through the proportional navigation guidance

loop. Refer to Appendix D for the entire block diagram of the guidance loop model, as well as accompanying Matlab scripts for initializing variables and plotting output parameters.

Seeker

According to figure 3.4.6, the seeker block's function is to take in the (x,y) position of the missile with respect to the target, convert it to an accurate LOS measurement, and then differentiate that value to obtain an LOS rate. The LOS is obtained through a simple geometrical calculation. Depending on the initial conditions prescribed for the model (missile speed, seeker FOV, initial LOS error, etc.) the target is given a position within the 2-D operational subspace. δx and δy are calculated and fed into a block that computes λ as:

$$\lambda = \tan^{-1}(\frac{\delta y}{\delta x}) \tag{3.4.7}$$

Obtaining γ, also calculated in the model geometrically from x,y vector components of the missile velocity, allows for the calculation of θ according to equation 3.4.20, to be discussed in the following paragraphs.

$$\gamma = \tan^{-1}(\frac{V_y}{V_x}) \tag{3.4.8}$$

Following the LOS and velocity vector angle calculations, the subsequent seeker functional block is modeled as a differentiator with a slight time lag (T_s). The value for T_s is equal to the response time of the focal plane as described in section 3.2.4, and the transfer function governing this operation is represented [37]:

$$\frac{\dot{\lambda}}{\lambda} = \frac{s}{sT_s + 1} \tag{3.4.9}$$

where s represents the Laplace differentiation operator. The calculation of θ will be discussed later, as it dictates the actual expected miss distance of the projectile.

Proportional Guidance Calculation

The guidance algorithm block is simply represented by a gain factor representing equation 3.4.6, producing the commanded acceleration for the missile proportional to the LOS rate measurement.

Actuators

Once the commanded acceleration value is obtained from the proportional navigation algorithm, it is passed on to the autopilot and actuator system. This system then deflects the control surfaces through a certain deflection angle, δ, to achieve the commanded acceleration. This action also affects the dynamics of the control signal progression through the guidance loop. Autopilot and actuator transfer functions are typically represented by the familiar form of a second order transfer equation with non-unity gain:

$$\frac{\delta}{n_C} = K_{act} \frac{\omega_{act}^2}{s^2 + 2\varsigma_{act}\omega_{act}s + \omega_{act}^2} \tag{3.4.10}$$

where ω_{act} is the actuator natural frequency (rad/s), ς_{act} is the unitless actuator damping ratio, and K_{act} is calculated according to equation 3.4.11. K_{act} is the autopilot gain factor that converts the commanded acceleration value into the appropriate fin deflection angle (units – rad).

$$K_{act} = \frac{1}{g \cdot K_1} \tag{3.4.11}$$

where g is the acceleration due to gravity (9.81 m/s^2), and K_1 is aerodynamic acceleration gain (g/rad). The derivation of the quantity K_1 is shown in Appendix E. The servomotor mechanism that comprises the actuator system generally carries a natural frequency in the range of 10-25 Hz (62.8 – 157.1 rad/s) and an optimal damping ratio of approximately 0.707.

Airframe

The non-linear force and moment equations presented in the previous sections determine how the airframe will respond to control surface deflections produced by the autopilot and actuators. These equations are linearized in this analysis, much like the operating geometry, but again produce results in very close agreement with the non-linear representations, shown in reference [37]. The linearized airframe is represented as a single transfer function within the

algorithm to input a δ and achieve a normal acceleration. Using the approach based upon the airframe geometry derived in [37], the resulting transfer function is represented in familiar terms of the following second order equation:

$$\frac{n_A}{\delta} = \frac{K_1(1 - \frac{s^2}{\omega_z^2})}{1 + \frac{2\varsigma_{AF}}{\omega_{AF}}s + \frac{s^2}{\omega_{AF}^2}} \tag{3.4.12}$$

where ω_z is the airframe zero (rad/s), ζ_{AF} is the airframe damping ratio, and ω_{AF} is what Zarchan dubs the "airframe natural frequency" (rad/s). To avoid confusion, the reader should be aware that ω_{AF} is not the structural bending natural frequency of the airframe; it is the heading angle oscillation natural frequency during flight. The derivation for each of the terms in equation 3.4.13 is lengthy and cumbersome, so it will not be included here. See Appendix E for an explanation of these quantities for the munition geometry considered in this thesis.

It is important to note that the aerodynamic parameters derived in Appendix E, which factor into the calculation of the terms appearing in equation 3.4.13, are not constants, but vary with angle of attack [37]. Hence, the transfer function representation is an exact representation of the airframe's dynamical response only when the missile is traveling at a fixed speed, altitude, and angle of attack. Nevertheless, when considering the mission proposed by this thesis, the single transfer function is an adequate approximation for the entire flight regime for several reasons. First, the mission constraints assume a constant speed, negating any effects of varying velocities. Next, the altitude is specified to be 5 km or below, yielding atmospheric properties that are nearly homogeneous (i.e. air density/air pressure) when compared to the upper stratosphere, a space within which some missile airframes operate [35]. Lastly, as the results from Missile DATCOM have demonstrated, the designed missile's stable range of angle of attack deviates only 16° (0.28 rad) from the trim condition, diminishing the effect of large changes in the aerodynamic parameters that occur at high angles of attack.

Another note of importance is that there must exist a saturation limit on the number of g's that the airframe can sustain without going unstable. Table 3.4.4 outlined these saturation limits based on the results produced by Missile DATCOM. Thus, it is necessary to insert a block that will limit the achieved acceleration based upon the speeds at which the munition is traveling.

The block is introduced after the airframe block in order to ensure that the projectile does not exceed the specified load factor limit. If this block were omitted, the simulation would deviate from reality by allowing the missile to achieve a lateral acceleration that is beyond the capable range of the airframe at its prescribed speed.

Missile as a Double Integrator

The final block shown in figure 3.4.6 is the double integrator operation. As the diagram indicates, the seeker is able to obtain the updated λ_t directly via the IR signature on the focal plane. However, in the simulation model this operation amounts to calculating the new x,y position of the munition and comparing it to that of the target. Given initial position and velocity information for the missile, the updated position is found by integrating the achieved missile acceleration twice. Thus, the governing equations resemble the following integral representations:

$$V_X(t) = \int_0^t n_{AX}\,dt + V_{0X} \tag{3.4.13}$$

$$V_Y(t) = \int_0^t n_{AY}\,dt + V_{0Y} \tag{3.4.14}$$

$$X(t) = \int_0^t V_X\,dt + X_0 \tag{3.4.15}$$

$$Y(t) = \int_0^t V_Y\,dt + Y_0 \tag{3.4.16}$$

yielding the x and y location of the missile after a certain period of time. The final operation in the model loop seeks to obtain δx and δy for the calculation of θ. These two quantities are computed as:

$$\delta x = X_T - X(t) \tag{3.4.17}$$

$$\delta y = Y_T - Y(t) \tag{3.4.18}$$

where X_T and Y_T are the x and y coordinates of the target in the 2-D operational subspace. With this calculation, the model loop will proceed until the missile either hits the target, or moves beyond the target position at a measureable miss distance.

The preceding paragraphs convey loop progression of the proportional navigation guidance algorithm. The goals of the simulation are to map out the flight trajectory within the 2-D operational subspace and obtain an accurate estimate of the miss distance defined in figure 3.4.5. For this reason, the model calculates the miss distance according to the figure as:

$$Miss = R \cdot \sin(\theta) \tag{3.4.19}$$

where the heading error angle is calculated, also as depicted in the figure, as:

$$\theta = \gamma - \lambda \tag{3.4.20}$$

With the simulation fully set up, it is now possible to input varying scenario conditions to determine if the munition will impact the target.

3.4.6 Generic Simulation Results

Although the specific parameters of the focal plane hardware are not available at this point because the design trade study has yet to be completed, it is still beneficial to obtain results for a generic scenario. This analysis allows the designer to ensure that the model is functioning properly, as well as yielding insight into how each block (i.e. airframe, actuators, etc) affects the dynamical response of the munition during flight. The missile airframe data is readily available from the initial design, and the actuator range of specifications is ubiquitous for nearly all airframes. The assumption that the actuator is on the low end of the performance range is reasonable in this case. The reader will note that the model is not run for the multiple munition speeds and target distances. This is because the author only seeks to introduce basic simulation results to the reader; specific scenario modeling will come later when a final design is chosen. Thus, the author defines the boundary and initial conditions of the simulation scenario as follows:

Parameter	Value	Description
N'	3.5	Prescribed effective navigation ratio
$\mathbf{V_x}$	208 m/s	Munition is traveling at Mach = 0.6 in x-direction
$\mathbf{V_y}$	0 m/s	Munition has no initial velocity in y-direction
$\boldsymbol{\theta_0}$	15°	Initial HE is at extreme edge of focal plane FOV
$\mathbf{X_T}$	1500 m	Target x position reasonably prescribed
$\mathbf{Y_T}$	402 m	Target y position set by initial LOS
$\mathbf{X_0}$	0 m	Initial munition position is set to the origin of 2-D operating area
$\mathbf{Y_0}$	0 m	
$\boldsymbol{\omega_{ACT}}$	10 Hz = 62.8 rad/s	Low end of available actuator performance
$\boldsymbol{\zeta_{ACT}}$	0.707	Optimal damping ratio
$\mathbf{T_s}$	10^{-3} sec	Seeker time lag/response time
$\boldsymbol{n_{sat}}$	193.3 m/s^2	Max lateral acceleration capability at 200 m/s (M=0.6)
$\boldsymbol{\omega_{AF}}$	28.34 rad/s	Airframe heading angle natural oscillation frequency
$\boldsymbol{\zeta_{AF}}$	0.025	Airframe is very lightly damped
$\boldsymbol{\omega_Z}$	41.397 rad/s	Airframe zero
K1	- 0.614 g/deg	Aerodynamic acceleration gain

Table 3.4.6 Initial and Boundary Conditions for Simulation

This scenario matches the mission setting in which the munition is released from a distance of 10 km traveling at M = 0.6 to the target with nearly 8 seconds of target illumination time. It assumes that the IMU drift error has caused a deviation in the desired flight path and has placed the target at the edge of seeker's FOV. Figure 3.4.8 (a) displays the flight trajectory of the missile. It is evident that the oscillation of the airframe damps out in an adequate amount of time. The airframe oscillation, depicted in figure 3.4.8 (b) is caused by the very light damping ratio of the airframe itself. It turns out that in practice, the actuators have a very minimal effect on the oscillatory response due to a change in heading. Figure 3.4.9 demonstrates this point. Running the simulation without the effects of the airframe dynamics yields a zero-effort-miss distance plot that briefly overshoots the ideal curve (ideal → no actuator dynamics) and then progresses smoothly to zero, impacting the target at approximately 7.8 seconds. The slight overshoot is caused by the dynamics of the actuator, which disappear in less than 0.15 seconds. Including the airframe transfer function, however, results in the oscillatory behavior with a time-lag shown in (b). The oscillation and time delay is brought about by the lightly damped structure of the airframe attempting to match the curve shown in Figure 3.4.8 (a). Despite the oscillation caused by the inclusion of the airframe dynamics, the missile still impacts the target directly.
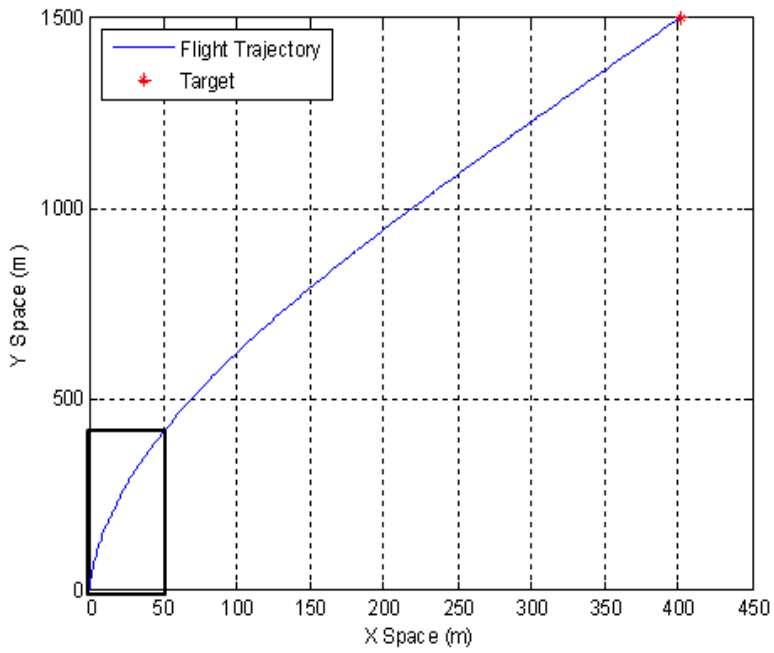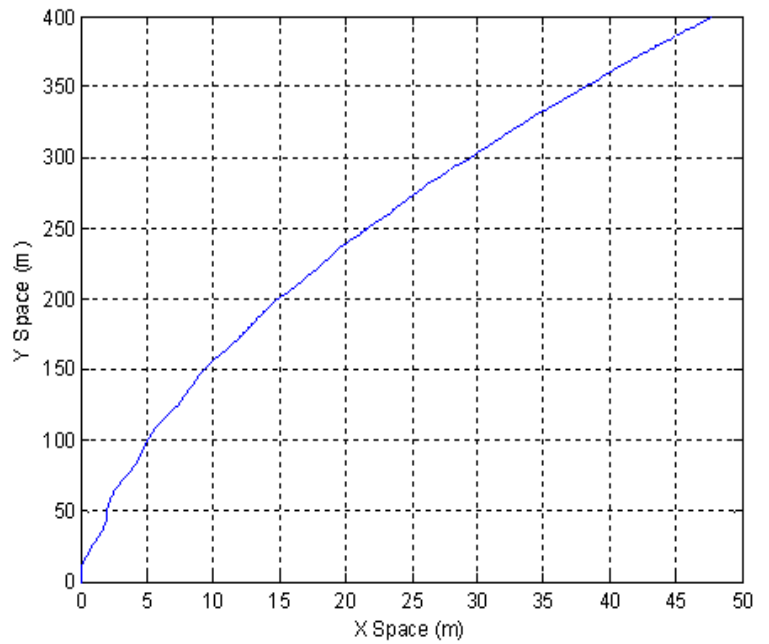
Figure 3.4.8 (a) Full munition flight trajectory, (b) Box close-up showing airframe oscillation
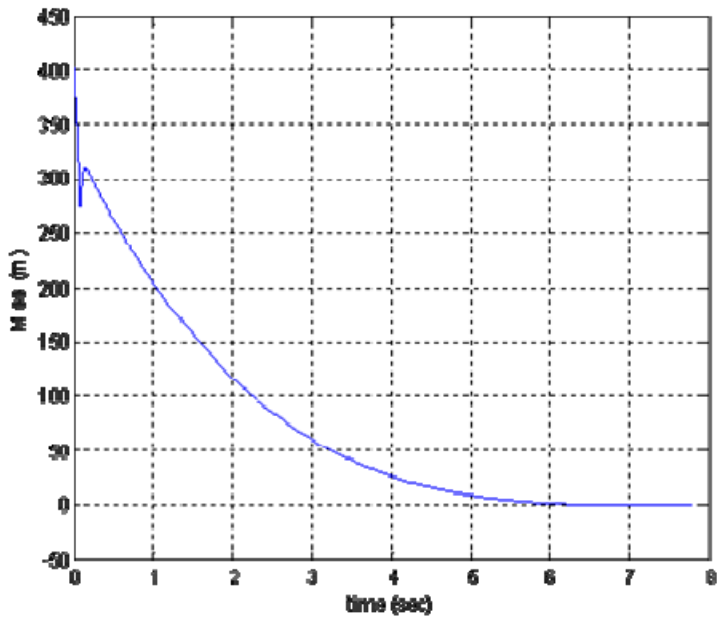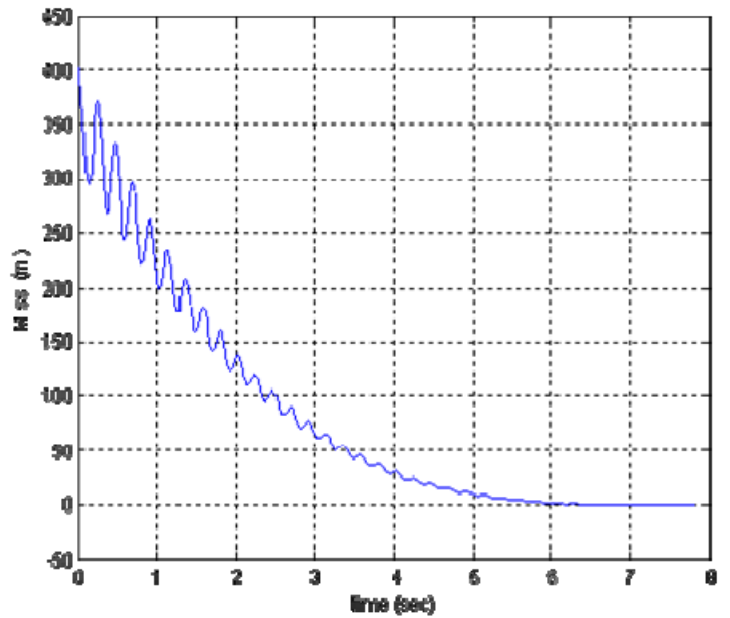
Figure 3.4.9 ZEM over time (a) without airframe dynamics, (b) with airframe dynamics

In fact, given adequate time to acquire the target (as in this scenario) the simulation run as is will hit the target with more than adequate error in any situation that is within the bounds of the mission constraints. That is, as long as the target is within the missile's FOV and the package is given enough time to maneuver, there will be minimal error. The airframe damping, although significantly affecting the flight path, does not alter the trajectory to the point that the missile will impact with greater than 1.5 m CEP. Nevertheless, the current simulation is ignoring the effects of noise from within the seeker as well the target signal.

3.4.7 Noise Inclusion

Up to this point, it has been assumed that the seeker is able to perfectly measure the λ (and corresponding $\dot{\lambda}$). However, in practice, noise sources such as glint, scintillation, and thermal effects limit the precision of the seeker system and degrade the expected miss distance values [38]. The analysis conducted above omitted these effects to introduce the reader to the simulation and to present a baseline from which to work. Certainly, for later simulations of prospective scenarios and candidate systems, seeker and signal noise sources must be included to maintain authenticity.

In the model, the aggregate of seeker LOS rate error sources is modeled as Gaussian white noise [38]. The author specifies the noise power for all subsequent analyses at a value of 2 mrad/s (0.115°/s), a value consistent with (and slightly more conservative than) published models [39]. The noise source is added to the LOS rate measurement made by the seeker and passed to the proportional guidance algorithm.

In order to obtain a reliable statistical sample set from which to derive a mean and standard deviation for the miss value, the author ran the flight simulation model 200 times. Using the exact same initial and boundary conditions input previously (Table 3.4.6), the miss distance changes from the singular value of 0.0768 m to a mean value of 0.0478 m with a standard deviation of 0.243 m. The reader can see exactly how the additive LOS rate noise affects the ZEM estimates for a sample run by observing figure 3.4.10. As the LOS and corresponding LOS rate are decreasing, the additive noise demonstrates a more profound effect upon the final miss estimates. The inset plots of figure 3.4.10 show close-up views of the final

1.8 seconds of flight and reveal that the noise inclusion affects the miss distance somewhat significantly.
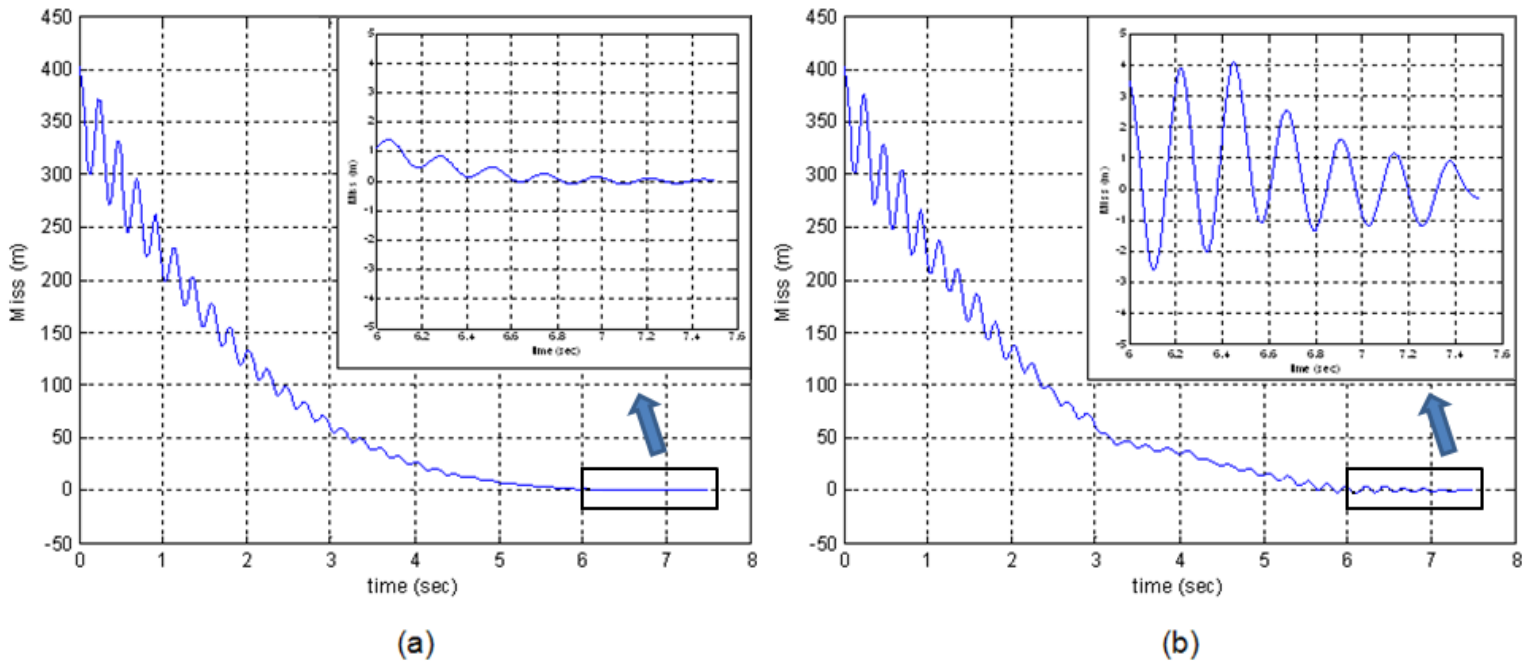
Figure 3.4.10 ZEM as a function of time (a) without LOS rate error, (b) with LOS rate error

The author also ran the simulation at the two other modeling speeds (with identical initial and boundary conditions as above) in order to obtain a comparative measure of how the noise affects the miss distance estimates across the range of modeling scenarios. While the results with additive noise predict miss values on the same order as those without the noise, they give the designer an added level of confidence in the accuracy of the simulation. Including uncertainty in the model allows the designer to determine the "3σ" miss value, the mean of the trial runs plus three times the standard deviation of the sample set. The expected error will be less than the 3σ value 99.7% of the time. If this value is below the 1.5 m CEP requirement, the designer is very confident in the performance of the system. The comparative quantitative results of the original runs and the averaged runs are summarized in Table 3.4.7.

Speed	Miss - No Noise (m)	Mean Miss - With Noise (m)	Std Dev - With Noise (m)
Mach 0.2	3.02E-06	0.0032	0.0368
Mach 0.4	0.0080	0.0018	0.1204
Mach 0.6	0.0768	0.0478	0.2430

Table 3.4.7 Comparison of expected ZEM values with and without added LOS rate error

Based upon the results of including the additive LOS error by means of Gaussian white noise, the designer is confident to move forward in the design process with the present simulation model. In each of the above cases, the 3σ miss value is less than the 1.5 m requirement for each of the modeling speeds. And while the analysis was merely one, generic scenario, the ability of the model to produce a large number of sample runs from which to derive the statistical properties gives validity to the results. It truly presents the designer with a robust analysis tool to model candidate systems as they are formed in the subsequent chapters.

3.5 Wrap-Up

The optical sensor analysis demonstrated the required performance measures for successful detection of the target signature at varying levels of relative humidity. The results of this specific analysis (Table 3.2.5) combined with the information gathered by component survey demonstrate that an off-the-shelf quadrant detector array will be more than sufficient for the thesis mission.

The inertial sensor analysis illustrated the stringent performance constraints required for an all-IMU guidance system and subsequently revealed the utility of relaxing the performance demands by adding a terminal guidance seeker. Additionally, the product information collected in the technology survey aided the author in paring down the listing of acceptable IMU's for the purpose of achieving mission success.

Modeling the projectile dynamics also served a great role in furthering the system design process. The model dimensions have been specifically designed to be similar to those tactical munitions currently being considered for precision guidance upgrades. The results obtained via Missile DATCOM and Simulink models demonstrate that the designed projectile has both the stability and maneuverability to meet the requirements of the mission for which it will be used. The two modeling packages give the tactical missile guidance designer invaluable tools that

allow for the prediction of missile performance in an otherwise unknown environment. Specific scenarios will subsequently be modeled and design trades will be considered based on the output results of both modeling packages.

The upcoming analysis will build upon the groundwork set forth by the development in this chapter and will determine the optimal combinations of performance parameters of individual component combinations to accomplish the mission goals while mitigating the cost of the system.

4   System Design Considerations

4.1 Overview

With the technical analysis of the individual components that will comprise the total seeker system complete, the designer can now move into the synthesis process. This consists of assembling a packaged system of the aforementioned components that will meet the mission requirements while optimizing the three selection criteria specified at the outset of the endeavor: accuracy, cost, and size/weight.

This chapter will expose the reader to the individual importance of each of the stated selection measures. Additionally, it will assess how the components studied in each of the technology surveys perform with respect to each criterion. The author proposes candidate systems to be modeled to develop comparative metrics with which to judge, and eventually select, the best possible combination of seeker, IMU, and control parameters. Finally, as this study is truly a systems analysis, there is a necessity to address the effects of human involvement to the scenario as a whole. Including these considerations allows the system designer to address performance factors that are often vital, but possibly overlooked, in the design process.

4.2 Selection Criteria

The selection criteria are derived from the three most vital requirements of the system. So, each candidate system design is judged based on accuracy, cost, and size/weight. Recall that the mission requirements dictate that the system: (a) retain an accuracy value of 1.5 m CEP or less, (b) cost less than $15,000, and (c) fit within an area 4" in diameter or less. Certainly, all of these measurement factors are interrelated; a large and expensive system may offer pin-point

accuracy, whereas a small, cheap system may not offer the type of accuracy required to meet the mission constraints. Thus, trade-offs are required to maximize the value of the complete system package. These design trades must be carefully considered from many different viewpoints prior to finalizing a system. The following paragraphs will further develop the individual selection criteria and explain how they fit in with the overall picture of the seeker system design.

4.2.1 Accuracy

Humanitarian considerations far outweigh any other factor in the process of determining the optimal system. Thus, accuracy is the most vital of all performance parameters for the seeker system. If the CEP eclipses the established 1.5 m limit, there is mission failure. As all surveyed quadrant photodiode arrays offer very similar (or identical) operating characteristics, this judging criterion falls mainly on the IMU component of the system. Even then, with the addition of the IR terminal guidance capability, there exists a range of capable IMU options, as shown in section 3.2.3. The focus of the design trade section will be on determining the miss distance performance from the projectile flight simulation model presented in section 3.4.4 given variable initial conditions dictated by the IMU error characteristics of each individual option.

4.2.2 Cost

The cost of the system is the second most important factor in this study. The initial goal of undertaking this thesis research was to come up with a low-cost design for the reasons expressed in section 1.1.1. Once again, the major price disparities exist with the IMU's. The flight computer will cost the same regardless of the IMU and photodiode arrays with which it will interface. Even the quad cell photodiode arrays present much less of a cost burden upon the system. Thus, while the total system package is being designed to be less than $15,000, the IMU presents the component that will most heavily affect the final system price.

Furthermore, the process of designing, packaging, and assembling all hardware components into a single system may require a larger price tag than the components themselves. The design/packaging costs are more difficult to predict than the component costs, which are readily available from the technology surveys completed in Chapter 3. Thus, the design trade

section will address this issue by finding the least expensive combination of components that still satisfies the other mission requirements.

4.2.3 Size/Weight

At this point in the analysis size and weight do not present much of an issue. All of the components studied to this juncture are MEMS devices of extremely small size and weight. In fact, the candidate list for components has already been pared down largely by the fact that the seeker system design is to be an all-MEMS package. All individual components gathered from the technology survey readily fit within a 4" diameter. Nevertheless, the designer must still determine an optimal geometry so the entire system assembly has the ability to be placed inside the munition's outer casing. The packaging of the system again becomes a major issue with respect to this criterion. Nevertheless, given the nature of the component sizes, the author assumes that this operation is possible and will place the majority of the weighting on the previous two judging criteria.

4.3 Candidate Systems

The selection of candidate systems has virtually been completed by the photodiode array and IMU analyses conducted in previous chapters. The remaining design milestone is to combine the hardware components to develop system alternatives that can be modeled and compared with one another. After this step, the designer is able to weigh the benefits and drawbacks of each option and ultimately select the final system for testing/prototype.

Despite the fact that there are a myriad of hardware alternatives in the design of a precision seeker system, the one true variable factor in this analysis, as described in the previous subsection, is the IMU. The disparity among the accuracy and cost characteristics of the IMU component are more pronounced than any other system element. Thus, the primary devotion of this subsection will hinge upon the differences in the IMU options. Certainly, the designer must not discount the other elements of the system make-up, but it is evident at this level of analysis that the IMU is the so-called "pinch-point" that will determine the overall performance and cost efficiency of the system. The selection of candidate systems will begin with a brief focus on the

selection of a photodiode array, and will subsequently move into combining it with an IMU to evaluate alternative systems.

4.3.1 Photodiode Array Selection

The surveyed photodiode arrays spread a broad range of costs, from approximately $25.00 to $1386.00. The higher end of the cost spectrum contains rugged, hermetically sealed, quadrant detectors optimized specifically for military applications. The more expensive options offer better off-the-shelf reliability and improved ability to withstand the shock of handling/launch. It is the position of the author that these military grade detectors are over-designed for the application considered in this thesis. The analysis in section 3.2.3 demonstrates that an off-the-shelf quadrant detector with a photosensitivity of 0.4 A/W offers a very high SNR at an approximate distance of 5 km from the target. Thus, due to the nature of the mission considered by this thesis, the author finds the quadrant cell photodiode array offered by Advanced Photonix (API SD 380-23-21-051, figure 4.3.1) priced at approximately $210.00 as an adequate option.

The designer must be aware that there may arise a mission down the road that demands the use of a solidly housed, hermetically sealed quad cell photodiode array. This situation would call for the use of a model such as the API SD 551-23-41-221 ($1386.00), which is designed explicitly for military operation on laser guided munitions. However, due to the less demanding nature of the scenario considered by this thesis and the analysis previously conducted, the cheaper alternative promises to be sufficient.

4.3.2 Candidate System Identification & Modeling

Moving forward with the selected quadrant detector, there are four options for the candidate systems, corresponding to four of the five remaining IMU options from section 3.2.3 (note that the author is only considering one AIS IMU because selection criteria similarity). The guidance control electronics (flight computer) is considered to be a static hardware choice, meaning although it will affect the total system cost, there are no alternatives being considered. The four candidate systems, outlined in Table 4.3.1, will be referred to as system #1 – system #4.
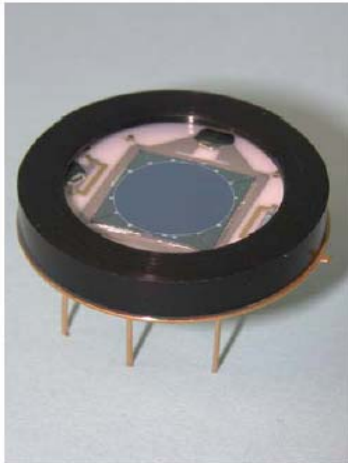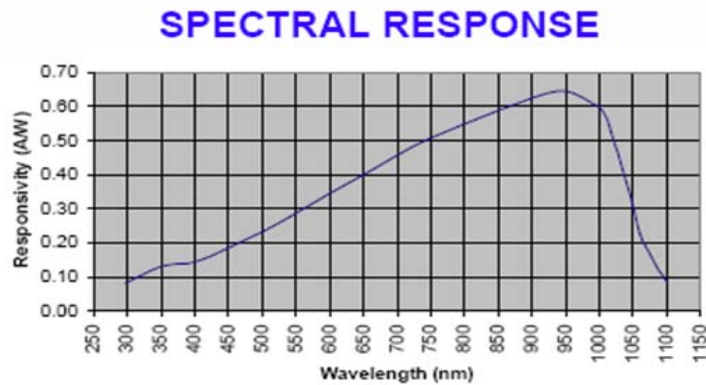
Figure 4.3.1 (a) API SD 380-23-21-051 Quad Cell Si Photodiode and (b) Spectral Response

Option #	Photodiode Array	IMU
1	API SD 380-23-21-051	Honeywell HG1930
2	API SD 380-23-21-051	AIS SiIMU02
3	API SD 380-23-21-051	Systron MMQ 50 IMU
4	API SD 380-23-21-051	MAS IMU01

Table 4.3.1 Candidate Seeker System Hardware Components

Each of these options was input into the simulation model to obtain miss distance estimates for the three modeling speeds with an acquisition distance of 1.5 km. The initial target distance is assumed to be 10 km. Ten kilometers is the largest of all target distances and allows the maximum value of IMU error to propagate for each modeling speed. This is the author's attempt to model a type of "worst-case" situation to obtain a measure of each system's performance. In the scope of the thesis, limiting the modeled scenario to an initial target standoff distance of 10 km provides adequate information with which to move forward in the design process. The author assumes that sufficient performance in this modeling scenario translates to mission success in less demanding situations (i.e. closer targets & less IMU error accumulation). However, in designing for more challenging circumstances, one will likely be required to model many different initial standoff ranges with varying acquisition distances.

Again, each model was run 200 times to obtain a statistical average of the expected miss values. The results for each option are summarized in tables 4.3.2 - 4.3.4. The model output

demonstrates that all options yield 3σ miss distance estimates that fall within the 1.5 m CEP constraint. The only IMU that does not yield sufficient performance is the Systron Donner option for a munition traveling at Mach 0.2. It allows too much IMU error to propagate and places the target signature outside the focal plane's field of view. Nevertheless, to keep the rest of the results in perspective, the miss values listed in tables 4.3.2 - 4.3.4 are significantly less than those of an the all-IMU systems utilizing the same inertial measurement units (tables 3.3.4 – 3.3.6). Note that the 3σ miss numbers are displayed as absolute values.

Option	Gyro Bias (°/hr)	Seeker Aided - Initial HE	Seeker Aided - Mean Final Miss (m)	Seeker Aided - Miss Std Dev (m)	Worst-Case 3σ Miss
#1 - Honeywell	20	2.698°	-0.0013	0.0387	0.1173
#2 - AIS	6.5	0.868°	-0.0001	0.0368	0.1104
#3 - Systron	150	19.78°	N/A	N/A	N/A
#4 - MAS	60	8.027°	0.0029	0.0356	0.1098

Table 4.3.2 Final Miss Estimates– M = 0.2, 1.5 km Acquisition Distance, 10 km Target

Option	Gyro Bias (°/hr)	Seeker Aided - Initial HE	Seeker Aided - Mean Final Miss (m)	Seeker Aided - Miss Std Dev (m)	Worst-Case 3σ Miss
#1 - Honeywell	20	1.373°	0.0056	0.1206	0.3673
#2 - AIS	6.5	0.442°	0.0024	0.1198	0.3619
#3 - Systron	150	10.18°	-0.0045	0.1341	0.4069
#4 - MAS	60	4.093°	0.0088	0.1211	0.3720

Table 4.3.3 Final Miss Estimates– M = 0.4, 1.5 km Acquisition Distance, 10 km Target

Option	Gyro Bias (°/hr)	Seeker Aided - Initial HE	Seeker Aided - Mean Final Miss (m)	Seeker Aided - Miss Std Dev (m)	Worst-Case 3σ Miss
#1 - Honeywell	20	0.897°	-0.0151	0.2518	0.7705
#2 - AIS	6.5	0.289°	0.0037	0.2474	0.7459
#3 - Systron	150	6.670°	0.0430	0.2387	0.7590
#4 - MAS	60	2.675°	-0.0144	0.2361	0.7226

Table 4.3.4 Final Miss Estimates– M = 0.6, 1.5 km Acquisition Distance, 10 km Target

4.3.3 Candidate System Design Trades

Having input each system candidate into the modeling program to obtain performance predictions, the guidance system designer is now ready to develop the design trades of each individual system against the others in order to determine the most cost-effective missile seeker

system. To effectively determine the best available system, the designer again turns to the selection criteria. Plotting each of the systems' specifications relating to the judging measures allows the designer to clearly identify the strengths and/or weaknesses of each of the specific design alternatives. Figure 4.3.2 shows each of the candidate system's accuracy (in the form of the worst case 3σ miss value), cost, and size characteristics plotted in 3-D for a modeling speed of M=0.6. The other two modeling speeds have strikingly similar plots (save for the Systron option at Mach 0.2), thus, they are not included. As mentioned previously, size is the one selection criterion that will not be a major factor into the selection process for this specific scenario. Nevertheless, it is included in the plot to demonstrate the utility of plotting a group of systems against all pertinent judging measures in order to obtain an accurate view of the optimal choice.
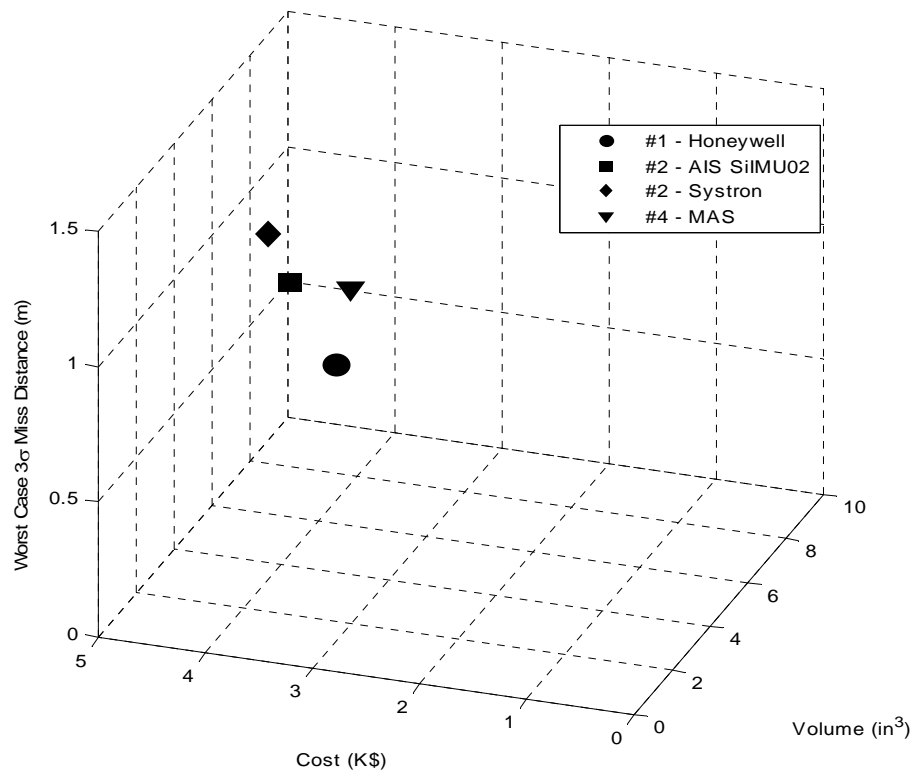

Figure 4.3.2 3-D Design Trade Plot of Candidate Seeker Systems

Looking at the 3-D trade plot, the reader should again note that a data point closer to the origin generally signifies a more desirable option. For a mission which cost is of paramount importance, given that the other two selection criteria are adequately satisfied, the designer will

likely choose the lowest priced option and move forward. However, a system designed for alternative scenarios may require some other performance parameters to which the guidance system designer should pay close attention. Furthermore, there may also be integration and compatibility issues that are necessary to address. Before selecting a finalized system design, the designer must consider all possible variables to ensure that the system is truly ready to be placed into operation. The following subsection brings to light some of the human factors that will affect the system performance.

4.4 Inclusion of Human Factors

The system hardware trades have now been exposed and the hardware selection process is nearly finished. There remains, however, the analysis of human involvement of the personnel operating at various stages of the munition's employment. Invariably, human communication is the dominating factor that determines the success of an endeavor such as the one presented by this thesis. The interaction between human beings is a much more dynamic and complex design space than that of the guidance hardware. Therefore, the guidance system designer must be absolutely certain that human factors are taken into account in the analysis. Otherwise, even the most capable system hardware could fail due to some unforeseen variable arising from human interaction. Just as hardware specifications were modeled and simulated, the designer must attempt to model and simulate human involvement to ensure the system will be successful. To remain within the scope of this thesis, the author cannot attempt to model and address the countless issues that arise due to human factors. However, the system designer must be aware that they are present and have the ability to make or break a mission. Although with limited depth, the author will address two major areas of human involvement that are of particular utility to the thesis analysis.

The primary set of issues of human concern to arise is the location of the launch in the target subspace. First, there must exist a finite launch window from which it is ideal for personnel to fire the munition. Within, and only within, this space, the munition can be released or fired. Preferably, the launch window for the thesis scenario is an area 5-10 km from the target, either at ground level for mortar/artillery rounds, or roughly 1-2 km above the ground for air launched projectiles, yielding direct line of sight. Launching from distances beyond the

window could cause an excess of angular error from the IMU to propagate, rendering the target outside the focal plane's FOV at the control handoff. Launching from distances closer than 5 km may present several undesirable scenarios. It may not allow the laser designator operator enough time to ensure the accuracy of target location. It could possibly present too great of a time constraint to complete the required communication agreements amongst launching/designating personnel. It also eliminates the safety buffer between the launching personnel and the target, making early detection possible and likely exposing them to quick retaliation from the adversary. Any of these situations could cause mission failure, so firing from outside of the designated window cannot be allowed. As the thesis is presenting a design methodology, note that the acceptable launch window will likely change given alternative scenarios and conditions.

A secondary issue with the location of the launch is the orientation of the munition with respect to the laser designator within the target subspace. The munition's focal plane must be able to capture the reflection of the laser designation signal from the target. If the munition were to enter the target subspace progressing towards the designation signal, it will not see the reflection and will likely lock on and guide to the location of the operator, a very undesirable situation. Thus, there must be some finite angular window encompassment, Ψ, from which it is safe to fire. The bisection of the angular window proceeds 10 km from the center of the target through the designator and sweeps $\Psi/2$ in each direction. The actual prescription of the value Ψ is beyond the scope of the thesis, but it is important to point out that such a window exists. The combination of the acceptable release areas described by distance and angle form the overall acceptable launch window. Figure 4.4.1 illustrates this window as it is described by the previous paragraph.

The next, and relating, issue is that the personnel launching/releasing the munition must have clear communication with the individual operating the laser designation system. There must be some mutual, spoken, agreement amongst the personnel operating on both sides of the munition's life cycle that the target coordinates are correct, it is in sight, the munition is ready to be launched, and that the designator should be turned on. As one example: when the munition is fired, the launching personnel must alert the designator at the exact time of launch to be sure that the designator is illuminated at the correct time. Delaying the alert to the designator may cause the target to be painted for less than an acceptable amount of time. This will likely cause mission failure, which is unacceptable.
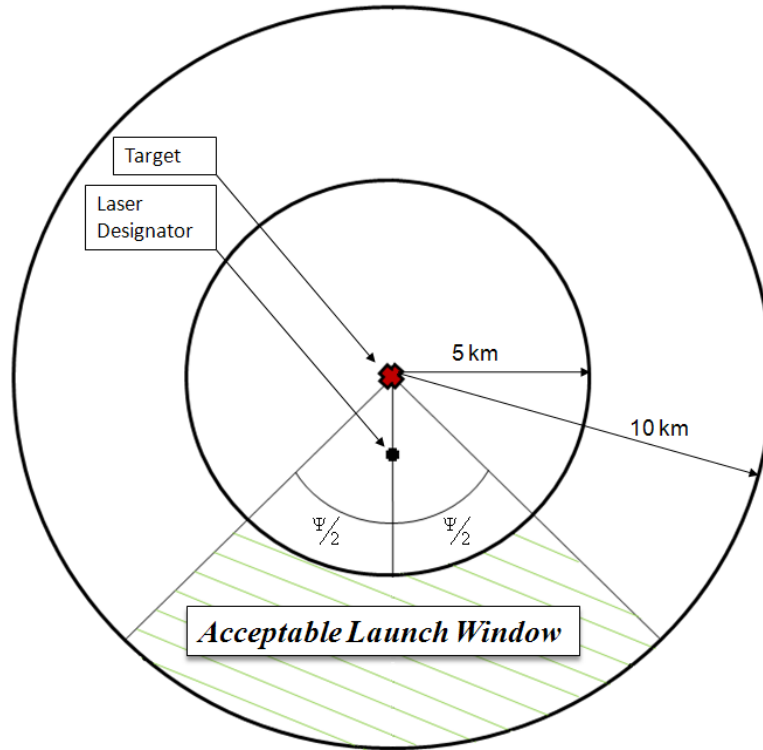
Figure 4.4.1 Depiction of Launch Window for Human Factors Consideration

The author modeled the latter of the two aforementioned human issues in an attempt to illustrate the effect human factors may have on the outcome of the mission. Specifically, the situation in which the designator illuminates the target shorter than the prescribed 10 s time was modeled. While the modeling of this situation demonstrates the outcome of illuminating the target at the incorrect time, it may also be viewed as the situation in which the designator is only able to illuminate the target for a fraction of the planned designation time due to personnel exposure concerns. Viewed from either perspective, the situation the author modeled the situation and plotted the estimated miss distance against the time-to-go at target acquisition (illumination time). The model assumes the maximum initial heading error at acquisition, 15°, so that the target is just within the focal plane's FOV. The results of 10 averaged runs are plotted in figure 4.4.2. The plot illustrates that the designed munition retains sufficient maneuverability to impact the target accurately at speeds of Mach 0.6 and Mach 0.4 with less than a second of illumination time. At Mach 0.2 the munition is less maneuverable and requires a minimum illumination time of just less than 4 seconds to achieve the accuracy goal.

Although the prescribed illumination time is generally 10 seconds, the plot demonstrates that it is only necessary that the laser designator operator paint the target for a maximum of 4 seconds for a munition traveling Mach 0.2, and 1 second for munitions traveling Mach 0.4 or 0.6. This gives the launching personnel some latitude in communicating with the designating personnel. Thus, the spoken agreement doesn't necessarily have to take place 10 seconds before impact. Additionally, it is important to keep in mind also that a major goal of the system design is to maximize the safety of ground personnel. A vital piece of information that is also gleaned from the simulation results is that the vulnerability of the laser designator can be restricted by
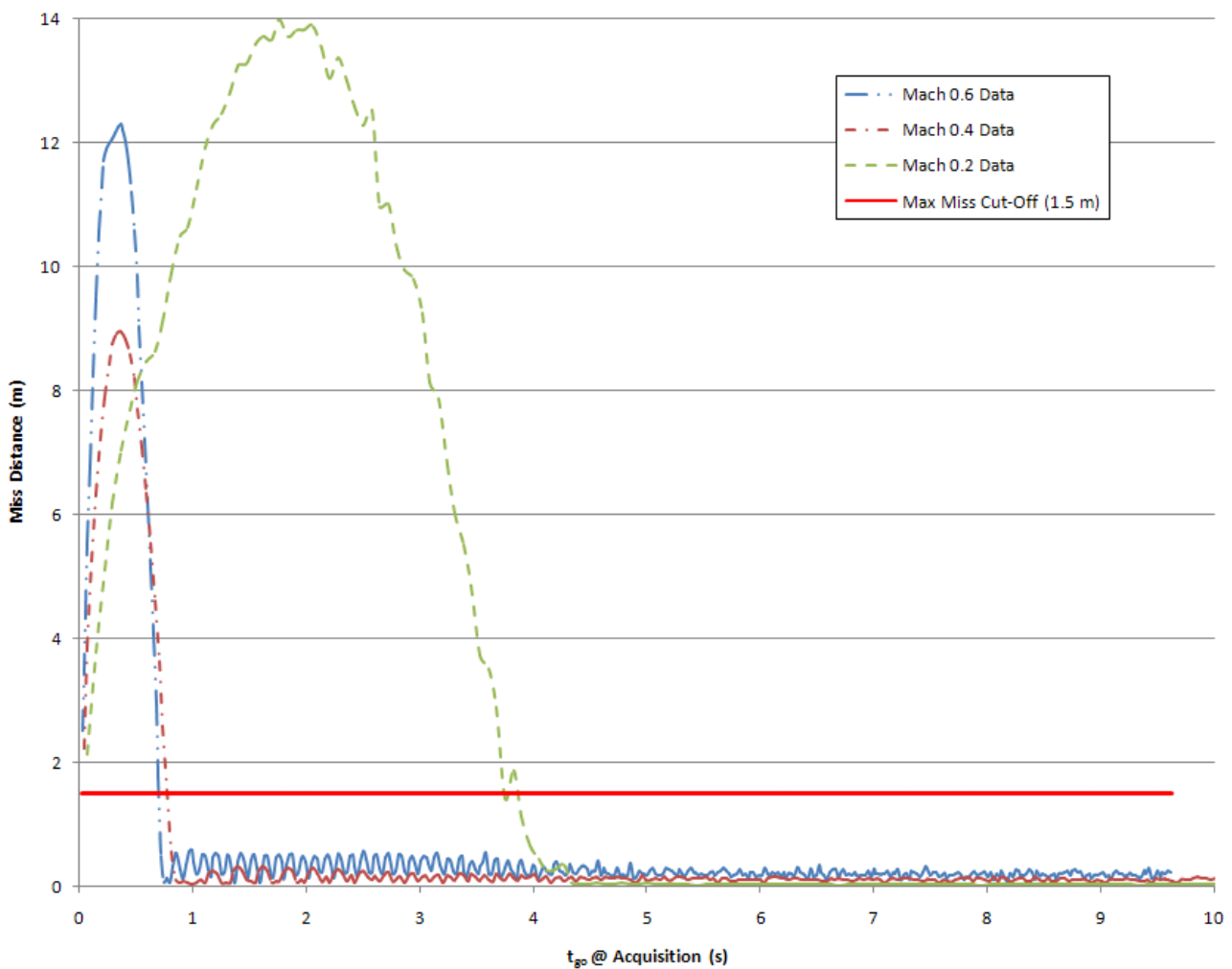
Figure 4.4.2 Estimated Miss Distances For A Given Illumination Time (15° HE assumed)

limiting the illumination time while still achieving the accuracy constraints in a hostile environment. While the plot shows the minimum allowable illumination times for the munition to remain aerodynamically capable of accurately hitting the target, the exact minimum illumination times (and corresponding personnel agreement, or "handshake", times) for the system will be decided only when the exact performance of the IMU is considered in the analysis. This will come once the system hardware choices are finalized in chapter 5.

Human involvment in the final stage of a system's life cycle will often be much larger and more complicated than initially perceived. Modeling this human interaction within the design process and predicting its effects upon system operation is a very fluid, but necessary, undertaking. There are many variables that remain to be addressed that this thesis has not focused upon. Certainly, there remains unmodeled human involvement that will affect the type of system that is selected, but the thesis scenario will suffice with the analysis completed in the previous paragraphs. The guidance system designer must be aware that these factors exist and that they will weigh heavily into the actual system selection in a real-world design.

5   System Selection & Integration

5.1 Overview

The design process is nearly complete. All design factors and corresponding selection criteria have been addressed at some level. The selection of the IR focal plane and the discussion of the design trades for the candidate systems enable the designer to make a well-informed system selection. This chapter focuses on the final system selection, system modeling, and packaged system geometry.

5.2 Final System Selection & Modeling

Figure 4.2.2 exhibits that each of the four candidate systems presents desirable alternatives for the seeker system. However, given that all four satisfy the accuracy constraints and that no single option gives the indication that it will include any undesirable packaging or human integration issues, the author moves forward with option #1 as the final design. With the guidance electronics and, more recently, the API quadrant photodiode array considered static hardware options, the Honeywell HG1930 IMU (figure 5.2.1) offers the lowest anticipated production cost of the alternatives. The HG1930 is specifically designed for use on projectiles, requires little power and is configurable based on user needs. By all accounts, it provides more than sufficient performance for every aspect of the system requirements.

The author modeled a seeker system with the HG1930 as the IMU in chapter 4 and determined the average miss value that the system offers (tables 4.3.2-4.3.4). Now, however, given a finalized system architecture, the designer is able to complete cradle-to-grave simulations for varying target distances and illumination times. The actual simulation remains

Figure 5.2.1 Honeywell HG1930 IMU

limited to the seeker controlled portion of flight, but like the models in chapter 4, the initial conditions at the control handover are dictated by the actual performance of the IMU on board.

The author simulated the three different modeling speeds for the three target ranges with illumination times of 10 s, 5 s, and 1 s. Once again, the simulation was run 200 times to obtain a valid statistical sample set for the miss values. The results of the simulations are listed in tables 5.2.1-5.2.3. Figure 5.2.2 displays a sample flight trajectory for the system as well as the expected ZEM as a function of time for a munition at Mach 0.6 engaging a target at a range of 10 km with an illumination time of 10 s. A histogram illustrating the results of the 200 runs for the same engagement scenario is shown in figure 5.2.3. The figure depicts a very precise guidance system, with no outliers and no significant variation. Because including histograms for all modeling scenarios within the text would be cumbersome, all others are included in Appendix F.

The results demonstrate that the IMU has accuracy to keep the target within the focal plane FOV given a target illumination time of 5 or 10 seconds. With an illumination time of 1 second, however, the IMU is only able to place a Mach 0.4 munition engaging a target at 5 km within an acceptable location to impact the target successfully. All other combinations of munition speed and target range do not place the target within the focal plane's FOV at the handover of control. Thus, the miss distances for those situations are governed solely by the

Speed	Target Distance	HE @ handover	Mean Final Miss (m)	Std Dev (m)	Worst 3σ Miss (m)
M = 0.2	5 km	1.58°	0.0040	0.0376	0.1168
	7.5 km	3.67°	-0.0022	0.0378	0.1156
	10 km	6.68°	-0.0029	0.0367	0.1130
M = 0.4	5 km	0.37°	0.0212	0.1240	0.3932
	7.5 km	0.92°	-0.0050	0.1289	0.3917
	10 km	1.58°	0.0082	0.1244	0.3814
M = 0.6	5 km	0.16°	0.0082	0.1243	0.3811
	7.5 km	0.38°	-0.0114	0.2276	0.6942
	10 km	0.70°	0.0125	0.2362	0.7211

Table 5.2.1 Average Expected Miss – 10 seconds illumination time

Speed	Target Distance	HE @ handover	Mean Final Miss (m)	Std Dev (m)	Worst 3σ Miss (m)
M = 0.2	5 km	3.37°	0.0064	0.0308	0.0988
	7.5 km	7.95°	0.0458	0.0257	0.1229
	10 km	14.72°	0.0437	0.0249	0.1184
M = 0.4	5 km	0.80°	-0.0065	0.1250	0.3815
	7.5 km	2.08°	-0.0239	0.1197	0.3830
	10 km	3.37°	-0.0017	0.1267	0.3818
M = 0.6	5 km	0.40°	-0.0035	0.2380	0.7175
	7.5 km	0.91°	0.0193	0.2488	0.7657
	10 km	1.61°	0.0601	0.2469	0.8008

Table 5.2.2 Average Expected Miss – 5 seconds illumination time

Speed	Target Distance	HE @ handover	Mean Final Miss (m)	Std Dev (m)	Worst 3σ Miss (m)
M = 0.2	5 km	26.91°	IMU - 18.44	N/A	N/A
	7.5 km	64.38°	IMU - 41.31	N/A	N/A
	10 km	87.66°	IMU - 73.27	N/A	N/A
M = 0.4	5 km	5.07°	0.3858	0.0379	0.4995
	7.5 km	45.97°	IMU - 21.21	N/A	N/A
	10 km	26.92°	IMU - 36.89	N/A	N/A
M = 0.6	5 km	37.45°	IMU - 6.61	N/A	N/A
	7.5 km	48.65°	IMU - 14.29	N/A	N/A
	10 km	56.48°	IMU - 24.90	N/A	N/A

Table 5.2.3 Average Expected Miss – 1 second illumination time
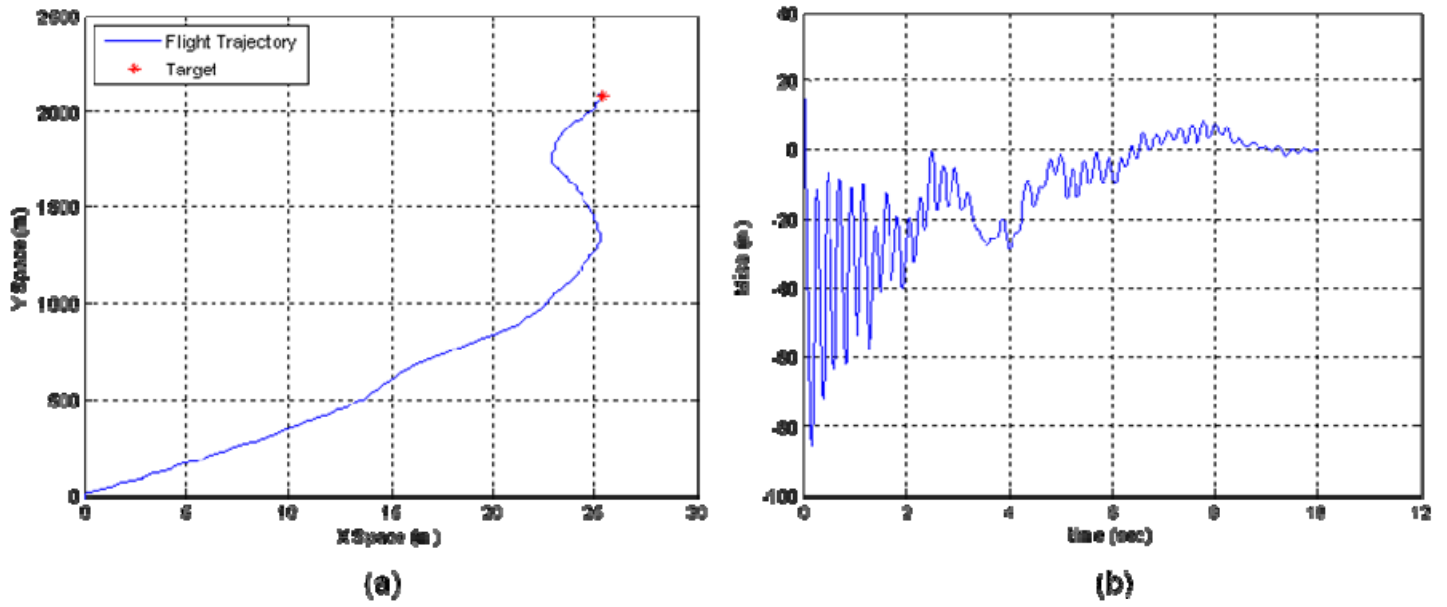
Figure 5.2.2 Mach 0.6, 10 km target, 10 s illumination: (a) Flight trajectory, (b) ZEM over time
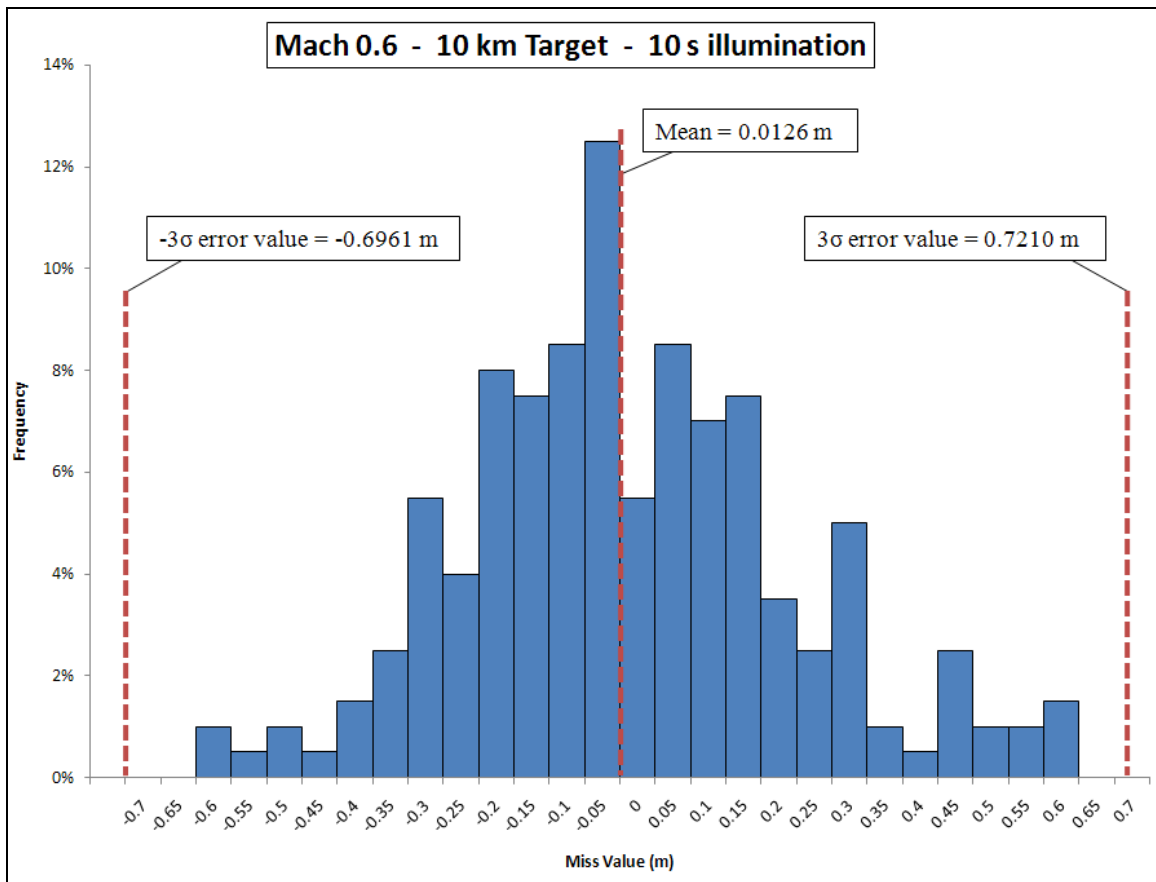

Figure 5.2.3 Histogram of Sample System Simulation Results

accuracy of the IMU (as indicated in table 5.2.3). As such, the illumination time must be greater than 1 second for the majority of applications of the designed system.

In industry, when conducting an analysis of statistical results like those listed above, it is important to outline a measure of quality control to ensure the endeavor performs up to some industry-wide standard. This measure generally comes in the form of a process capability index denoted C_{pk} [40]. In the design process, the results of any modeled system should be subjected to this type of quality check to ensure the results are acceptable. Basically, C_{pk} is a measure of how well the distribution of statistical results is centered on the desirable outcome. In this case, one would think of the C_{pk} as the measure of how well the miss distance values are centered on a mean of 0.0 m. For the specific analysis conducted in this thesis, the value of C_{pk} is calculated as:

$$C_{pk} = \frac{CEP - \mu}{3\sigma}$$

(5.2.1)

where the CEP is 1.5 m, μ is the mean miss distance, and σ is the standard deviation of the miss results. Generally, engineers desire a C_{pk} value of 1.67 to ensure that the results are acceptable for a double sided, unproven process such as the thesis scenario [40]. The worst-case situation for the system simulation results yields a C_{pk} value of 1.944. Given this value, the author is satisfied with the results of the statistical analysis.

The analysis above, while enlightening, leaves the exact value of the minimum illumination time required for each engagement scenario unresolved. The guidance system designer must not overlook this critical aspect of the system analysis. It is of extreme importance for the safety of the designating personnel and for the adequate communication among all personnel involved in an engagement. Only once this value is resolved can the designer move forward in the design process.

Figure 4.4.2 shows the minimum illumination times for the munition to remain *aerodynamically* capable to hit the target with an acceptable miss value with an initial heading error of 15°. However, the tables above have shown that with an accurate IMU, less than 15° of heading error will accumulate during flight and less aerodynamic capability is necessary than suggested in figure 4.4.2. Therefore, the combination of the two factors (aerodynamic

maneuverability & IMU accuracy) dictates the true minimum illumination time allowable for each projectile to impact the target with less than 1.5 m error.

Combining and comparing the two factors, the author found the minimum illumination times for each modeling speed and target range. These time values allow the IMU to place the target within the FOV at the control handover while still giving the projectile enough time to make the necessary course corrections. The specific values are listed in table 5.2.4.

Speed	Target Distance	Minimum Illumination Time	Maximum "Handshake" Time	Remarks
M = 0.2	5 km	3.75 s	69.78 s	Aerodynamically Limited
	7.5 km	3.75 s	106.55 s	
	10 km	4.92 s	142.13 s	IMU Limited
M = 0.4	5 km	0.81 s	35.95 s	Aerodynamically Limited
	7.5 km	1.41 s	53.74 s	IMU Limted
	10 km	1.47 s	72.06 s	
M = 0.6	5 km	1.07 s	22.97 s	IMU Limited
	7.5 km	1.18 s	34.88 s	
	10 km	1.35 s	46.73 s	

Table 5.2.4 Min Illumination and Max "Handshake" Times for 1.5 m CEP

The table also includes the maximum time allowable for the launching personnel to communicate all necessary information to the designating personnel, or the time allowable from launch for the handshake to be made between the two parties. Specifically, it is the minimum illumination time subtracted from the total flight time of the projectile. If the agreement is delayed longer than the time values listed in table 5.2.4, there is mission failure.

Based on the technical analysis completed and the hardware technology surveyed, the selected seeker system seems to meet all cost and accuracy constraints. While the technology surveys revealed expected hardware pricing information for the IMU and IR focal plane, the approximate cost for the guidance electronics has yet to be obtained.

The cost of the guidance electronics will likely be dominated by the most important piece of hardware, the digital signal microprocessor. Reference [41] describes a guided system that successfully implemented a Texas Instruments (TI) 40 MHz microprocessor on its particular platform. Thus, it is reasonable to expect that a similar processor will handle the signal

processing needs of the system under investigation quite sufficiently. A TI distributor website lists the price of a 500 MHz microprocessor unit at $95 [42]. The unit also publishes an acceptable operating temperature range of -45° C to 90° C. Estimating the cost of the guidance breadboard and other integrating electronics, the author approximates the total cost of the guidance control electronics package at conservative value of $200.

To be thorough, the author also includes a price estimate for the control actuation system (CAS). The price of the CAS will not be included in the estimate of the overall system because the author is interested only in the seeker head components that will relay information to the controls for the required course correction. Nevertheless, because the seeker system directly interfaces with the CAS, it is a beneficial inclusion. A survey of rotary servomotors offered by the General Dynamics-Versatron, based in Healdsburg, CA, used for the control surface actuation systems of tactical missile systems currently utilized by the U.S. military estimate notional unit prices of roughly $4,000-$6,000. This price estimate includes the cost not only of hardware, but also quality verification, design engineering, etc. The actual price of the actuation system will vary based on end user requirements, but this estimate serves as an acceptable starting point.

While there will be some slight cost and performance variance from one manufacturer to another regarding the guidance electronics, the estimate in the above paragraph is sufficient for the purpose of estimating the total system cost. Table 5.2.1 concisely lists the approximated costs of each of the pertinent hardware components/subsystems that comprise the total system architecture. The results indicate that the endeavor to create a low-cost, accurate seeker system from off-the-shelf components remains both feasible and practical.

Component	Cost	Remarks
API Quad Si Photodiode Array	$210.00	Model SD 380-23-21-051
Honeywell IMU	$3,500.00	Model HG1930
Flight Computer	$200.00	TI Model TMS32C6414EGLZ5E0
Total Hardware Price Estimate	$3,910.00	

Table 5.2.1 Hardware Component Costs for Selected Seeker System

5.3 Design, Integration & Packaging

The remaining issues of hardware integration and packaging also heavily affect the success of the system design. In addition to the complexities of ensuring all that components can be integrated and amassed into a single unit small enough to fit within tactical projectile casings, the production and assembly adds to the system cost for the end user. In fact, it is highly likely that the ongoing production (packaging and assembly) costs will affect the final price tag more heavily than the actual system hardware. This subsection addresses challenging design issues and the influence on system cost of the integration and assembly process.

The continual packaging and assembly costs that are seen by the end user are not to be confused with the one-time system design and verification costs of the unit. The author will not attempt to speculate upon the actual estimates of design and verification costs because the integration of the physical components into a single unit design will likely prove to be an iterative process. Moreover, in the business sector, the iterative design process is part of an engineering and development contract that does not affect the price seen by the end user. Therefore, the author will address the one-time packaging issues from a broader, strategic design perspective.

The thesis attempts to propose a design methodology for a generic tactical munition platform that will be easily transferrable to alternative, but similar, tactical units. Although a single design can be proposed for a single platform, the final system design will surely require a slightly different geometry for other platforms (mortar, artillery, RPG). Nevertheless, the author proposes a specific design arrangement for the notional projectile used throughout the thesis analysis. Figure 5.3.1 depicts the proposed hardware arrangement within the munition housing.

The 1" diameter lens that focuses the incoming EM flux onto the IR focal plane is situated at the front of the hemispherical nose of the munition. The focal plane is placed one focal length (1") directly behind the lens in order to collect the incoming flux most efficiently. Directly behind the quad cell detector, the IMU is aligned so that its inertial axes align with the local body axes of the munition. The correct orientation of the IMU ensures that the position estimation is as accurate as possible. In addition to the aforementioned seeker system components, the author has included the munition payload, control system servomotors, rocket motor assembly, and representative guidance electronics to illustrate how each component fits within a tactical munition casing.
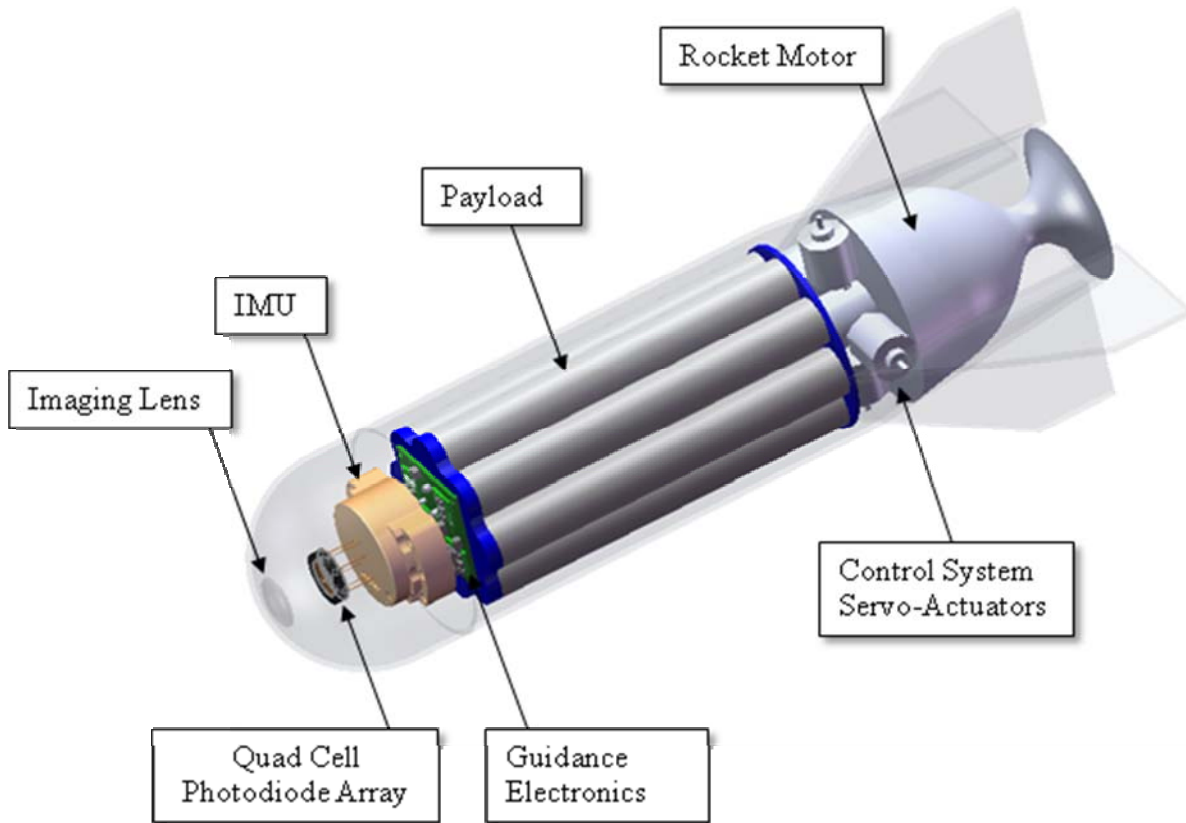
Figure 5.3.1 Proposed Seeker System Configuration - CAD Cartoon

Naturally, the proposed design is one of many acceptable geometric arrangements, and further hands-on analysis is required to determine the optimal configuration. In particular, the designer requires knowledge of the actual mass, center of mass location, and moment of inertia about the main missile axis for accurate dynamic modeling. The configuration will also require rigorous field testing to ensure that it has the ability to withstand the expected wear caused by the dynamic flight environment.

While the design of the physical system architecture is the paramount step in the design process of the seeker system, the end user is more interested in the price and accurate performance of the unit. Thus, it is of extreme benefit to determine a final system price estimate for the designated user. The cost of the system hardware represents only a portion of the unit price of the system. In commercial business, the final unit price must support all aspects of the munition design life cycle. It must include the overhead required for the assembly, packaging,

and testing of the unit in production, recovery of design and facilities costs, company profit, and even the costs of shipping unit quantities to the customer. With all the additional costs, the final unit pricing is undoubtedly much higher than the $3,910 estimated for the system hardware.

The price evolution for the seeker system is expected to follow the pattern displayed by most market merchandise. This pattern is exponentially decaying, with the first single unit being very expensive, but retaining a steady-state, bulk production price that is significantly less. In most cases, a rule of thumb generally places the steady-state market price at roughly three to five times the cost of the hardware making up the system. This overhead accounts for all additional costs described in the previous paragraph. Assuming this relationship holds true, the expected steady-state price of the seeker system will be in the range of $11,730 - $19,550, placing the proposed configuration in the range of the price ceiling specified for the system. Note that the production cost of the IMU will likely fall in the foreseeable future (perhaps to $2K), rendering the latter number of the estimate above as an extreme upper bound for the unit price of the system.

The actual guidance system component (IR focal plane, IMU) costs demonstrate the validity of low-cost components for precision guidance applications. So, despite the possibility of the price estimate landing above the initial target of $15,000, the study demonstrates that the designing and marketing a low-cost guidance system from COTS components presents a very attractive business opportunity.

6 Conclusions and Suggestions for Future Work

6.1 Conclusions

The goal of this research was to develop a seeker system design methodology to be applied to the specific mission of creating a sufficiently accurate system from COTS components at low cost. From a strategic viewpoint, this thesis demonstrated a successful cradle-to-grave design methodology for a specific type of seeker system. The approach formulated by the author successfully applied design and analysis techniques to achieve a specified set of design constraints and requirements. Despite being aimed specifically at developing a strap-down seeker assembly for guiding tactical munitions employed in short-range, rapid-response situations, the design and analysis elements comprising the methodology have the capability to be applied to other systems with a similar mission design space.

Furthermore, through the evaluation of the design space trade-offs, the thesis analysis demonstrated that it is both realistic and practical to develop a precision guidance seeker system from COTS components for less than $15,000. The approximated production level system cost of $11,730 - $19,550 presents an attractive system to be applied for scenarios that do not demand systems with high dynamic bandwidth. Certainly, as the technology continues to mature, component and assembly costs will fall. This trend will swing the cost vs. benefit analysis, likely unfavorable to guided munitions beforehand, in favor of utilizing this type of guided system for many situations. Given the demonstrated success of the guided systems in use today, this is a very attractive opportunity for all branches of the U.S. military.

The methodology presented in the thesis is also of particular utility from a more broad perspective. As the capability of today's technology continues to expand, it is inevitable that precision guidance will continue to be applied to smaller and smaller platforms. This

development is going to amplify the need for (and development of) compact, accurate, seeker-enabled guidance systems. The market niche for these systems will require that system cost be a paramount design trade element, but also that all design trade elements are taken into consideration. This thesis provides a roadmap for a system designer that includes these vital characteristics. It allows the engineer to develop the technology requirements while still addressing the system dynamics issues that remain so important.

6.2 Suggestions for Future Work

The thesis analysis presented a very basic investigation into seeker system technology and the market that encompasses it. The author made many simplifying assumptions to allow the study to be completed without extending the original scope of the thesis. As such, the opportunity for follow-on research is plentiful. Furthermore, the amount of future work opportunities will likely go hand-in-hand with the military's necessity of improved guidance system technology. As the employment of guidance systems expands within the military's arsenal to platforms never before considered, there will emerge the need for further research in a wide array of fields. For now, however, the author focuses on several subsequent research opportunities directly related to the thesis study.

The first area that presents opportunity relates to the target characteristics. While this thesis considered the benign situation of static targets, the existence of transient, or highly dynamic, targets remains of perhaps more importance to the military. For this reason, it would be beneficial to expand the mission to include active targets. This study would include the addition of dynamic capability to the MEMS focal plane. The author suggests three possible avenues to allow for higher optical bandwidth: (a) the inclusion of MEMS gimbals to allow the entire "optical" assembly to rotate within the munition head, (b) using optical beam steering by means of multi-axis micro-mirrors that direct in the incoming signal to certain areas of the focal plane, and (c) implementing a phased focal plane array to increase the effective FOV of the system as close as possible to 180°. The inclusion of these factors will serve to improve the capability of the system as a whole and would make the system much more attractive to the end-user.

This thesis is intended to present a systems analysis of the seeker system, so many of the individual tenets could possibly serve as stand-alone projects. One specific area lies in the dynamic modeling of the system. The 2-D simulation developed by the author was of particular utility for giving rough approximations to the munition's flight behavior in a dynamic environment, but needless to say, many simplifying assumptions were made and an entire degree of freedom (altitude, or z-space) was ignored. For adequate proof of concept, any system will require 6-DOF modeling capability (x, y, z, pitch, yaw, & roll). This type of modeling, including precise atmospheric effects, allows the designer to obtain miss distance estimates with a great degree of confidence. Once detailed dynamic modeling is addressed and performance is verified, then the prototyping and testing become viable options.

The projectile geometry designed in this thesis was intended to easily relate to many tactical munitions currently in use. While the author's notional projectile satisfied that intention, it is not an exact replication of any real-world munition. The opportunity to identify an actual system in need of precision guidance and apply the methodology to that platform is one that should be explored in depth down the road. Using the analyses presented in this thesis one may be able to create a marketable seeker system to be employed one of the military's many platforms that would be improved by the addition of precision guidance capability.

Finally, the author reiterates that the human involvement in the target engagement process is extremely important. The assumption that all pertinent communication is complete within 1 to 2 minutes from call-for-fire is unrealistic. In a situation like the thesis scenario, it is more likely that the limiting factor is not the hardware technology, but the human delays and mistakes that inevitably take place. A difference in military doctrine from one service branch to another is just one example of a sticking point that affects the speed and efficiency of executing the mission outlined in this thesis. Two recent theses from MIT address this issue by analyzing Air Operations Center activities, where many decisions are made and time delays occur [43, 44]. A more broad study outlining the interaction between the limitations of technology performance and strategic human involvement would address the important issue that the author has omitted for this technological analysis.

[This Page Intentionally Left Blank]

Appendix A – MATLAB Script for IMU Drift Calculation

```matlab
%%%%%%%%%%%%%%%%%%%%%%%%%%%%%%%%%%%%%%%%%%%%%%%%%%%%%%%%%%%%%%%%%%%%%%%%%%%%
% 2 Lt Brian Nagle, USAF
% Draper Laboratory Fellow, MIT Dept. of Mechanical Engineering
% Master's degree candidate
% 14 January 2008
%%%%%%%%%%%%%%%%%%%%%%%%%%%%%%%%%%%%%%%%%%%%%%%%%%%%%%%%%%%%%%%%%%%%%%%%%%%%


% This m.file estimates the spatial error caused by IMU drift in a tactical
% munition for a prescribed amount of flight time.  The user must know the
% drift specifications of the IMU in order to run the loop.  The loop
% assumes that all IMU error is propagating in one direction (worst case)
% and that the munition is unaffected by wind and/or atmospheric
% turbulence.  The goal of the model is to find the highest allowable IMU
% error (d) that will keep the final angular error (angerror) below 15
% degrees.

% Defining parameters
% v - munition velocity in m/s
% d - IMU drift spec in deg/s
% e - IMU drift spec in rad/s
% tf - anticipated flight time of munition in sec

% Travel Distances in 60 sec for analyzed speeds:
d2 = 4080;  % mach 0.2 - 68 m/s --> 4.08 km
d4 = 8160;  % mach 0.4 - 136 m/s --> 8.16 km
d6 = 12480; % mach 0.6 - 208 m/s --> 12.48 km


v = 136;
d = 0.0056;
tf = 50;
error = 0;        % initiate the error value at launch
conv = pi/180;    % define conversion from degrees to radians
e = d*conv;       % convert from degrees to radians

% Calculate the spatial error caused by the IMU drift
for i = 1:tf;
    error = error + v*sin(e*i);
end

dist = v*tf;  % distance from target along the original course
eps = e*tf;   % final angular orientation of munition

if v == 68;
    dgo = d2-dist;
elseif v == 136;
    dgo = d4-dist;
else
    dgo = d6-dist;
end


nu = atan(error/dgo); % angular error due to propagated spatial error
```

```matlab
angerror = (eps + nu)/conv % display total angular error in command window

if angerror > 15
    disp('error exceeds focal plane FOV, mission failure');
else
    disp('error within specified tolerance');
end
```

Appendix B – Full IMU Specification Table

System	Volume (in³)	Mass (lbs)	Approx Cost ($K)	Gyro Bias (°/hr) 1σ	Accel Bias (milli-g) 1σ	Random Walk (°/rt-hr)	Scale Factor (ppm)	Dynamic Range (deg/s)	Remarks
Honeywell HG1930	4	0.35	3.5	20	4	0.15 (deg/hr)	300	1440	High G tested
Honeywell HG1700AG	33	1.6		1	1	0.125	150	1000	RLG
AIS SiIMU02	7.3	0.463	4.5	6.5	0.5	0.5	500	500 (2&3) 9000 (1)	High G tested - Silicon Sensing
AIS SiIMU04	10.35	0.5512	4.5	8	3	0.5	3000	150 (2&3) 600 (1)	Marketed by Silicon Sensing
Xbow IMU440CA	28.125	1.3	2	7200	15	4.5	10000	200	MEMS design
Xbow IMU700CB	120	3.5	11.5	20	12	0.4	20000	200	FOG, Si Accelerometers
MEMSense μIMU	5.53	0.0294	2.5	2016	2.1	n/a	n/a	600	
Systron MMQ 50 IMU	9	0.5	5	50-200	2.5	0.3	5000	200	Single unit price (think about QDARS)
Xsens Mti	4.52	0.1102	3	18000	2.04	60		300	
Litton LN200	32	1.54	30	10	1000	n/a	n/a	n/a	FOG, MEMS Si Accelerometers
Draper MMIMU	8	0.62	30	10	3000	n/a	n/a	n/a	MEMS, non-production design
Micro-Aerospace MASIMU01	7.7	0.1764	4	60	n/a	n/a	n/a	150	Utilizes Analog Devices Gyros

# Appendix C – Missile DATCOM Fortran Input File

```
DIM IN
 $FLTCON NALPHA=15.,NMACH=1.,MACH=0.4,REN=3000000.,
        ALPHA=-28.,-24.,-20.,-16.,
     ALPHA(5)=-12.,-8.,-4.,0.,
     ALPHA(9)=4.,8.,12.,16.,
        ALPHA(13)=20.,24.,28.,$
 $REFQ XCG=8.0,$
 $AXIBOD TNOSE=OGIVE,LNOSE=3.,DNOSE=4.,LCENTR=8.,DCENTR=4.,TAFT=CONE,
        LAFT=5.0,DAFT=3.,DEXIT=2.,$
 $AXIBOD BASE=.TRUE.,BETAN=10.,JMACH=2.5,PRAT=4.,TRAT=4.,$
 $FINSET1 XLE=12.,NPANEL=4.,PHIF=0.,90.,180.,270.,SWEEP=35.3,STA=0.,
     CHORD=5.,1.,SSPAN=1.75,4.5,CFOC=0.3,1.,$
 $DEFLCT DELTA1 = 5., DELTA3 = 5.,$
DERIV RAD
PART
PRINT AERO BODY
DAMP
PLOT
SAVE
NEXT CASE
```

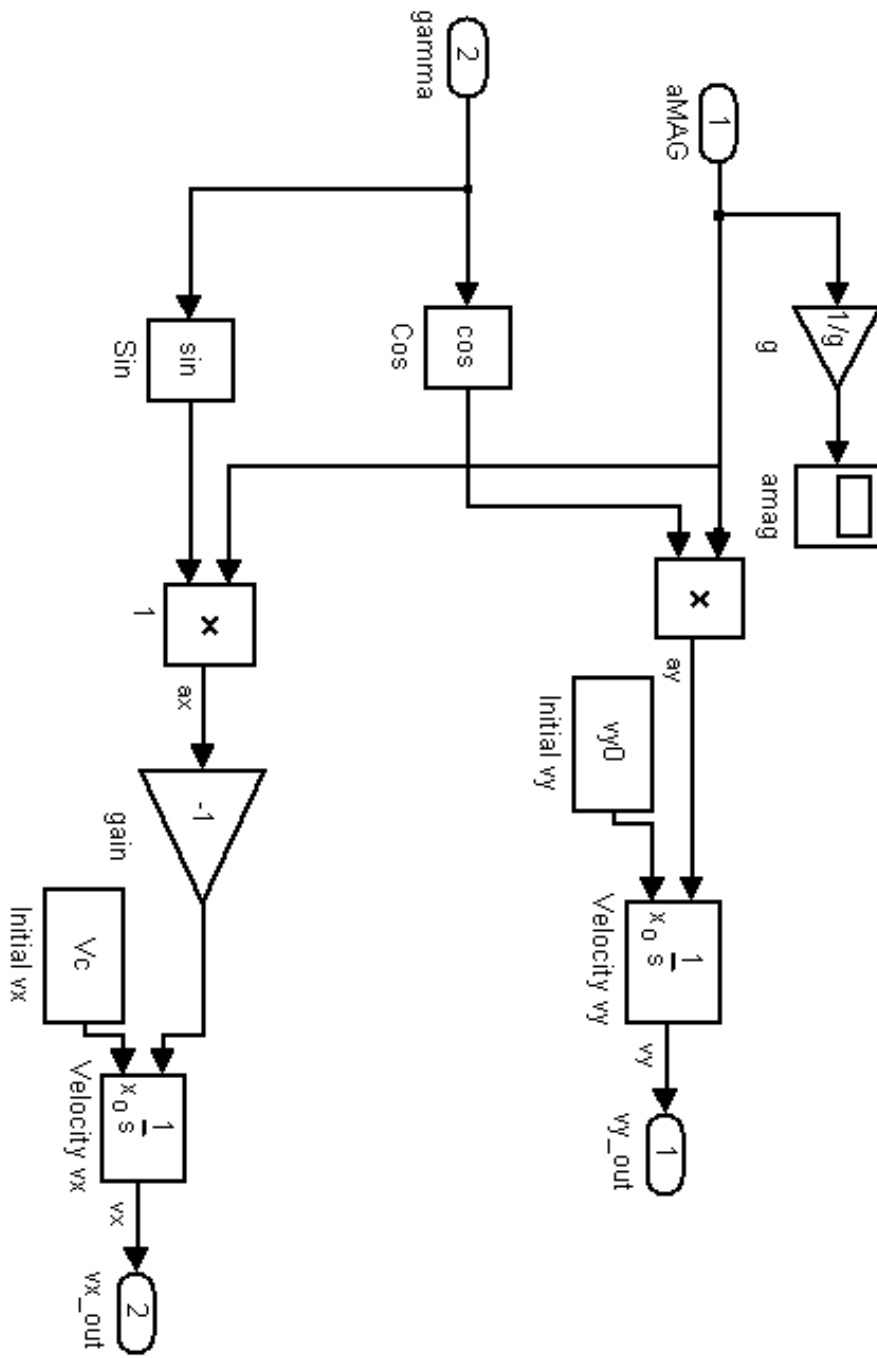# Appendix D – Flight Simulation Model Block Diagrams & Scripts
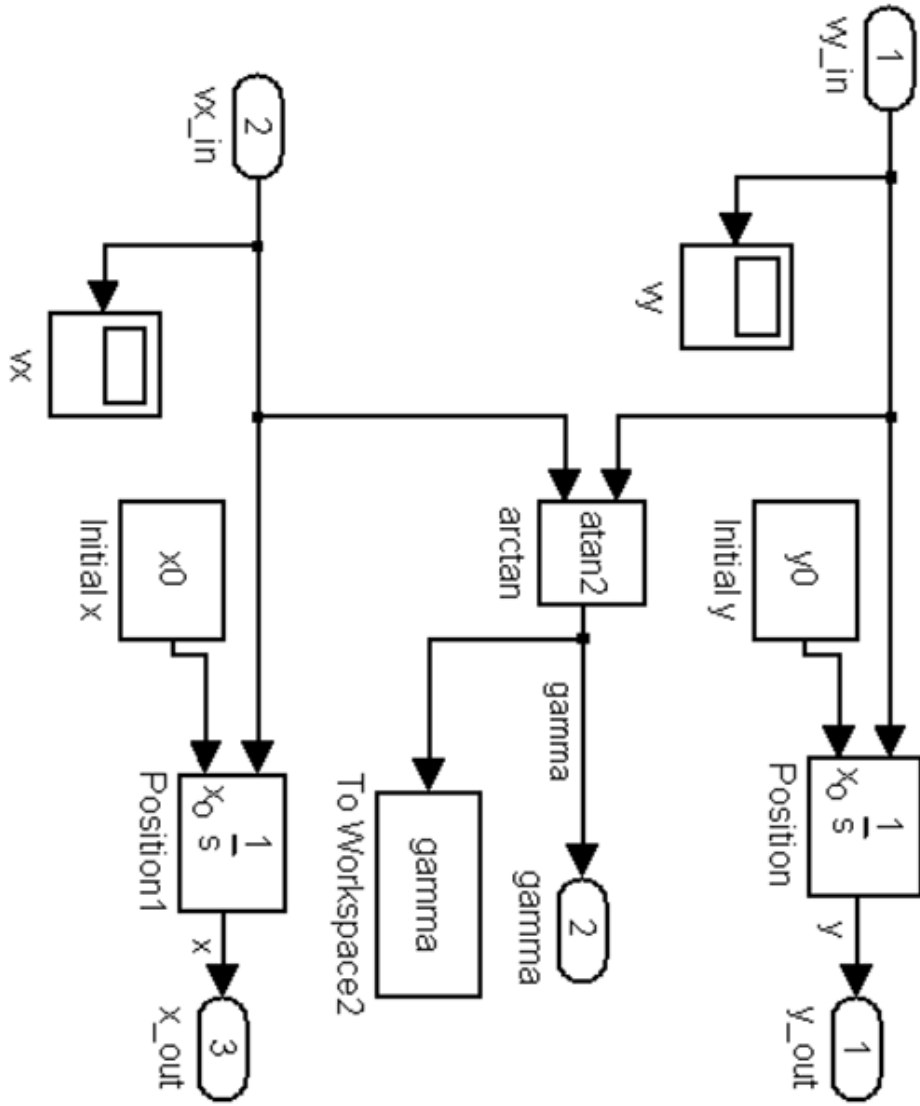
Complete Guidance Loop Block Diagram
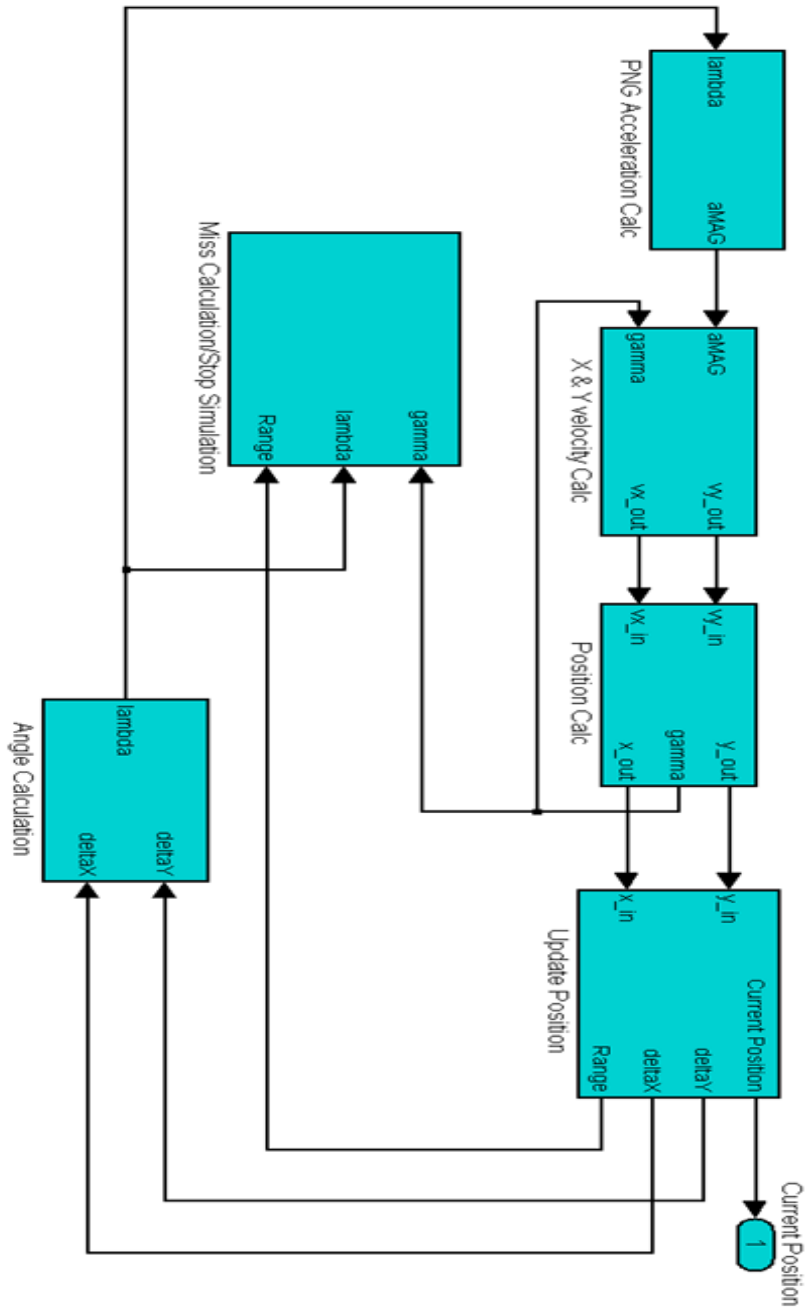
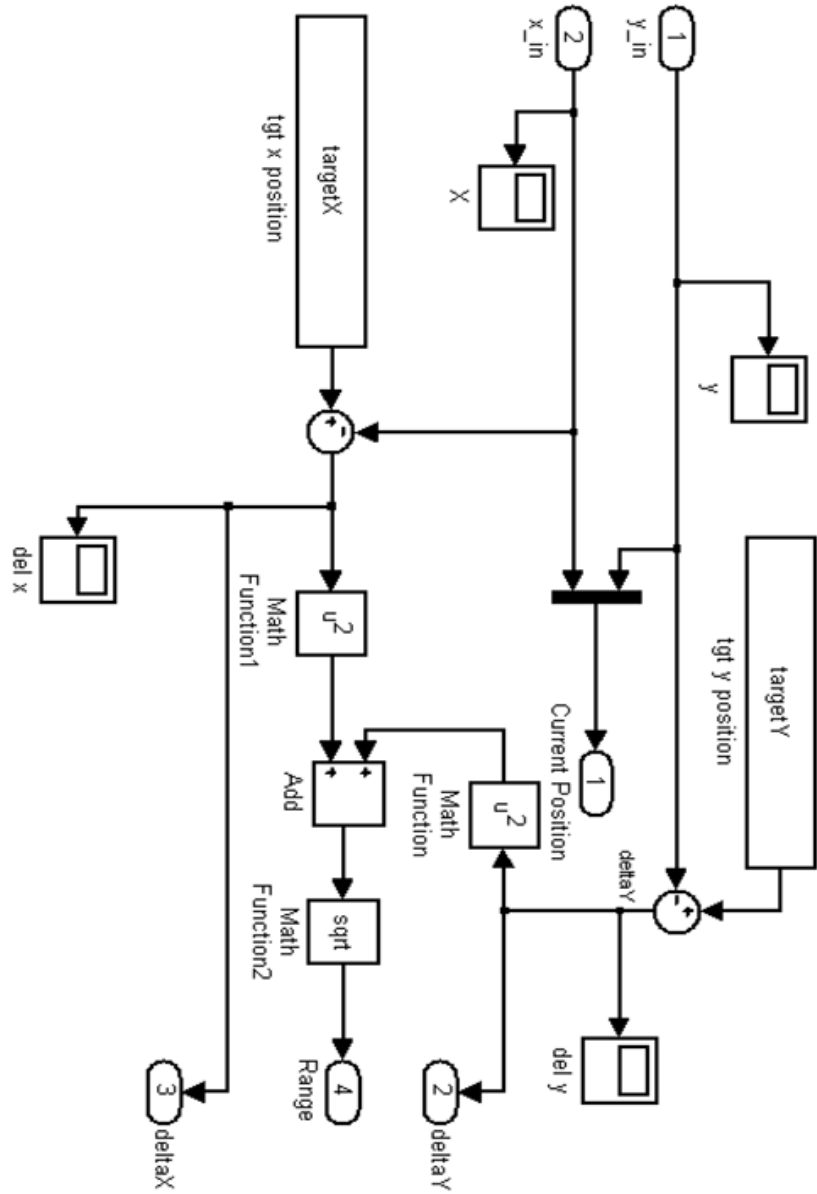# Proportional Navigation Guidance Acceleration Calculation
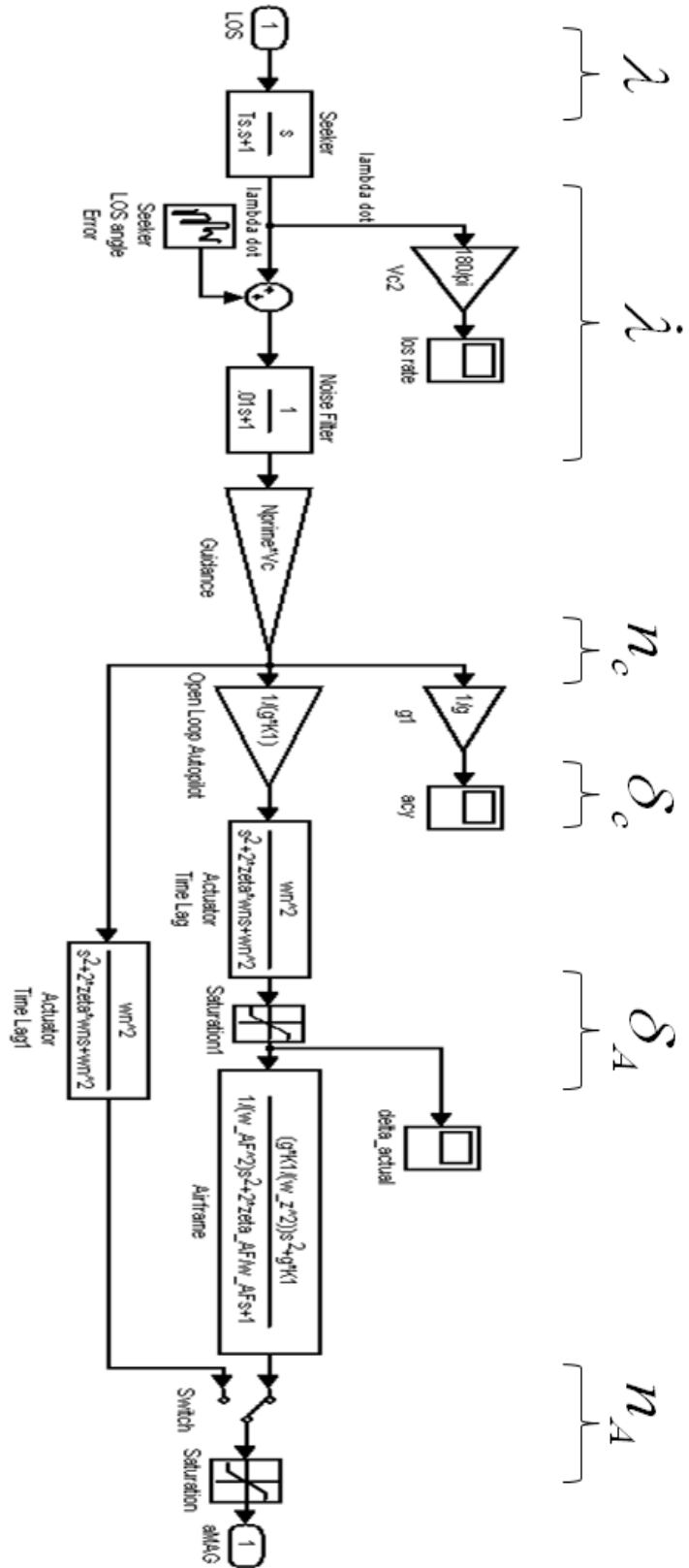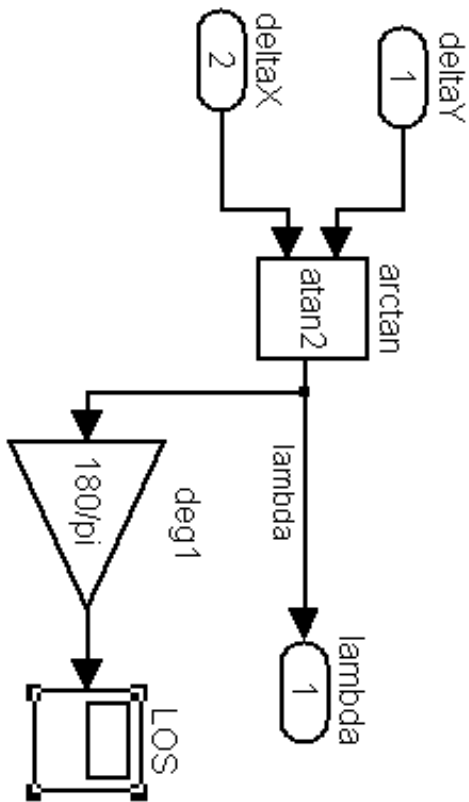
X & Y Velocity Calculation
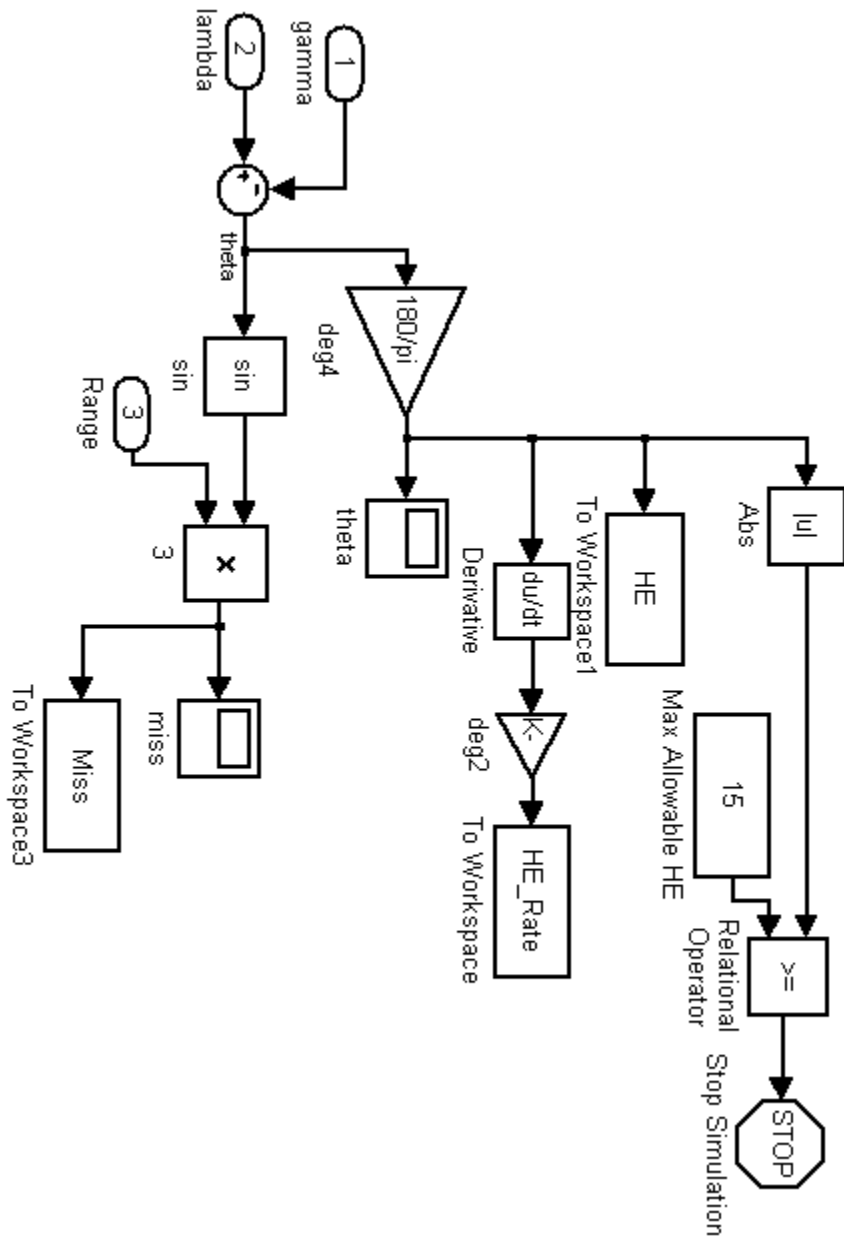
X & Y Position Calculation

Position Update Calculation

Line-of-Sight Angle Calculation

Miss Calculation/Stop Simulation

Flight Simulation Model Initialization – MATLAB Script

```matlab
%%%%%%%%%%%%%%%%%%%%%%%%%%%%%%%%%%%%%%%%%%%%%%%%%%%%%%%%%%%%%%%%%%%%%
% 2 Lt Brian Nagle, USAF
% Draper Laboratory Fellow, MIT Dept. of Mechanical Engineering
% Master's degree candidate
% November 2007
%%%%%%%%%%%%%%%%%%%%%%%%%%%%%%%%%%%%%%%%%%%%%%%%%%%%%%%%%%%%%%%%%%%%%


% Define parameters to be input into simulink model Missile_1DOF_v2:

% All parameters herein are further defined in "Tactical and Stategic
% Missile Guidance", by Paul Zarchan, Chapters 2 and 22.


% Constants

Nprime = 3.5;                        % Proportional Guidance Constant
Vc = 136;                            % Missile Speed, or Closing Velocity
theta_init = 0.3195*(pi/180);        % Initial heading error angle
vy0 = 0;                             % Initial velocity in y-direction
zeta = 0.707;                        % Control System Damping Ratio
wn = 10*2*pi;                        % Control System Natural Frequency
%n = 1;                              % dummy constant
Ts = 0.001;                          % Seeker system time constant
if Vc == 208;                        % Maximum Lateral acceleration (m/s^2)
    nl_sat = 193.3;
elseif Vc ==136;
    nl_sat = 86.25;
else
    nl_sat = 21.52;
end
g = 9.81;                            % Acceleration due to gravity
targetX = 1500;                      % Initial target position in x direction
x0 = 0;                              % Initial x position in domain - Assume
                                     initial position is at origin
y0 = 0;                              % Initial y position in domain - Assume
                                     initial position is at origin
targetY = tan(theta_init)*targetX;   % Initial y separation

% Airframe Geometry
IM = 0.0254;                         % Conversion factor from in to m
RD = pi/180;                         % Conversion factor from rad to deg
d = 4.5*IM;                          % Missile diameter
Ctt = 1.5*IM;                        % Length of tail edge
Crt = 5*IM;                          % Length of tail root
ht = 2.5*IM;                         % Width of tail
L = 16*IM;                           % Missile length
Xcg = 8*IM;                          % CG location
Ln = 3*IM;                           % Nose length
An = 0.67*Ln*d;                      % Nose area
Ab = (L-Ln)*d;                       % Body area
Xhl = 13*IM;                         % Length to control surface hinge line
```

```matlab
W = 9*g;                                % Weight of missile in Newtons
Iyy = W*L^2/(12*g);                     % Missile moment of inertia


mach = 0.6;                             % Missile speed in mach
Vm = mach*340;                          % Conversion to m/s
alpha = 24*RD;                          % AOA at 24 deg
delta = 25*RD;                          % Delta at 25 deg
rho = 1.225;                            % Air density in kg/m^3


Sref = (pi*d^2)/4;                      % Reference area
beta = sqrt(1-mach^2);                  % Normalized speed for subsonic travel
St = 0.5*ht*(Ctt+Crt);                  % Tail Area
Splan = L*d;                            % Approximated planform area
Xcpn = 0.67*Ln;                         % Nose center of pressure
Xcpb = (0.67*An*Ln+Ab*(Ln+0.5*(L-Ln)))/(An+Ab);  % Body center of pressure
Q = 0.5*rho*Vm^2;                       % Dynamic Pressure


% Aero Coefficients
Cn_delta = 8*St/(beta*Sref);                        % Cn delta
Cn_alpha = 2+(1.5*Splan*alpha)/Sref+8*St/(beta*Sref);  % Cn alpha
Cm_delta = (8*St/(beta*Sref))*(Xcg-Xhl)/d;          % Cm delta
Cm_alpha = 2*(Xcg-Xcpn)/d+((1.5*Splan*alpha)/Sref)*((Xcg-Xcpb)/d)+ ...
    (8*St/(beta*Sref))*(Xcg-Xhl)/d;                 % Cm alpha


M_alpha = Q*Sref*d*Cm_alpha/Iyy;        %
M_delta = Q*Sref*d*Cm_delta/Iyy;        %
Z_alpha = -g*Q*Sref*Cn_alpha/(W*Vm);    %
Z_delta = -g*Q*Sref*Cn_delta/(W*Vm);    %



% Airframe Transfer Function Parameters
% Aerodynamic Acceleration Gain
K1 = -Vm*(M_alpha*Z_delta-Z_alpha*M_delta)/(g*1/RD*M_alpha);
% Aiframe zero
w_z = sqrt((M_alpha*Z_delta-Z_alpha*M_delta)/Z_delta);
% Airframe Natural Frequency
w_AF = sqrt(-M_alpha);
% Airframe Damping
zeta_AF = Z_alpha*w_AF/(2*M_alpha);
```

Flight Simulation Model Plotting - MATLAB Script

```matlab
%%%%%%%%%%%%%%%%%%%%%%%%%%%%%%%%%%%%%%%%%%%%%%%%%%%%%%%%%%%%%%%%%%%%
% 2 Lt Brian Nagle, USAF
% Draper Laboratory Fellow, MIT Dept. of Mechanical Engineering
% Master's degree candidate
% November 2007
%%%%%%%%%%%%%%%%%%%%%%%%%%%%%%%%%%%%%%%%%%%%%%%%%%%%%%%%%%%%%%%%%%%%

% This m.file plots the trajectory of the munition along its flight path to
% the target in figure 1, and plots the heading error value vs time in
% figure 2.  It also determines and displays the final miss value as
% "miss_real".

function plots2(yout,targetY,targetX,tout,HE,Miss)

figure(1)
plot(yout(:,1),yout(:,2),targetY,targetX,'r*');
grid
legend('Flight Trajectory', 'Target',2);
xlabel('X Space (m)');
ylabel('Y Space (m)');

figure(2)
plot(tout,HE,'b')
legend('Heading Error (Theta)',2);
xlabel('time (sec)');
ylabel('degrees');
ylim([-10 25]);


miss_real = abs(Miss(length(Miss)));

miss_real
```

Appendix E – Derivation of Airframe Transfer Function

E.1 Overview

      The method for deriving the airframe transfer function utilized in the flight simulation package of Section 3.4 is developed in <u>Tactical and Strategic Missile Guidance, 5th Ed.</u>, by Paul Zarchan. The text demonstrates the creation of an airframe transfer function for any generic geometry in great detail. This appendix is merely an abbreviated synopsis of the method and details the derivation only for the geometry considered in the thesis.

      The approach taken by Zarchan is the exact same as that used in Missile DATCOM, or the component build-up method. This method seeks to determine how the airframe is affected by the body, wings, tail, etc and then sum their individual contributions to obtain the overall force and moment coefficients. We will begin by expressing the approximations for the normal force and moment coefficients as the sum of the individual component contributions:

$$C_N = 2\alpha + \frac{1.5 S_{plan}\alpha^2}{S_{ref}} + \frac{8 S_T(\alpha+\delta)}{\beta S_{ref}} \tag{E.1}$$

$$C_M = 2\alpha\frac{(X_{CG}-X_{CPN})}{d} + \frac{1.5 S_{plan}\alpha^2}{S_{ref}}\frac{(X_{CG}-X_{CPB})}{d} + \frac{8 S_T(\alpha+\delta)}{\beta S_{ref}}\frac{(X_{CG}-X_{HL})}{d} \tag{E.2}$$

In the above equations, the first, second and third terms correspond to the contributions from the nose, body, and tail, respectively. Table E.1 provides a concise description of each term in the two formulas.

      Assuming that each equation is linear in angle of attack and fin deflection, we are able to express the normal force and moment coefficients as:

$$C_N = C_{N_\alpha}\alpha + C_{N_\delta}\delta \tag{E.3}$$

$$C_M = C_{M_\alpha}\alpha + C_{M_\delta}\delta \tag{E.4}$$

From these expressions, we are able to obtain a transfer function from the input control surface deflection to the lateral acceleration of the airframe. The following paragraphs will derive these equations for the geometry and boundary conditions considered by this thesis.

α	Angle of Attack
δ	Control Surface Deflection Angle
X_{CG}	Center of Gravity Location
X_{CPN}	Nose Center of Pressure Location
X_{CPB}	Body Center of Pressure Location
X_{HL}	Control Surface Hinge Line Location
S_{plan}	Planform Area
S_{ref}	Reference Area
S_T	Tail (Control Fin) Area
d	Body Diamater

Table E.1 Descriptors of Variables in Moment and Normal Force Coefficient Equations

E.2 Calculation for Thesis Geometry

Given the airframe geometry shown in Figure E.1 and the corresponding dimensions in Table E.1 the airframe transfer function can be obtained. The first step in this lengthy process is to determine the location for the center of pressure of both the nose and the body. These are approximated as:

$$X_{CPN} = 0.67 L_N \tag{E.5}$$

$$X_{CPB} = \frac{0.67 A_N L_N + A_B[L_N + 0.5(L - L_N)]}{A_N + A_B} \tag{E.6}$$
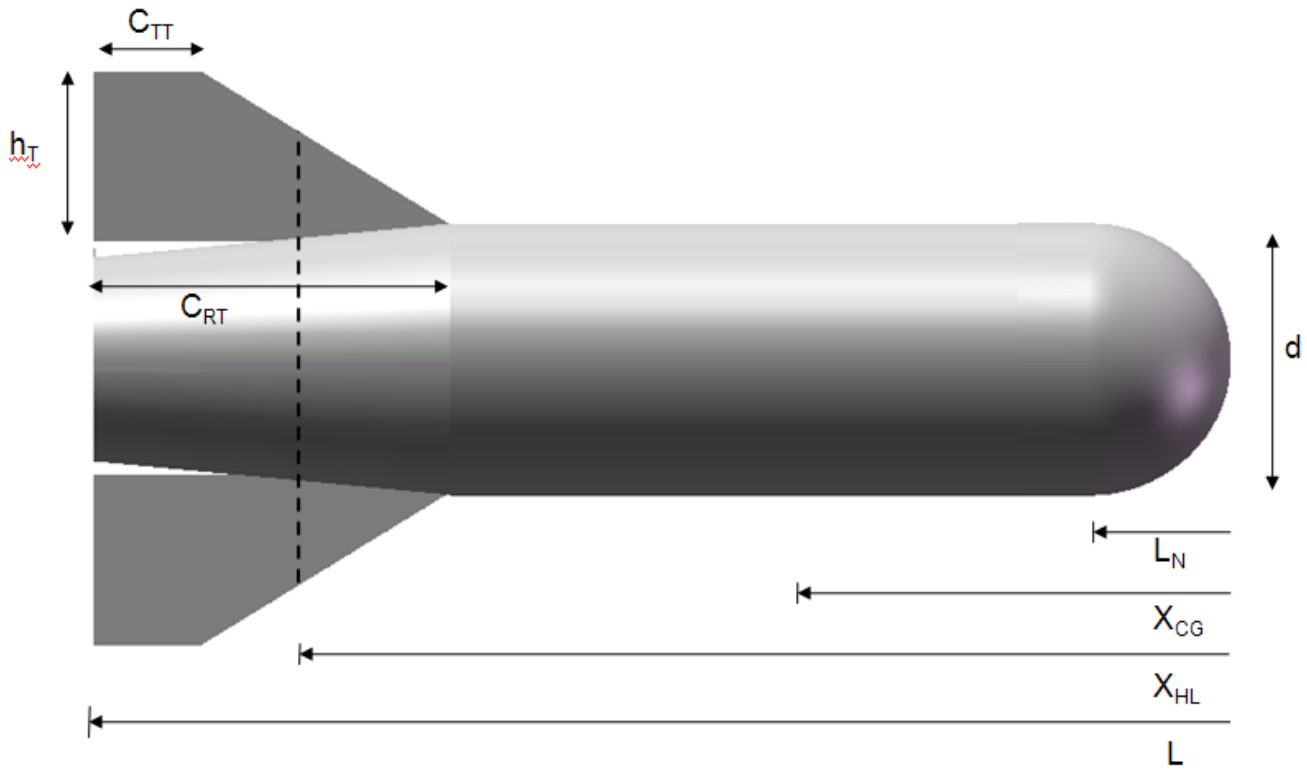
Figure E.1 Designer defined geometry and terms for airframe transfer function

Value	English	Metric
d	4 in	0.1016 m
Ln	3 in	0.0762 m
X_{CG}	8 in	0.2032 m
X_{HL}	13 in	0.3302 m
L	16 in	0.4064 m
C_{TT}	1.5 in	0.0381 m
h_T	2.5 in	0.0635 m
C_{RT}	5 in	0.1270 m

Table E.2 Measurements for Figure E.1

where the nose and body areas are approximated as:

$$A_N = 0.67 L_N d \qquad \text{(E.7)}$$

$$A_B = (L - L_N)d \qquad \text{(E.8)}.$$

We will also define the reference area, planform area, tail area, and normalized speed for subsonic travel (β) as:

$$S_{ref} = \frac{\pi d^2}{4} \qquad \text{(E.9)}$$

$$S_{plan} \approx Ld \qquad \text{(E.10)}$$

$$S_T = 0.5 h_T (C_{TT} + C_{RT}) \qquad \text{(E.11)}$$

$$\beta = \sqrt{1 - Mach^2} \qquad \text{(E.12)}.$$

With the linearized expressions for C_N and C_M, we are able to obtain their dependency upon changes in α and δ simply by dividing equations E.1 and E.2 by the two angles:

$$C_{N_\alpha} = 2 + \frac{1.5 S_{plan} \alpha}{S_{ref}} + \frac{8 S_T}{\beta S_{ref}} \qquad \text{(E.13)}$$

$$C_{N_\delta} = \frac{8 S_T}{\beta S_{ref}} \qquad \text{(E.14)}$$

$$C_{M_\alpha} = 2\frac{(X_{CG} - X_{CPN})}{d} + \frac{1.5 S_{plan} \alpha}{S_{ref}} \frac{(X_{CG} - X_{CPB})}{d} + \frac{8 S_T}{\beta S_{ref}} \frac{(X_{CG} - X_{HL})}{d} \qquad \text{(E.15)}$$

$$C_{M_\delta} = \frac{8 S_T}{\beta S_{ref}} \frac{(X_{CG} - X_{HL})}{d} \qquad \text{(E.16)}.$$

With the assumed linearized equations of motion, Zarchan defines moments and normal forces exerted upon the airframe that arise due to variations of α and δ.

$$M_\alpha = \frac{\frac{1}{2} \rho v^2 S_{ref} d C_{M_\alpha}}{I_{yy}} \qquad \text{(E.17)}$$

$$M_\delta = \frac{\frac{1}{2}\rho v^2 S_{ref} dC_{M_\delta}}{I_{yy}} \qquad (E.18)$$

$$Z_\alpha = \frac{-\frac{1}{2}g\rho v^2 S_{ref} dC_{N_\alpha}}{WV_M} \qquad (E.19)$$

$$Z_\alpha = \frac{-\frac{1}{2}g\rho v^2 S_{ref} dC_{N_\alpha}}{WV_M} \qquad (E.20)$$

where I_{yy} is the missile's moment of inertia about its longitudinal axis. These quantities are then used to develop the following simplified terms that appear in the total transfer function from control surface deflection to airframe lateral acceleration:

$$K_1 = \frac{-V_M[M_\alpha Z_\delta - Z_\alpha M_\delta]}{57.3gM_\alpha} \qquad (E.21)$$

$$\omega_Z = \sqrt{\frac{M_\alpha Z_\delta - Z_\alpha M_\delta}{Z_\delta}} \qquad (E.22)$$
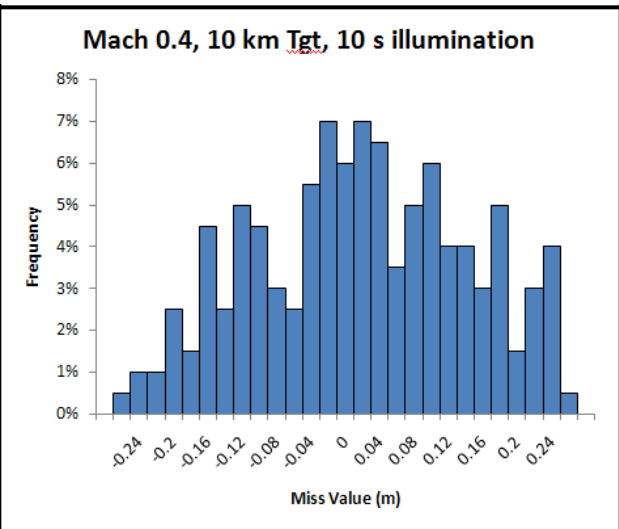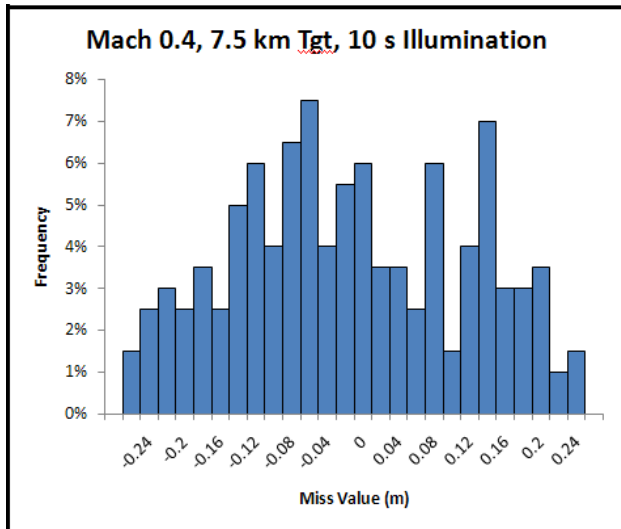
$$\omega_{AF} = \sqrt{-M_\alpha} \qquad (E.23)$$

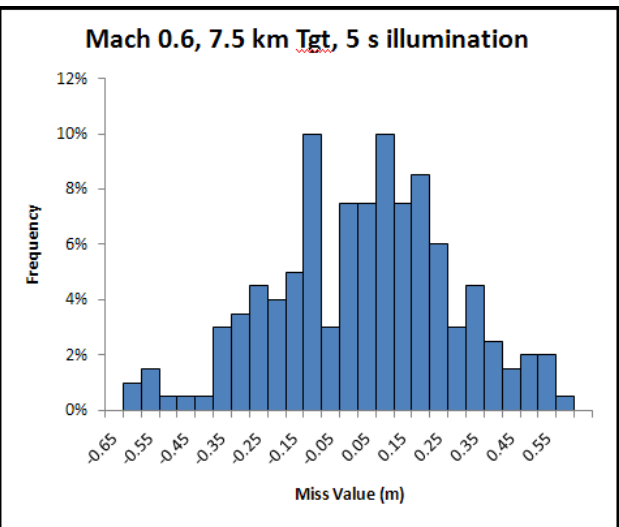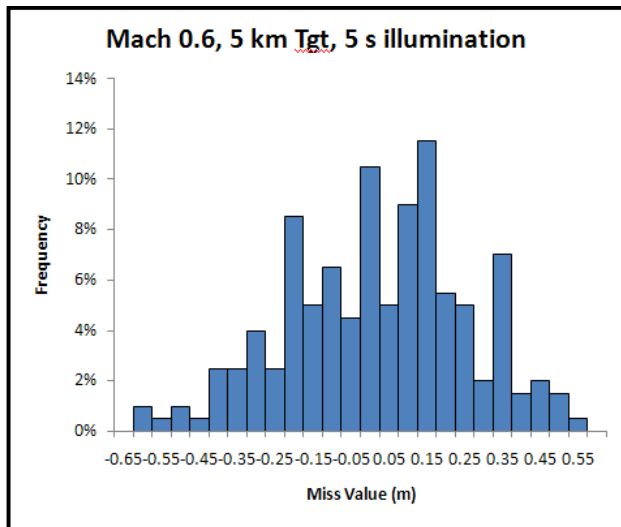$$\varsigma_{AF} = \frac{Z_\alpha \omega_{AF}}{2M_\alpha} \qquad (E.24).$$
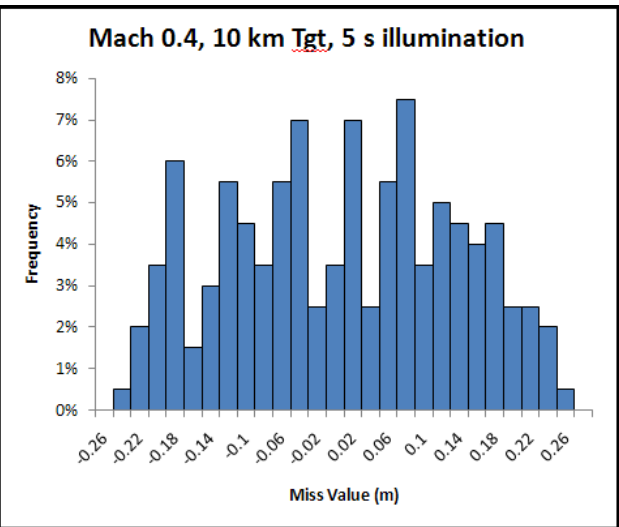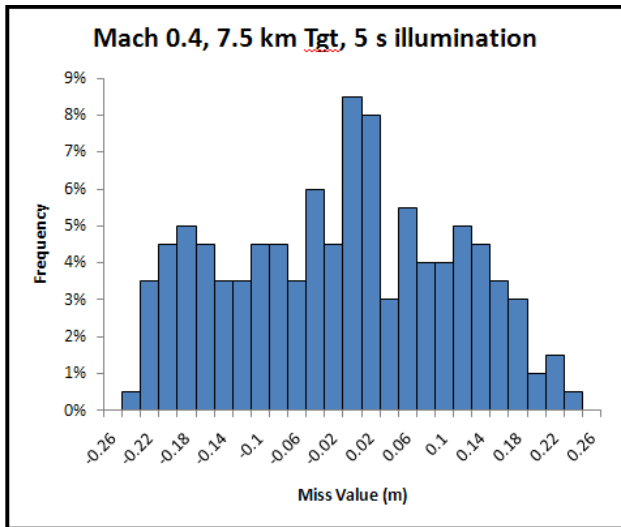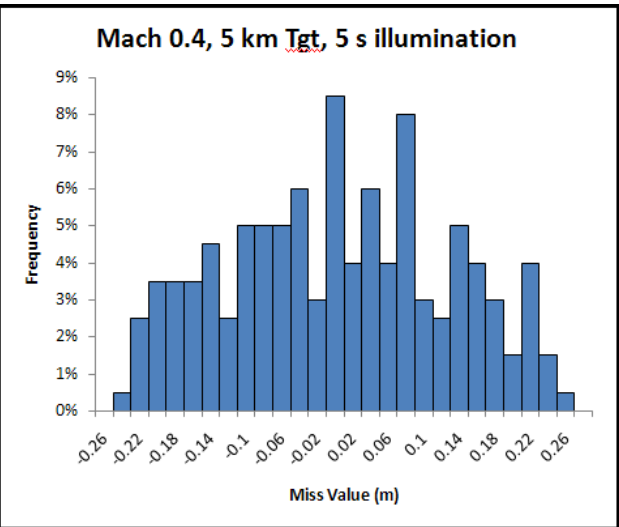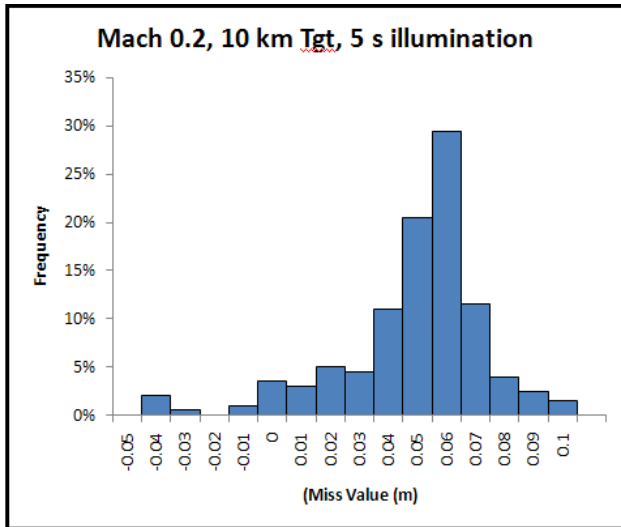
The simplified terms above allow the airframe transfer function to be expressed in a form consistent with 2nd order dynamics systems familiar to the engineering community.

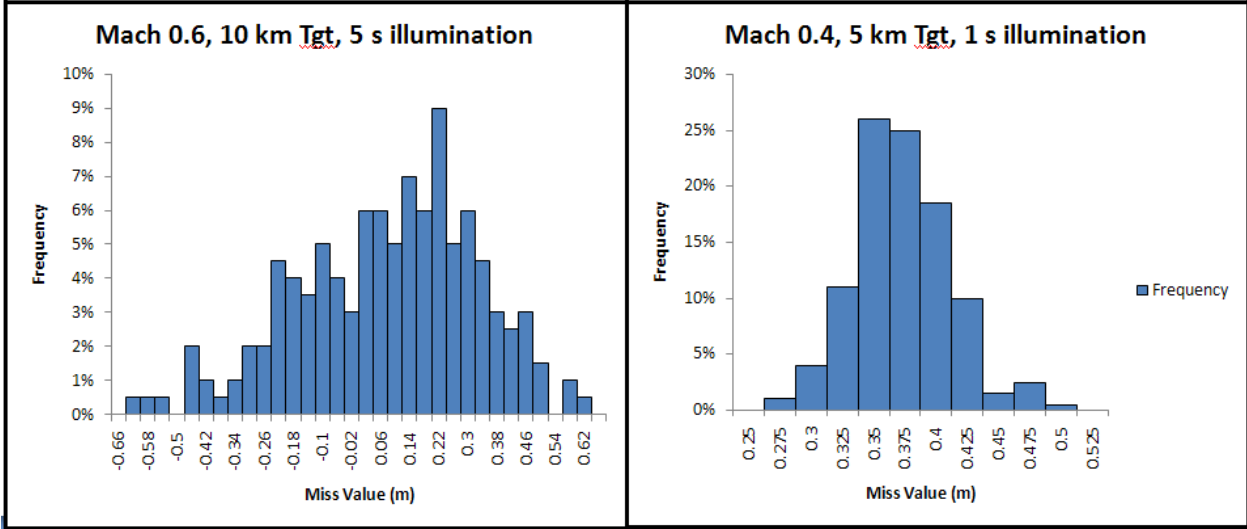The derivation of these terms gives the reader insight into how the geometry of the airframe affects the dynamics of its flight. Furthermore, Zarchan demonstrates that although the transfer function representation is only an approximation to reality, it shows very good agreement with empirical results at angles of attack less than 30°.

Appendix F – Histograms of Final System Simulation Results

Mach 0.4, 7.5 km Tgt, 10 s Illumination

Mach 0.4, 10 km Tgt, 10 s illumination

Mach 0.6, 5 km Tgt, 10 s illumination

Mach 0.6, 7.5 km Tgt, 10 s Illumination

Mach 0.2, 5 km Tgt, 5 s illumination

Mach 0.2, 7.5 km Tgt, 5 s illumination

Mach 0.6, 10 km Tgt, 5 s illumination

Mach 0.4, 5 km Tgt, 1 s illumination
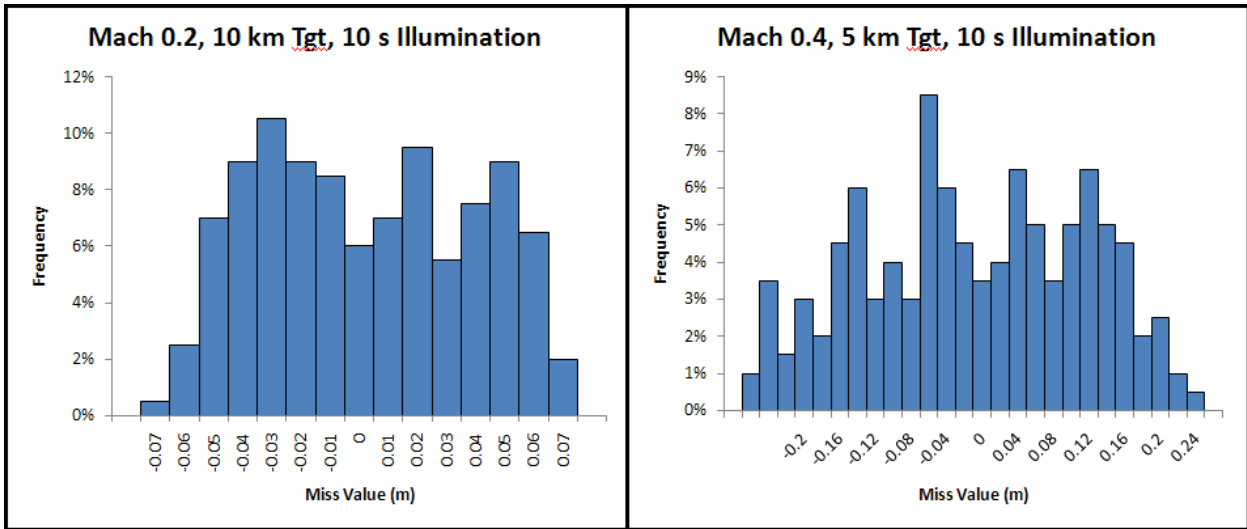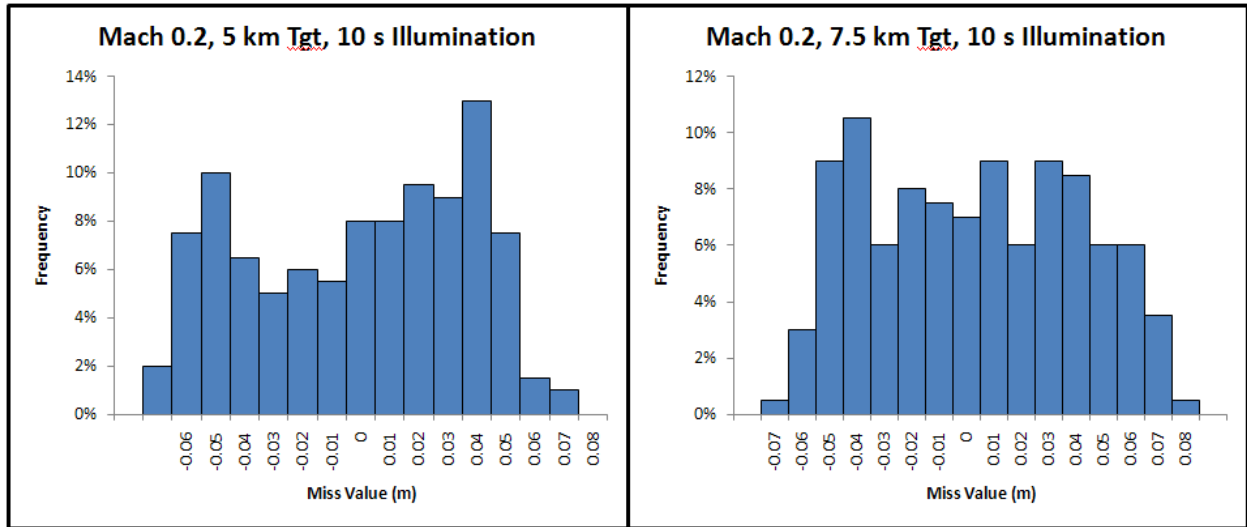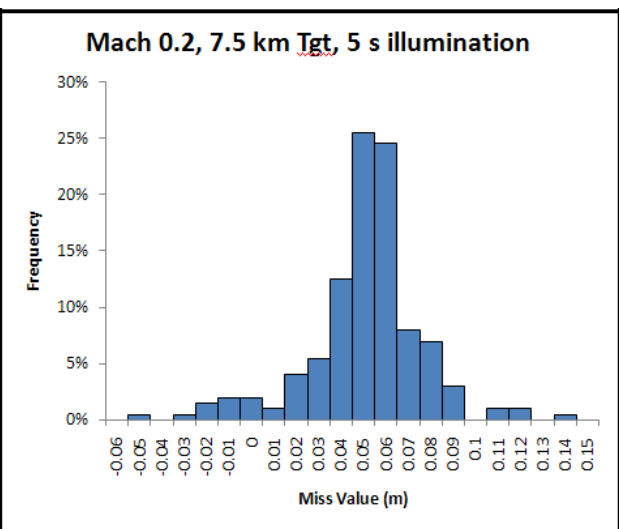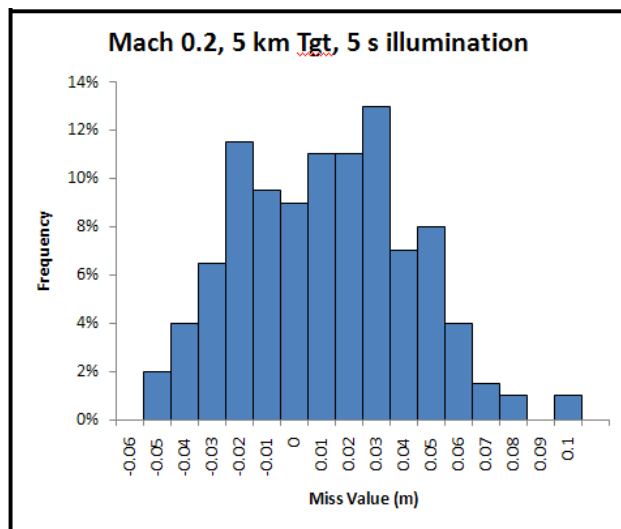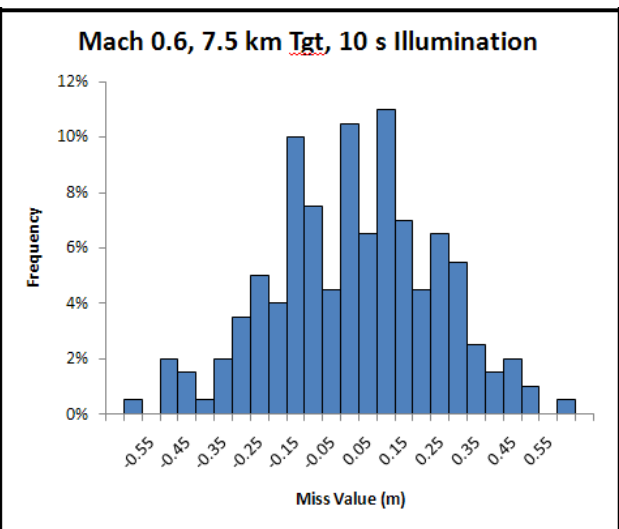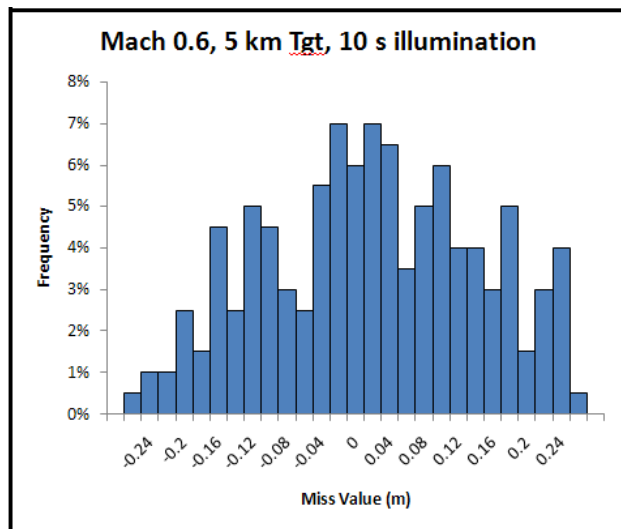
References

[1] B. W. Parkinson, *The Global Positioning System: Theory and Applications.* American Institute of Aeronautics and Astronautics, 1996, pp. 36.

[2] F. Berrigan and W. Hartung, "Fact Sheet US Arms Transfers and Security Assistance to Israel," *Foreign Policy in Focus,* 2002.

[3] K. Fowler and P. Compact, "The Wheel Has Already Been Invented," *IEEE Instrumentation & Measurement Magazine,* 2002.

[4] L. Hollingsworth. 2002, *XM395,* Precision guided mortar munition. Defense Technical Information Center.

[5] P. D. McKeehen, W. B. Blake, M. W. Pershing and D. A. Warner, "DYNAMIC MODELING AND SIMULATION OF A SMALL DESTRUCTIVE PROJECTILE," *AIAA Modeling and Simulation Technologies Conference and Exhibit, Montreal, Canada,* 2001.

[6] G. Russell, S. Cayson, M. Jones, W. Carriger, R. Mitchell, F. Strobel, M. Rembert and D. Gibson, "Army hypersonic compact kinetic-energy missile laser window design," *Proceedings of SPIE,* vol. 5078, pp. 28-39, 2003.

[7] Joint Chiefs of Staff, *Joint Tactics, Techniques, and Procedures for Laser Designation Operations.* Defense Technical Information Center, 1999.

[8] Anonymous. Light: Radiometry and photometry. Andor Technology. 2008. Available: http://www.andor.com/library/light/?app=335

[9] D. A. Fraser, *The Physics of Semiconductor Devices.* 4th ed., vol. 16, Oxford Oxfordshire; New York: Clarendon Press; Oxford University Press, 1986, pp. 196.

[10] E. L. Dereniak and D. G. Crowe, *Optical Radiation Detectors.* New York: Wiley, 1984, pp. 300.

[11] Anonymous. "PSD1: Quadrant detector specification sheet." Thorlabs. 2008

[12] I. Hamamatsu Photonics. "Position sensitive detector." 2002. Available: http://www.hamamatsu.com

[13] N. Barbour and G. Schmidt, "Inertial sensor technology trends," in *Proceedings of the 1998 IEEE Symposium on Autonomous Underwater Vehicle Technology,* 1998, pp. 55-62.

[14] N. Yazdi, F. Ayazi and K. Najafi, "Micromachined inertial sensors," *Proc IEEE,* vol. 86, pp. 1640-1658, 1998.

[15] Z. P. Barbaric and L. M. Manojlovic, "Optimization of optical receiver parameters for pulsed laser tracking systems," in *6th International Conference on Telecommunications in Modern Satellite, Cable, and Broadcast Services-TELSIKS 2003,* 2003, pp. 192-201.

[16] G. L. Knestrick, T. H. Cosden and J. A. Curcio, "Atmospheric attenuation coefficients in the visible and infrared regions," Naval Research Laboratory, 1961.

[17] Anonymous. Calculation of radiometric properties. Gigahertz Optik. 2004. Available: http://www.gigahertz-optik.com/database_en/html/applications-tutorials/tutorials/ii.-properties-and-concepts-of-light-and-color/ii.5.-calculation-of-radiometric-quantities---examples.html

[18] B. van Ginneken, M. Stavridi and J. J. Koenderink, "Diffuse and specular reflectance from rough surfaces," *Appl. Opt.,* vol. 37, pp. 130-139, 1998.

[19] Anonymous, "An Introduction to Semi-Active Laser Designation and Guidance," 2003.

[20] G. R. Osche and D. S. Young, "Imaging laser radar in the near and far infrared," *Proc. IEEE (USA),* vol. 84, pp. 103-125, Feb. 1996.

[21] R. A. Schowengerdt and R. A. Schowengerdt, *Remote Sensing, Models, and Methods for Image Processing.* ,2nd ed.San Diego: Academic Press, 1997, pp. 522.

[22] Environmental Research Institute of Michigan. Infrared Information and Analysis (IRIA) Center, W. L. Wolfe, G. J. Zissis and United States. Office of Naval Research, *The Infrared Handbook.* Washington: The Office, 1978, pp. a. 1600.

[23] A. Mecherikunnel and C. Duncan, "Total and spectral solar irradiance measured at ground surface," *Appl. Opt.,* vol. 21, pp. 554-556, 1982.

[24] F. Kearns, "Testing multiple laser systems on the Chameleon EO system: a singletarget approach," *AUTOTESTCON Proceedings, 2000 IEEE,* pp. 31-39, 2000.

[25] Anonymous. "High voltage P-type quad silicon detector." Advanced Photonix, Inc. 2006.

[26] Judson Technologies, "Indium Gallium Arsenide Detectors," 2004.

[27] D. Tipotsch, "*APKWS Demonstration,*" American Institute of Aeronautics and Astronautics, 1998.

[28] D. Blanchard, "A brief history of Air-Intercept Missile 9 (Sidewinder)," *& Proceedings,*

[29] B. Glasgow and W. Bell, "Future of anti-aircraft imaging infrared seeker missile threats," *IEEE Aerospace Applications Conference Proceedings,* vol. 4, pp. 457-465, 1999.

[30] F. J. Gonzalez, B. Ilic, J. Aida and G. D. Boreman, "Antenna-coupled infrared detectors for imaging applications," *IEEE Journal on Selected Topics in Quantum Electronics,* vol. 11, pp. 117-120, 2005.

[31] Anonymous. "Quartz dual axis rate sensor data sheet." Systron Donner Intertial. 2008. Available: http://www.systron.com/PDFS/datasheets/QDARS_US.pdf

[32] E. L. Fleeman, *Tactical Missile Design.* ,2nd ed.Reston, VA: American Institute of Aeronautics and Astronautics, 2006, pp. 468.

[33] W. B. Blake, "Missile DATCOM User's Manual–1997 Fortran 90 Revision," *Air Force Research Laboratory,* 1997.

[34] J. M. Simon and W. B. Blake, "Missile Datcom: High Angle of Attack Capabilities," *AIAA Paper,* pp. 99-4258, 1999.

[35] Brandt, S.A., Stiles, R.J., Bertin, J.J., Whitford, R., *Introduction to Aeronautics: A Design Perspective.* American Institute of Aeronautics and Astronautics, 2004.

[36] K. A. Wise and D. J. Broy, "Agile missile dynamics and control," *Journal of Guidance, Control, and Dynamics,* vol. 21, pp. 441-449, 1998.

[37] P. Zarchan, *Tactical and Strategic Missile Guidance.* ,5th ed., vol. 219, Reston, Va.: American Institute of Aeronautics and Astronautics, 2007, pp. 888.

[38] G. M. Siouris, *Missile Guidance and Control Systems.* New York: Springer, 2004, pp. 666.

[39] H. B. Hablani and D. W. Pearson, "Miss distance error analysis of exoatmospheric interceptors" *Journal of Guidance, Control, and Dynamics,* vol. 27, pp. 283-289, 2004.

[40] D. C. Montgomery, *Introduction to Statistical Quality Control.* 3rd ed. New York: Wiley, 1996.

[41] A. E. Gamble and P. N. Jenkins, "Low cost guidance for the Multiple Launch Rocket System (MLRS) artillery rocket," *Record - IEEE PLANS, Position Location and Navigation Symposium,* pp. 193-199, 2000.

[42] Anonymous. Texas instruments digital signal processor product folder. Texas Instruments, Inc. 2008. Available: http://focus.ti.com/docs/prod/folders/print/tms320c6414.html

[43] Frey, Steven E. "A strategic framework for program managers to improve command and control system interoperability" Massachusetts Institute of Technology, System Design & Management Program, 2002.

[44] Kometer, Michael W. "Command in air war : centralized vs. decentralized control of combat airpower" Massachusetts Institute of Technology, Management, and Policy Program, 2005.